Exploring The Impact of Genetic Variations on Human Hepatic Stellate Cells Using Extracellular Matrix 3D Models

Elisabetta Caon

Division of Medicine

Institute for Liver and Digestive Health

University College London

A thesis submitted for the degree of

Doctor of Philosophy

Supervisors

Prof. Krista Rombouts

Prof. Massimo Pinzani

Declaration.

I, Elisabetta Caon confirm that the work presented in this thesis is my own. Where information has been derived from other sources, I confirm that this has been indicated in the thesis.

Signature:

Abstract.

Background and aims: Liver fibrosis is a crucial pathophysiological step in chronic liver diseases (CLD). Activated hepatic stellate cells (HSCs) are the key mediators of fibrogenesis and therefore, research has been focusing on identifying and addressing pro-fibrogenic mechanisms in HSCs for the development of new drug candidates to treat fibrogenic liver diseases. This process has been hampered by the lack of appropriate models. In addition, only recently attention has been given to the importance of genetic polymorphisms for the onset of CLD, with numerous new variants being discovered, although their molecular role is still largely unclear. In this project, the impact of the PNPLA3 I148M and TM6SF2 E156K variants on the pro-fibrogenic behaviour of HSCs has been investigated utilizing as a platform 3D scaffolds and hydrogels obtained from the decellularized extracellular matrix (ECM) of healthy and diseased human livers.

Methods: Healthy or cirrhotic decellularized human liver ECM 3D scaffolds were either utilized for the culture of primary human HSCs wild type (WT) or mutant for the genetic variant under investigation or lyophilized and solubilized to yield liver ECM solution. The ECM solution was mixed with two different gelling agents to form hydrogels for the culture of HSCs WT or mutant for the genetic variant under investigation. RNA sequencing was performed on 2D-cultured primary human HSCs and liver biopsies of obese individuals, genotyped for the PNPLA3 I148M variant. Cell behaviour of HSCs cultured in ECM hydrogels or scaffolds and treated with/without TGFB1/Endothelin-1/CytosporoneB (Csn-B) was evaluated.

Results: Comparison between transcriptomic analysis of liver biopsies and primary human HSCs highlighted shared PNPLA3 I148M-driven dysregulated pathways related to mitochondrial function, antioxidant response, ECM remodelling and TGFB1 signalling. Analogous pathways were dysregulated in HSCs WT/I148M-PNPLA3 cultured in 3D liver scaffolds. Mitochondrial dysfunction in I148M-PNPLA3 cells was linked to respiratory chain complex IV insufficiency. Antioxidant capacity was lower in I148M-PNPLA3 HSCs, while ROS secretion was increased in I148M-PNPLA3 HSCs and higher in bioengineered cirrhotic scaffolds *versus* healthy scaffolds. TGFB1 signalling pathway followed the same trend. In I148M-PNPLA3 cells, TGFB1-

endogenous inhibitor NR4A1 expression and activation were decreased: treatment with the Csn-B agonist increased total NR4A1 in HSCs cultured in healthy but not in cirrhotic 3D scaffolds. This led to a decreased TGFB1 signalling and increased NRF2 in Csn-B treated cells. Hydrogels made with human liver ECM proved to be stable and support viability and responsiveness to pro-fibrogenic treatment of HSCs. Furthermore, HSCs showed similar behaviour when cultured in ECM scaffolds or ECM hydrogels and featured a less activated phenotype compared to 2D plastic culture. HSCs carrying the PNPLA3 I148M and TM6SF2 E156K variants showed to have increased basal contraction and activation induced by the presence of the cirrhotic ECM compared to WT HSCs.

Conclusions: This study illustrates how the usage of novel 3D models based on human derived healthy and cirrhotic decellularized liver ECM combined with omics and molecular biology techniques can help unravel the pro-fibrogenic behaviour of HSCs in presence of different genetic variants and their role in the progression of CLD.

Impact Statement.

The burden of chronic liver disease in the UK has seen a dramatic increase in the last 30 years and is estimated to be currently affecting 1.5 billion people worldwide.

Currently, the only effective treatment for advanced liver disease is transplantation, and although it has been demonstrated that acting on the disease aetiology can regress cirrhosis and fibrosis, no targeted treatment is available.

The discovery of efficient drugs for the treatment of liver fibrosis has been hampered for years by the complex biology of the key mediators of fibrogenesis, i.e., activated hepatic stellate cells (HSCs). In fact, the process of drug discovery mainly utilizes *in vitro* models based on conventional 2D plastic surfaces. The rigidity of this material induces an activated status in HSCs which is different from the one in the diseased liver. Hence, the necessity of new *in vitro* models providing more accurate platforms to investigate the HSCs behaviour and response to drugs.

In addition, the recent discovery of several genetic variants associated with the onset of chronic liver disease, as well as other environment and systemic factors, increased the complexity in setting up platforms and experiments to investigate liver disease.

In this project we showed an efficient method to investigate how genetic variants might affect HSCs behaviour in liver disease.

We used transcriptomic analysis to obtain an overview of all the different pathways and genes which are affected by the presence of a specific genetic variant in HSCs. This database will be soon published and available for the scientific community to further explore HSCs behaviour.

To overcome issues given by 2D plastic cultures or animal models, we used only primary human-derived cells which were genotyped for the genetic variant, and we cultured them on a novel human-derived *in vitro* 3D extracellular matrix model which recapitulates the ECM microenvironment and the stiffness of both a healthy and a cirrhotic human liver.

We were able to replicate the findings from the transcriptomic analysis in the *in vitro* 3D model and further explore the mechanisms leading to the dysregulation of specific pathways, dissecting the effects of the healthy and cirrhotic ECM on HSCs behaviour. Thus, we demonstrated that the 3D ECM scaffolds model could be an important new platform for the study of HSCs biology.

The transcriptomic analysis also led to the identification of a gene deregulated in presence of the genetic variant, which could raise future interest as a possible target in the treatment of liver disease.

With the aim of simplifying and increase the scalability of the 3D ECM scaffolds model, a second part of the project focused on the optimization of decellularized ECM hydrogels for the culture of HSCs. This second platform showed retention of the main features of the scaffolds model, thus allowing the setting up of more complex experiments to investigate the impact of genetic variants on HSCs.

Overall, I believe this work represents a small step forward in the understanding of HSCs biology in chronic liver diseases and of liver fibrosis modelling.

Acknowledgments.

First and foremost, I would like to thank my supervisor Prof. Krista Rombouts for her great support during these four years; the stimulating conversations, the constant guidance, and the opportunity to try and stir this project in the direction I thought it was best to go. You were a great example of passion and perseverance in every moment of the research path, and always had a smile on your face. Thank you to my secondary supervisor Prof. Massimo Pinzani for always being available and supportive in the key moments of my PhD journey, and for the countless illuminating advice and conversations which helped me grow as a young scientist and helped build my confidence in the scientific world. I would also like to thank Dr. Giuseppe Mazza who first introduced me to the tissue engineering world and gave me the opportunity to work in collaboration with several other departments, giving me the chance to learn how to work with other groups.

I am also very grateful to Dr. Michele Vacca, who helped me with the transcriptomic analysis, Prof. Jan-Willem Taanman who taught me the secrets of mitochondria, and Dr. Zalike Keskin-Erdogan and Nicola Morgan who helped me with the rheological and SEM analysis. Thank you, Dr. Andrew Hall, for your patience in helping me optimizing the immunohistochemistry.

A big thank you goes to Dr. Maria Giovanna Vilia, Dr. Walid Al-Akkad and Dr. Luca Frenguelli: you all have been great teachers and friends since I first started, and still going. I owe you for most of the things I know how to do in a lab and for the endless support and laughs in every moment of these past few years.

I want to say thank you to Dr. Margarita Papatheodoridi and Lucia Marinas Del Rey for being the best post-lockdown labmates and friends. Having you as companions in good and bad times has made everything easier and funnier. Thank you also to Maria Martins and Harry Hodgetts who have been my labmates for the last few months and were always available to help, for a good chat or a piece of cake. I would also like to thank all the people who have come and gone from the Pinzani-Rombouts lab in the past few years and that have shared with me a piece of my journey.

Thank you to Martina Marrali, who started in the lab at the same time as me and has since then been an invaluable friend who never gets tired to listen to me in my ups and downs whether she is close or far away. May this stay like this in the years to come.

A big thank you to all my friends in London and in Italy, especially Giulia, Giuliona, Pedro and Greta; it has been nice to be able to share happiness and fears with someone who is in a similar path as mine.

The biggest thank you goes to my partner Jay. Without your love and your endless support none of this would have been possible. You were able to believe in me and my abilities when I was not, and for that I can't be thankful enough. Your help was essential through the difficult moments of this journey. Every bad day would always end up being better and full of joy and laughter thanks to you and your good spirit. I feel really fortunate to have you by my side.

Last but not least, I want to thank my family for giving me the chance to get to this point. Mamma e Papa', grazie per avermi dato l'occasione di arrivare fino a qui. Senza di voi tutto questo non sarebbe stato possibile. Grazie per avermi supportata in ogni mia decisione anche quando cio' mi ha portata lontana da voi. La presenza e l'affetto che voi ed Alberto mi date e' stata importante in ogni giorno di questo percorso.

Table of contents.

Abstract. 3

Impact Statement. 5

Acknowledgments. 7

List of Figures. 12

List of Tables. 16

Abbreviations. 17

Achievements. 25

1 General introduction 27

1.1 Chronic Liver Disease. 27

1.2 Hepatic stellate cells and fibrogenesis in chronic liver disease. 28

1.3 Liver extracellular matrix. 30

1.4 Current hepatic models for pre-clinical studies. 31

1.5 Traditional 3D in vitro hepatic systems. 32

1.6 Genetic variants in chronic liver disease. 35

2 Aims and Objectives. 36

3 Exploring the impact of the genetic PNPLA3 I148M variant on primary human hepatic stellate cells by using 3D extracellular matrix models 37

3.1 Introduction. 37

3.1.1 The PNPLA3 I148M genetic variant in hepatic stellate cells and liver disease. 37

3.1.2 Decellularized liver ECM scaffolds as three-dimensional in vitro models. 38

3.2 Materials and Methods. 40

3.2.1 Study population and genotyping. 40

3.2.2 Primary human HSCs isolation and culture. 41

3.2.3 DNA extraction and genotyping of primary human HSCs. 41

3.2.4 Whole transcriptome amplification and RNA sequencing (NGS). 41

3.2.5 Bioinformatics functional analyses. 42

3.2.6 Preparation of 3D human liver scaffolds. 43

3.2.7 Primary human HSCs culture on 3D human liver scaffolds or 2D. 45

3.2.8 Histology and Immunostaining analysis. 45

3.2.9 Viability assay. 46

3.2.10 RNA extraction, complementary DNA (cDNA) synthesis and quantitative real time PCR (RT-qPCR). ... 46
3.2.11 Nanostring analysis. ... 48
3.2.12 Flow Cytometry Analysis. ... 48
3.2.13 Protein extraction and quantification. ... 49
3.2.14 Western Blot. ... 49
3.2.15 Protein secretion analysis. ... 50
3.2.16 ROS secretion analysis. ... 51
3.2.17 Complex IV and citrate synthase activity assay. ... 51
3.2.18 Blue Native electrophoresis. ... 51
3.2.19 Extracellular Flux analysis. ... 52
3.2.20 Data analysis and statistics. ... 52

3.3 Results ... 53
3.3.1 Transcriptomic analysis of WT-PNPLA3 and I148M-PNPLA3 HSCs and human liver biopsies. ... 53
3.3.2 The 3D HSCs model recapitulates PNPLA3 I148M-induced modulation of intracellular pathways observed in human livers and 2D models. ... 61
3.3.3 The PNPLA3 I48M variant causes mitochondrial dysfunction in HSCs 65
3.3.4 Antioxidant response is reduced in PNPLA3-I148M HSCs. ... 69
3.3.5 Antifibrotic NR4A1 is downregulated in PNPLA3-I148M vs WT HSCs. 72
3.3.6 NR4A1 agonist Cytosporone-B increases NR4A1 only in HSCs cultured in 3D healthy scaffolds. ... 75
3.3.7 Cytosporone-B attenuates TGFB1-induced production of COL1A1 and increases antioxidant enzymes in both WT and PNPLA3-I148M HSCs. ... 77
3.3.8 NR4A1 phosphorylation is differently regulated in WT vs I148M-PNPLA3 HSCs ... 81

3.4 Discussion ... 84

4 Modelling liver fibrosis in three-dimensional liver extracellular matrix hydrogels ... 88

4.1 Introduction. ... 88
4.1.1 Hepatic stellate cells contraction and liver disease. ... 88
4.1.2 The TM6SF2 E156K genetic variant in hepatic stellate cells and liver disease. ... 89
4.1.3 Hydrogels as three-dimensional in vitro models. ... 90

4.2 Materials and methods. ... 93
4.2.1 LX2 cells culture. ... 93
4.2.2 DNA extraction and genotyping of primary human HSCs. ... 93
4.2.3 Liver ECM solution preparation. ... 93
4.2.4 Synthesis of $PGMA_{55}$-$PHPMA_{135}$ diblock copolymer worms for HepGel production. ... 94
4.2.5 HepGel preparation. ... 94
4.2.6 ECM Gel preparation. ... 94

4.2.7 *Seeding of primary HSC and LX2 cells in HepGel.* ... 95
4.2.8 *Seeding of primary HSC in ECM Gels.* ... 95
4.2.9 *Live/Dead assay* ... 96
4.2.10 *Immunofluorescence staining and contraction evaluation in HepGel.* ... 96
4.2.11 *Contraction evaluation in ECM Gels.* ... 97
4.2.12 *Protein extraction and western blot.* ... 98
4.2.13 *Mechanical characterization.* ... 98
4.2.14 *Scanning Electron Microscopy.* ... 99
4.2.15 *Data analysis and statistics.* ... 99

4.3 Results. ... 100
4.3.1 Thermo-responsive human liver extracellular matrix three-dimensional hydrogels for modelling liver fibrosis and evaluating HSCs contraction. ... **100**
4.3.1.1 *Assessment of LX2 cell density and viability in HepGel* ... 100
4.3.1.2 *LX2 cultured in HepGel respond to pro-fibrogenic stimuli: gene and protein expression analysis.* ... 101
4.3.1.3 *LX2 cultured in HepGel response to pro-fibrogenic stimuli: contraction.* 102
4.3.1.4 *Assessment of HSC viability and proliferation in HepGel.* ... 103
4.3.1.5 *HSC cultured in HepGel respond to pro-fibrogenic stimuli: gene and protein expression analysis.* ... 105
4.3.1.6 *HSCs cultured in HepGel response to pro-fibrogenic stimuli: contraction* ...106
4.3.2 Nanocellulose-based human liver extracellular matrix three-dimensional hydrogels (ECM Gels) for modelling liver fibrosis and evaluating HSCs contraction. ... **108**
4.3.2.1 *Characterization of the mechanical properties of ECM Gels.* ... 108
4.3.2.2 *Assessment of HSCs cell density and viability in ECM Gels.* ... 111
4.3.2.3 *HSCs cultured in ECM Gels respond to pro-fibrogenic stimuli: gene expression analysis.* ... 113
4.3.2.4 *Comparison of HSCs behaviour when cultured in ECM Gels, ECM-scaffolds or 2D.* ... 114
4.3.2.5 *Cultures in ECM Gels can be used to investigated genetic variants in HSCs.* ...116
4.3.2.6 *Cultures in ECM Gels to evaluate HSCs contraction.* ... 117

4.4 Discussion. ... 121

5 General Conclusions and Future Perspectives. ... **126**

Bibliography. ... **131**

List of Figures.

Figure 1: Schematic of chronic liver disease progression. 28

Figure 2: Hepatic stellate cells activation.. 30

Figure 3: Summary of three-dimensional platforms utilized for liver disease modelling. 34

Figure 4: Role of PNPLA3 in HSCs. 38

Figure 5: Decellularized human liver scaffolds quality control. 45

Figure 6: Characterization of HSCs genotyped WT or I148M for the PNPLA3 variant and cultured on plastic.. 54

Figure 7: Gene expression profiled by NGS and analysed by IPA of in vitro-cultured primary human HSCs genotyped for WT-I148M PNPLA3 mutations: Canonical Pathways and Biofunctions. 55

Figure 8: Gene expression profiled by NGS and analysed by IPA of in vitro-cultured primary human HSCs genotyped for WT-I148M PNPLA3 mutations: Upstream Regulators and target genes.. 56

Figure 9: Comparative IPA analysis of in vitro-cultured primary human HSCs and human biopsies of patients stratified according to carriage of the I148M. 57

Figure 10: Gene expression profiled by NGS and analysed by IPA of in vitro-cultured primary human HSCs and human biopsies genotyped for WT-I148M PNPLA3 mutations. 58

Figure 11: Gene expression profiled by NGS and analysed by IPA of in vitro-cultured primary human HSCs and human biopsies genotyped for WT-I148M PNPLA3 mutations: schematic. 59

Figure 12: Validation of target genes highlighted by comparative NGS analysis of in vitro-cultured primary human HSCs and human biopsies genotyped for WT/I148M-PNPLA3 mutations.. 60

Figure 13: Characterization of the 3D model of HSCs genotyped WT or I148M for the PNPLA3 variant and cultured on healthy or cirrhotic human liver decellularized scaffolds: H&E 61

Figure 14: Characterization of the 3D model of PNPLA3 WT or I148M HSCs cultured on healthy or cirrhotic human liver decellularized scaffolds: Nanostring. 63

Figure 15: Characterization of the 3D model of PNPLA3 WT or I148M HSCs cultured on healthy or cirrhotic human liver decellularized scaffolds: TGFB1 and COL1A1. . 64

Figure 16: PNPLA3-I148M HSCs have impaired mitochondrial function compared to PNPLA3-WT HSCs: VARS2... 65

Figure 17: PNPLA3-I148M HSCs have impaired mitochondrial function compared to PNPLA3-WT HSCs: Complex IV.. 67

Figure 18: PNPLA3-I148M HSCs have impaired mitochondrial function compared to PNPLA3-WT HSCs: Mitochondrial respiratory chain complexes and OCR.. 68

Figure 19: Characterization of antioxidant response of HSCs PNPLA3-I148M WT HSCs cultured in healthy or cirrhotic scaffolds: CYGB, NRF2 and KEAP1. 70

Figure 20: Characterization of antioxidant response of HSCs PNPLA3-I148M WT HSCs cultured in healthy or cirrhotic scaffolds: SOD1, SOD2 and ROS.. 71

Figure 21: NR4A1 expression and TGFB1 regulation in WT-PNPLA3 or I148M-PNPLA3 genotyped HSCs: gene and protein expression. 73

Figure 22: NR4A1 expression and TGFB1 regulation in WT-PNPLA3 or I148M-PNPLA3 genotyped HSCs: IHC. 74

Figure 23: Effect of the natural agonist Csn-B on NR4A1 expression in WT-PNPLA3 or I148M-PNPLA3 genotyped HSCs: dose-response.. 75

Figure 24: Effect of the natural agonist Csn-B on NR4A1 expression in WT-PNPLA3 or I148M-PNPLA3 genotyped HSCs: NR4A1.. 77

Figure 25: Effect of the natural agonist Csn-B on activation markers and antioxidant enzymes in WT-PNPLA3 or I148M-PNPLA3 genotyped HSCs: COL1A1. 78

Figure 26: Effect of the natural agonist Csn-B on activation markers and antioxidant enzymes in WT-PNPLA3 or I148M-PNPLA3 genotyped HSCs: TGFB1. 79

Figure 27: Effect of the natural agonist Csn-B on activation markers and antioxidant enzymes in WT-PNPLA3 or I148M-PNPLA3 genotyped HSCs: pro-COL1A1.. 79

Figure 28: Effect of the natural agonist Csn-B on activation markers and antioxidant enzymes in WT-PNPLA3 or I148M-PNPLA3 genotyped HSCs: NRF2. 80

Figure 29: Effect of the natural agonist Csn-B on activation markers and antioxidant enzymes in WT-PNPLA3 or I148M-PNPLA3 genotyped HSCs: CYGB.................... 81

Figure 30: Mechanism controlling NR4A1 activation in WT-PNPLA3 or I148M-PNPLA3 HSCs cultured on healthy or cirrhotic scaffolds. 83

Figure 31: Schematic of the effect of the PNPLA3 I148M mutation on mitochondrial activity, oxidative stress and NR4A1 regulation in HSCs.. 87

Figure 32: Crosstalk between LSECs and HSCs. 89

Figure 33: Set-up of the system to measure contraction of HSCs in ECM-gels. 98

Figure 34: Viability of LX2 cells in HepGel.. 101

Figure 35: Gene and protein expression analysis of LX2 cells cultured in HepGel and treated with TGFB1. 102

Figure 36: Immunofluorescence staining of LX2 cells cultured on HepGel and treated with TGFB1. 103

Figure 37: Viability of primary HSCs in HepGel.. 104

Figure 38: Gene and protein expression analysis of primary HSCs cultured in HepGel and treated with TGFB1. 105

Figure 39: Gene expression analysis of primary HSCs cells cultured in HepGel or 2D and treated with TGFB1. 106

Figure 40: Immunofluorescence staining of primary HSCs cultured on HepGel and treated with TGFB1. 107

Figure 41: Mechanical properties of ECM Gels: E' an E". 109

Figure 42: Mechanical properties of ECM Gels: Young's modulus.. 109

Figure 43: Mechanical properties of ECM Gels: SEM. 110

Figure 44: Evaluation of viability and proliferation of HSCs cultured in healthy ECM Gels.. 112

Figure 45: Evaluation of viability and proliferation of HSCs cultured in cirrhotic ECM Gels.. 113

Figure 46: Responsiveness to TGFB1 treatment of HSCs cultured in healthy or cirrhotic ECM Gels. *114*

Figure 47: Comparison of HSCs behaviour in healthy or cirrhotic ECM Gels, scaffolds or 2D culture........ *115*

Figure 48: Comparison of the 3D ECM Gels versus ECM scaffolds model......... *116*

Figure 49: Comparison of WT or HET-MUT HSCs behaviour in healthy or cirrhotic ECM Gels......... *117*

Figure 50: Contraction evaluation of HSCs TM6SF2-WT or TM6SF-E156K cultured in healthy ECM Gel. *119*

Figure 51: Protein expression of contractile proteins in HSCs TM6SF2-WT or –E156K cultured in healthy ECM gels......... *120*

List of Tables.

Table 1: Clinical features of patients analysed in the Human RNAsequencing dataset and stratified for PNPLA3 I148M genotype…………………………………………...40

Table 2: Decellularization protocol 444

Table 3: Antibodies used for immunohistochemistry staining................................ 466

Table 4: Applied Biosystem Taqman gene expression assays used for qPCR 477

Table 5: Antibodies used for Western Blot analysis 50

Table 6: Antibodies used for BN-PAGE... 511

Table 7: NR4A1 expression and TGFB1 regulation in WT-PNPLA3 or I148M-PNPLA3 genotyped HSCs: NR4A1 activity……………………………………………. 74

Table 8: List of fluorescent dyes used for immunofluorescence staining……………97

Table 9: ECM Gel composition………………………………………………………..108

Abbreviations.

2D – Two dimensional

3D – Three dimensional

4-HNE - 4-Hydroxynonenal

ABCG5/G8 - ATP-binding cassette sub-family G member 5/8

ACTA2- Actin Alpha 2

ACVA - 4,4-azobis (4-cyanopentanoic acid)

ADPN - adiponutrin

AIH - autoimmune hepatitis

AKT - AKT serine/threonine kinase

ALD – Alcoholic Liver Disease

ALTCs - Acellular Liver Tissue Cubes

APOB – Apolipoprotein B

ATP - Adenosine 5′-triphosphate

ATP5A - ATP synthase F1 subunit alpha

ATP7B - ATPase Copper Transporting Beta

BCA – bicinchoninic acid

BMP1 - Bone morphogenetic protein 1

BN-PAGE – Blue Native PAGE

BSA – Bovine Serum Albumin

CCl4 – Carbon Tetrachloride

CCR2 - C-C Motif Chemokine Receptor 2

CCR5 - C-C Motif Chemokine Receptor 5

CLD – Chronic Liver Disease

COL1A1 – Collagen Alpha 1 type I

COL1A3 – Collagen Alpha 3 type I

CPDB - 2-Cyanopropyl Dithiobenzoate

CSN-B – Cytosporone B

CYGB – Cytoglobin B

DMA – Dynamic mechanical analysis

ECM – Extracellular Matrix

EDTA - Ethylenediaminetetraacetic acid

EFEMP1 - EGF containing fibulin like extracellular matrix protein 1

EGR1- Early Growth Response 1

ERK - extracellular signal-regulated kinases

ET-1 – Endothelin-1

FACS – Fluorescent Activated Cell Sorting

FBS – Fetal Bovine Serum

FDA – Fluorescein Diacetate

FGF21 - Fibroblast growth factor 21

FOS - Protein c-Fos

FSC-A – Forward Scatter Area

FSC-H – Forward Scatter Height

FXR - Farnesoid X receptor

GAPDH - Glyceraldehyde 3-phosphate dehydrogenase

GKCR - Glucokinase Regulator

GMA - glycerol methacrylate

GSA – Gene Set Analysis

GSTT1 – Glutathione Transferase 1

GWAS - genome-wide association studies

H&E – Haematoxylin and Eosin

HBSS - Hank’s Balanced Salt Solution

HBV – Hepatitis B Virus

HCC – Hepatocellular Carcinoma

HCV – Hepatitis C Virus

HepGel – liver ECM decellularized solution mixed with PGMA55-PHPMA135 diblock copolymer (1:1)

HET – Heterozygous

HFE - High FE2+

HMOX1 - Heme Oxygenase 1

HPMA - 2-hydroproxyl methacrylate

HSCs – Hepatic Stellate Cells

HSD17B13 - Hydroxysteroid 17-Beta Dehydrogenase 13

HTS – High Throughput Screening

IL1β - Interleukin 1 beta

IL6 - Interleukin 6

ILK – Integrin-Linked Kinase

IPA – Ingenuity Pathway Analysis

JUN - Jun Proto-Oncogene

KEAP1 - Kelch like ECH associated protein 1

KF – Kupffer Cells

KLF-2 - Kruppel-like factor 2

LOX – Lysyl Oxidase

LSECs – Liver Endothelial Sinusoidal Cells

MBOAT7 - Membrane Bound O-Acyltransferase Domain Containing 7

MDA - Malondialdehyde

MLCII – Myosin Light Chain 2

MMPs - Metalloproteinases

MQ – Milli-Q water

MTCO1 - Mitochondrially Encoded Cytochrome C Oxidase I

MTCO2 - Mitochondrially Encoded Cytochrome C Oxidase II

NAFLD – Non-Alcoholic Fatty Liver Disease

NAS – NAFLD activity score

NASH – Non-Alcoholic Steatohepatitis

NDUFB6 - NADH:Ubiquinone Oxidoreductase Subunit B6

NGS – Next Generation Sequencing

NO – Nitric oxide

NPCs – Non-Parenchymal Cells

NR4A1 - Nuclear Receptor Subfamily 4 Group A Member 1

NR4A2 - Nuclear Receptor Subfamily 4 Group A Member 2

NR4A3 - Nuclear Receptor Subfamily 4 Group A Member 3

NRF2 - Nuclear factor, erythroid 2 like 2

OCR – Oxygen Consumption Rate

OXPHOS – Oxidative Phosphorylation

P(PF-co-EG) - poly(propylenefumarate-co-ethylene glycol)

PAA – Peracetic acid

PBS – Phosphate Buffered Saline

PCLS – Precision Cut Liver Slices

PDGF – Platelet Derived Growth Factor

PEG - Poly-ethylene glycol

PEO - polyethylene oxide

PGMA - Poly(glycerol monomethacrylate)

PI – Propidium Iodide

PLA - polycaprolactone

PLG - polylactidecoglycolide

PNIPPAAm - poly(N-isopropylacrylamide)

PNPLA3 – Patatin-like Phospholipase domain containing 3

PPARα - Peroxisome proliferator-activated receptor alpha

PPARγ - Peroxisome proliferator-activated receptor gamma

PPARδ - Peroxisome proliferator-activated receptor delta

PTGS2 - Prostaglandin-endoperoxide synthase 2

PUFAs - Polyunsaturated fatty acids

PVA - poly (vinyl alcohol)

PVDF - polyvinylidene fluoride

RGD - Arg – Gly – Asp

RIPA – Radio-immunoprecipitation assay

RM – Reagent Mix

RNS – Reactive Nitrogen Species

ROS – Reactive Oxygen Species

RP18S - Ribosomal protein S18

RT – Room Temperature

RT –qPCR – Real Time quantitative PCR

SDC - Sodium Deoxycholate

SDHA - Succinate Dehydrogenase Complex Flavoprotein Subunit A

SDS - Sodium Dodecylsulfate

SDS-PAGE - sodium dodecyl sulfate-polyacrylamide gel electrophoresis

SEM – Scanning Electron Microscopy

SERPINA1 - Serpin Family A Member 1

SERPINE1 - Serpin family E member 1

SFM – Serum Free Medium

SGK1 - Serum/glucocorticoid regulated kinase 1

SK1 - sphingosine kinase -1

SNAI1 - Snail family transcriptional repressor 1

SNP – Single Nucleotide Polymorphism

SOD1 - Superoxide dismutase 1

SOD2 - Superoxide dismutase 2

SSC-A – Side scatter Area

TG – Triglycerides

TGFβ – Transforming Growth Factor β

TIMP1 – Tissue Inhibitor of Metalloproteinases 1

TIMPs - Tissue inhibitors of metalloproteinases

TM6SF2 - Transmembrane 6 superfamily 2

UQRCQ - ubiquinol-cytochrome c reductase

URA – Upstream Regulator Analysis

VARS2 – Valyl RNA synthetase 2

VEGF – Vascular Endothelial Growth Factor

VLDL – Very Low-density lipoproteins

VMSCs – Vascular Smooth Muscle Cells

WT – Wild Type

Achievements.

During the course of my PhD the following achievements were obtained:

Published Articles:

- **E. Caon**, M. Martins, H. Hodgetts, L. Blanken, M. G. Vilia, A. Levi, K. Thanapirom, W. Al-Akkad, J. Abu-Hanna, G. Baselli, A. R. Hall, J.W. Taanman, M. Vacca, L. Valenti, S. Romeo, G. Mazza, M. Pinzani, K. Rombouts, "*Exploring the impact of the genetic PNPLA3 I148M variant on primary human hepatic stellate cells by using 3D extracellular matrix models*", submitted to *Journal of Hepatology*, pending revision;
- K. Thanapirom, **E. Caon**, M. Papatheodoridi, L. Frenguelli, W. Al-Akkad, Z. Zhang, M. G. Vilia, M. Pinzani, G. Mazza, K, Rombouts, "*Optimization and validation of a novel three-dimensional co-culture system in decellularized human liver scaffold for the study of liver fibrosis and cancer*", *Cancers (Basel)*, 2021.

Abstracts presented in conferences and meetings as a first author:

- **Oral presentation** at *"European Association for the Study of the liver (EASL) - NAFLD Summit 2022", "Exploring the impact of the genetic PNPLA3 I148M variant on primary human hepatic stellate cells by using healthy and diseased 3D extracellular matrix scaffolds";*
- **Poster presentation** at *"ILC 2022 – The International Liver Congress 2021 – EASL", "Transcriptomic analysis reveals deregulated antifibrotic NR4A1 expression, impaired mitochondrial function and anti-oxidant response in human hepatic stellate cells carrying the PNPLA3 I148M mutation";*
- **Oral presentation** at *"Digital EASL - NAFLD Summit 2021", "The Patatin-like phospholipase domain-containing-3 I148M mutation causes mitochondrial dysfunction and enhances the profibrogenic potential in human Hepatic Stellate Cells";*
- **Poster presentation** at *"ILC 2021 – The International Liver Congress 2021 – EASL", "Implication of the Patatin-like phospholipase domain-containing-3 I148M*

mutation on Hepatic Stellate Cells mitochondrial dysfunction and profibrogenic potential";

- **Poster presentation** at *"ILC2020 – The International Liver Congress 2020 - EASL", "Analysis of PNPLA3 SNP variants in human hepatic stellate cells in 3D human liver extracellular matrix scaffolds reveals key PNPLA3-dependent pro-fibrogenic features";*
- **Poster presentation** at *"AASLD 2019 – The Liver Meeting – American Association for the Study of Liver Disease (AASLD)" (Boston), "Thermo-responsive human liver extracellular matrix three-dimensional hydrogels for modelling liver fibrosis";*
- **Oral presentation** at *"ECLCB 2018 – European Club for Liver Cell Biology" (Bonn)* and at *"TERMIS 2018 - Tissue Engineering and Regenerative Medicine International Society World Congress" (Kyoto), "Primary human Hepatic Stellate Cell phenotype is differently regulated by pro-fibrogenic and pro-inflammatory stimuli in cirrhotic and healthy human liver 3D ECM scaffolds".*

Awards:

- Poster "*Exploring the impact of the genetic PNPLA3 I148M variant on primary human hepatic stellate cells by using healthy and diseased 3D extracellular matrix scaffolds*" included in "Best of NAFLD Summit 2022";
- Poster "*Implication of the Patatin-like phospholipase domain-containing 3 I148M mutation on hepatic stellate cells mitochondrial dysfunction and profibrogenic potential*" included in "Best of ILC2021" at "ILC 2021 – The International Liver Congress 2021 – European Association for the Study of the Liver";
- Best "*3-Minute Thesis Presentation (3MT)*" at UCL Division of Medicine Retreat 2019.

1 General introduction

1.1 Chronic Liver Disease.

Chronic liver disease (CLD) is a leading cause of death worldwide with a number of cases estimated to be 1.5 billion[1]. The most common causes are non-alcoholic fatty liver disease (NAFLD) (59%), chronic HBV (29%) and HCV (9%) infections, and alcoholic liver disease (ALD) (2%)[1].

NAFLD affects approximately 25% of the world's adult population[2], with a percentage of patients progressing to non-alcoholic steatohepatitis (NASH)[3] which can then lead to cirrhosis and hepatocellular carcinoma (HCC)[3]. Various mechanisms have been associated with the progression of NAFLD to NASH, including fat accumulation, lipotoxicity, oxidative stress, mitochondrial dysfunction, inflammation and alterations in the liver-gut axis signalling[4]. Fibrosis stage has been identified as the most important predictor of prognosis in patients with NAFLD[5].

Liver fibrosis is defined as the progressive deposition of fibrillar extracellular matrix (ECM) associated with progressive nodular regeneration of the liver parenchyma leading to cirrhosis. This is due to a chronic wound-healing reaction, which is highly efficient in the presence of a single acute tissue insult but leads to progressive scarring when tissue damage is persistent[6]. Hepatic fibrogenesis can develop into cirrhosis and hepatic failure on average after 15-20 years. Cirrhosis is classified as an advanced stage of fibrosis, characterized by the formation of regenerative nodules of liver parenchyma, which are separated by and encapsulated in fibrotic septa, and associated with major angio-architectural changes[7]. Liver cirrhosis is the most common non-neoplastic cause of death among hepatobiliary and digestive diseases. Furthermore, cirrhosis is largely associated with the development of primary liver cancers such as hepatocellular carcinoma and cholangiocarcinoma[8]. Clinical studies have indicated that fibrosis and even cirrhosis can be regressed when intervening on the primary disease etiology[9]. Nonetheless, approved therapies targeting fibrosis or cirrhosis are still lacking and liver transplantation is currently considered the only treatment option for cirrhosis[10] (Figure 1).

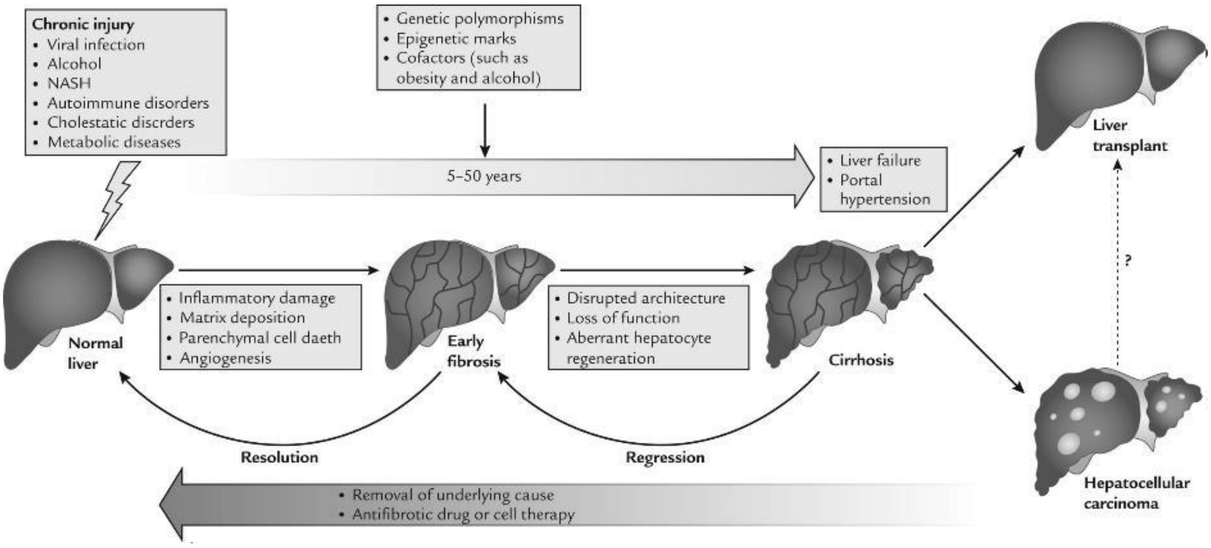

Figure 1: Schematic of chronic liver disease progression. *From A. Muir, “Understanding the complexity of cirrhosis”, Clinical Therapeutics, 2015*

1.2 Hepatic stellate cells and fibrogenesis in chronic liver disease.

Although fibrogenesis is a common hallmark in the development if any chronic liver disease, the specific aetiology can have an impact on the development of distinct morphological patterns of fibrosis. For instance, in NAFLD and ALD excess ECM deposition is initially localized mainly around the sinusoids and groups of hepatocytes, while in HCV and HBV the increased deposition of ECM is initially observed around the portal-central vein and results in portal-central bridging necrosis. These patterns depend on different factors, such as the location of liver injury, the pro-fibrogenic factors concentration in the liver microenvironment and the specific cellular origin of myofibroblasts, the key cells in hepatic fibrogenesis development[11]. Studies performed over the past four decades have shown that the major source of hepatic myofibroblasts in patients and models of chronic liver disease are activated hepatic stellate cells (HSCs)[12,13].

Hepatic stellate cells in healthy livers are vitamin A storing cells located around the sinusoids in the space of Disse, and therefore also addressed as liver-specific pericytes[12]. Quiescent HSCs undergo a phenotypical modulation into myofibroblast, losing their vitamin A droplets, in response to several micro-environmental disturbances[14]. Among these, the release of cytokines and chemokines by platelets and inflammatory cells[15], release of damage-associated reactive oxygen species (ROS), generation of lipid peroxides and apoptotic bodies by damaged hepatocytes[16,17] and major disturbance of the ECM homeostasis in the space of Disse[18]. This first phase of HSCs activation is called initiation, and it is featured by a strong crosstalk between HSCs and liver sinusoidal endothelial cells (LSEC). In this phase HSCs start proliferating and accumulating collagen in the space of Disse. The initiation phase is followed by perpetuation, characterized by HSCs starting to produce cytokines also acting in an autocrine manner, maintaining their activation and survival and the associated ECM deposition[12]. A third phase, regression, occurs only if the cause of hepatocellular damage ceases either spontaneously (i.e., resolution of an acute viral hepatitis) or following therapeutic intervention when feasible. In this case, HSCs undergo a process which can involve apoptosis, senescence, or the conversion to a lesser activated phenotype i.e., the so-called inactivated or deactivated HSC[13] (Figure 2).

Due to their key role in fibrogenesis, many therapeutic strategies targeting liver fibrosis have been focusing on cell-membrane, cytoplasmic and nuclear molecules that are involved in HSCs activation. For instance, many substances targeting PPARα, PPARγ, PPARδ, FXR, CCR2 and CCR5 are currently in phase II and III clinical trials as anti-fibrotic drugs[13]. In addition, there has been growing interest in targeting the RhoA/RhoKinase pathways in HSCs to decrease their contractile phenotype, and thus ameliorate portal hypertension[19]. Nonetheless, a safe and efficient therapy to reduce fibrosis and improve chronic liver disease has still to be found.

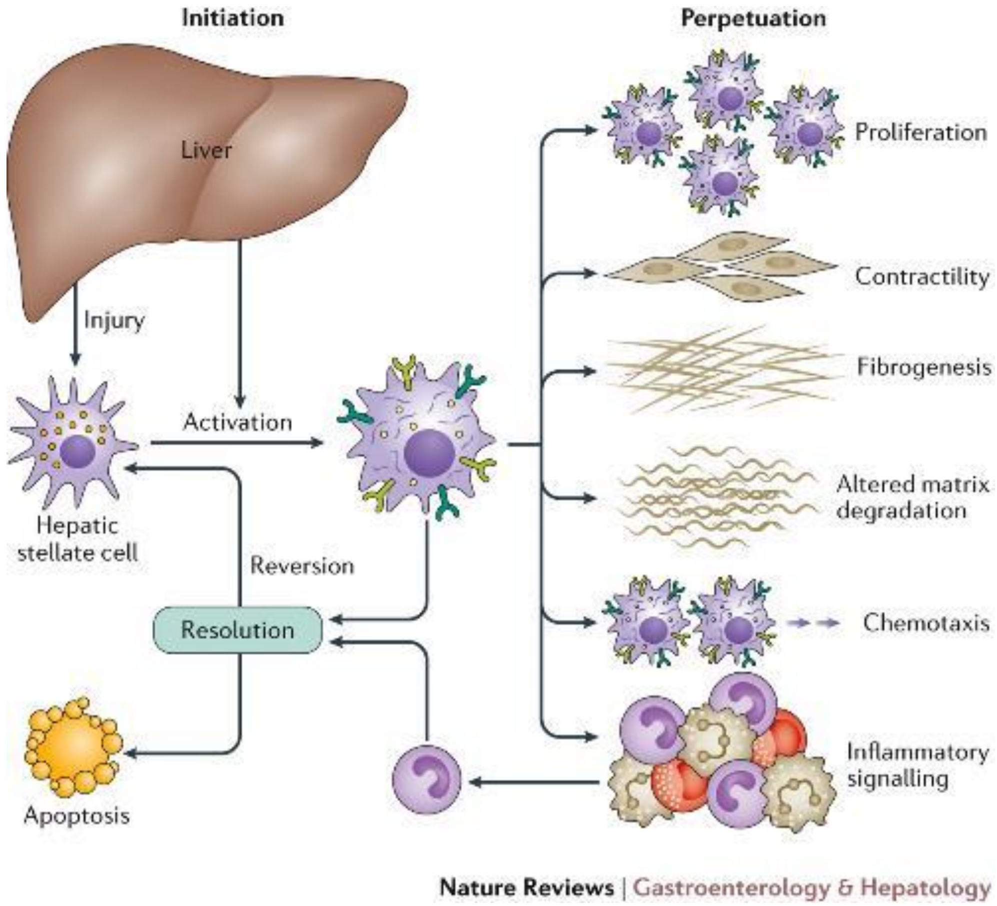

Figure 2: Hepatic stellate cells activation. *Tsuchida, T. & Friedman, S. L. (2017) "Mechanisms of hepatic stellate cell activation" Nat. Rev. Gastroenterol. Hepatol.*

1.3 Liver extracellular matrix.

In all tissues, the most common ECM-producing cells are myofibroblasts. It is well known that HSCs produce significantly larger amounts of collagen and ECM proteins than hepatocytes and endothelial cells *in vitro*, and therefore, as mentioned above, activated HSCs are considered the major source of myofibroblasts in the liver[12]. In addition, some myofibroblasts may also derive from portal myofibroblasts, or from bone marrow cells (fibrocytes)[20,21]. However, *in vivo* studies in mice confirmed that HSCs give rise to 82-96 % of myofibroblasts in models of toxic, cholestatic and fatty liver disease.

Liver ECM is composed by several families of molecules such as collagens, non-collagenous glycoproteins, proteoglycans, glycosaminoglycans, growth factors, integrins and matricellular proteins[22]. In healthy livers, ECM comprises approximately

0,5 % of the total liver weight, with fibrils such as collagen type I, III, V and XI found only in the capsule and the portal triad, and only scattered fibres present in the subendothelial space[23]. Some of the proteoglycan proteins such as decorin and byglican can bind growth factors and other molecules such Transforming Growth Factor β (TGFβ or TGFB), turning the ECM into a local storing site for these molecules[24]. Furthermore, ECM homeostasis is maintained by a constant turnover of its proteins, a well-defined, fine balance between matrix metalloproteinases (MMPs), which can degrade ECM, and tissue inhibitors of metalloproteinases (TIMPs)[25]. Under repeated injury conditions, this balance is compromised, with TIMPs production prevailing over MMPs synthesis, and continuous ECM production. This promotes chronic vascular remodelling and enhanced ECM crosslinking that eventually leads to fibrosis and inability of the tissue to heal properly[26].

1.4 Current hepatic models for pre-clinical studies.

Until recently, most of the potential drugs for liver disease have been tested in traditional 2D monolayer cultures. The process of investigating pharmacokinetics and performing toxicological studies can though be very challenging and many lead to unreliable results. Indeed, in many cases, drug candidates that showed efficacy when tested in different 2D *in vitro* systems did not reproduce similar successful effectiveness in *in vivo* animal models[27,28]. The main pitfall of 2D models is the lack in resembling the natural hepatic 3D microenvironment, which enables parenchymal and non-parenchymal cells to maintain their physiological features[29].

For instance, HSCs when cultured on non-coated polystyrene dishes in the presence of foetal bovine serum spontaneously activate and transdifferentiate into an activated myofibroblasts-like cell, typical of a diseased liver[12]. On the other hand, it is well-know that there are differences between *in vitro* cultured activated HSCs and *in vivo* activated HSCs. Recent studies showed that many genes are differently expressed in *in vitro* cultured activated cells and *in vivo* activated HSCs, such as genes involved in proliferation, cell survival, cytoskeletal organization and contraction, inflammation, ECM organization and degradation, lipid metabolism, and several transcription factors[30].

Therefore, animal models have until now been essential for drug discovery since they can overcome many of the 2D models' drawbacks. Indeed, they combine the native ECM microenvironment, different cell types, oxygen, and nutritional flows[31], but have many limitations as well. Being of non-human origin, they show significant differences in metabolic capacities, cytochrome P450 isoforms activity, physiology, drug half-life and availability and disease adaptive mechanisms[28,32]. Consequently, 9 out of 10 drugs that passed animals trials i.e., pre-clinical trials, ended up failing during human clinical trials[33].

All these points lead to the necessity of optimizing *in vitro* tissue-specific models for a successful investigation of liver cell behaviour and drug discovery. These models should have preferably a 3D aspect, contain organ specific ECM[34], and be able to mimic ECM structures as found *in vivo*[35].

1.5 Traditional 3D *in vitro* hepatic systems.

As mentioned above, there are several aspects that are important for natural cell behaviour and that are missing in common 2D models: tissue-specific cell-cell interactions, tissue-specific cell-ECM interactions, tissue-specific architecture, nutrients and oxygen gradients.

The *in vitro* culture of HSCs can serve as a good example of how these aspects can influence cell behaviour in 2D compared to 3D cultures. In fact, HSCs activation is strikingly induced by the culture on plastic, which has a stiffness of ~2GPa, compared to culture on softer materials which resemble the natural liver 3D environment and therefore have a lower stiffness of 1-20 kPascal[36,37]. In recent years, many efforts have been made to develop well-defined 3D *in vitro* models, able to mimic ECM features and structure as found *in vivo*[35] (Figure 3). All these models try to recreate the hepatic microenvironment, and all share advantages and disadvantages. Among them, it is worth mentioning organs on a chip[38], cell spheroids[39], Precision Cut Liver Slices[40], cell sheets[41,42] and 3D matrix synthetic scaffolds[34,36,37].

- Organs on a chip: these systems use microfluidic or microscale bioreactors to control the flow of culture medium. For instance, Liver-on-a-chip can be composed by a scaffold that fosters formation of a 3D tissue structure where different hepatic cell types are cultured, connected with an on-board microfluidic pumping system. Therefore, viability and behaviour of the cells can be maintained for a long time thanks to the perfusion and constant recirculation of culture medium in each well, which allows controlled oxygenation and shear stress[43]. A promising feature of these systems is the possibility to develop multi organ chip-based systems, with controlled medium flow through different engineered tissues that are interconnected and thus resemble the crosstalk between different organs in the human body[44].

- Cell spheroids: multicellular cluster of cells allowing ECM production, cell-cell and ECM-cells interactions. Cell spheroids allow the development of 3D hepatocytes cultures and of multicellular cultures[39,45] which better resemble the microenvironment of the human liver. Limitations of this model include the variability of spheroids size which affects the data reproducibility during drug efficacy and toxicity studies[46].
- Precision Cut Liver Slices (PCLS): can be obtained from different species such as rat[47] mouse[48] and human liver[40]. They are 8 mm in diameter, 250 um thick and contain 70 to 100 lobules. PCLS are maintained in a vial on a roller platform, gently agitated in a humidified incubator. Experiments can be performed over a period of 24h to 1 week, allowing the investigation of hepatocytes and all the other nonparenchymal cells behaviour. On the other hand, the major drawback of this system is that the incubation time is quite short, and the outcomes are different depending on the species that is chosen[49].
- Cell sheets: method based on the usage of poly(N-isopropylacrylamide) (PNIPPAAm)-grafted-temperature-responsive cell culture dishes. Basically, these dishes have a PNIPPAAm gel implanted that change features between hydrophobicity and hydrophilicity according to temperature, allowing cell detachment without breaking cell-cell interactions. The cell sheets can then be assembled to build 3D structures[41,42]. The total absence of vascularisation and therefore oxygen supply in the model only allows to use it in short-term cultures.

- 3D matrix synthetic scaffolds: can be made from synthetic or biological sources. Synthetic scaffolds can be obtained using polymers like polylactidecoglycolide (PLG), polyethylene glycol (PEG), polycaprolactone (PLA)[50] or naturally-derived hydrogels (alginates, cellulose, polyethylene)[51]. Furthermore, biological ECM-derived material, as basement membrane or collagen I can be used. Although the latter are characterized by the preservation of ECM molecules, the tissue microarchitecture is not preserved, thus not allowing the maintenance of specific liver metabolic functions.

As ECM is a fundamental feature in liver microarchitecture, our lab has focused on the development of ECM-based 3D models, starting from the decellularization of human livers to produce scaffolds and hydrogels.

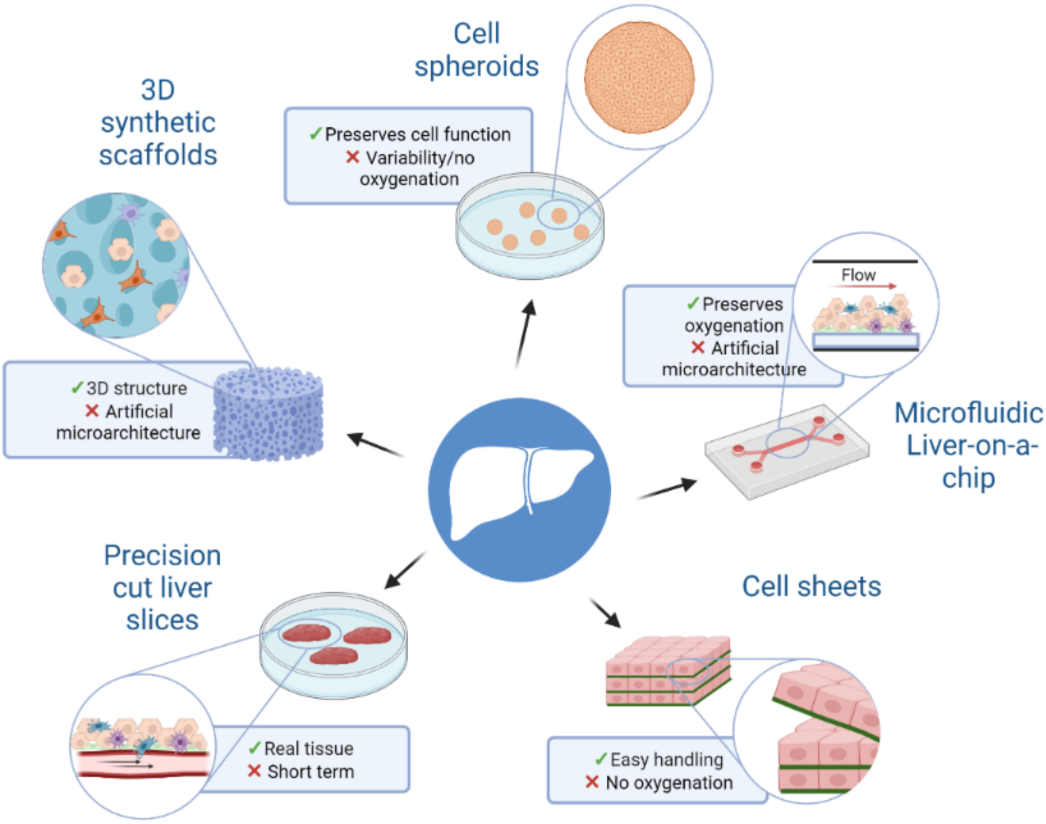

Figure 3: Summary of three-dimensional platforms utilized for liver disease modelling. *Created with Biorender.*

1.6 Genetic variants in chronic liver disease.

The importance of genetics in the understanding of chronic liver disease has become increasingly evident in the last few decades. In fact, the development of novel genomic technologies has allowed the identification of unknown genetic risk factors responsible or contributing to the development of liver disease[52]. The first gene mutations to be discovered were those responsible for the onset of monogenic diseases, where a variation in a single gene alone is the cause of the condition. Among those, the mutation in the ATP7B gene leading to Wilson disease was discovered in 1993[53], the hemochromatosis responsible variations in the HFE gene in 1996[54], and the α1-antitrypsin deficiency responsible mutation in the SERPINA1 gene in 1978[55]. Later, genome-wide association studies (GWAS) enabled scientists to discover gene variants involved in polygenic diseases, where the mutation is not the only determinant in the onset of the disease but confers incremented susceptibility to its development. The first GWAS in hepatobiliary diseases identified the single nucleotide polymorphism (SNP) in the ABCG5/G8 gene as a major susceptibility factor for gallstone disease[56], and later several genetic factors involved in the development of autoimmune liver disease were discovered[57]. In recent years, the increased incidence of NAFLD and NASH in the general population has prompted the conduction of several GWAS studies which have identified numerous SNPs involved in the development of fatty liver disease. Among those, the mutations in the PNPLA3[58] and TM6SF2[59] genes, which have been also associated with the progression to HCC[60], and the genetic variants in the MBOAT7[61] and GKCR[62] genes. The variant in the HSD17B13 gene was instead found to be protective towards chronic liver disease[63]. The increasing insights in genetic factors contributing to the development of chronic liver disease and the decreasing cost of genomic assays is slowly allowing the integration of genomics as a tool in clinical medicine, which could help in a faster diagnosis of unexplained liver disease[64]. Furthermore, knowledge on genetic variants involved in liver disease is facilitating the optimization of more accurate disease models[43] and treatment drugs[65].

2 Aims and Objectives.

The aim of this project is to utilize and optimize an *in vitro* 3D model based on decellularized ECM from human liver to investigate the impact of different genetic mutations on the pro-fibrogenic behaviour of hepatic stellate cells (HSCs).

This aim will be addressed by achieving the following objectives:

i. Comparison of the transcriptomic analysis of primary human HSCs and patients with NAFLD genotyped and classified by the presence of the PNPLA3 I148M variant.

ii. Validation of the target pathways and genes identified from the comparative transcriptomic analysis in a 3D *in vitro* model where primary HSCs carrying or not the PNPLA3 I148M variant will be cultured on decellularized healthy or cirrhotic human liver scaffolds.

iii. Further exploration of pathways identified by transcriptomic analysis and molecular mechanisms driving the regulation of identified target genes.

iv. Optimization of the scalability of the 3D ECM *in vitro* model with the production of ECM hydrogels for the culture of HSCs.

v. Validation of the ECM hydrogel platform for the modelling of liver fibrosis and study of genetic variants in HSCs by investigating the effect of the combination of PNPLA3 I148M and TM6SF2 E156K mutations on cells behaviour.

3 Exploring the impact of the genetic PNPLA3 I148M variant on primary human hepatic stellate cells by using 3D extracellular matrix models

3.1 Introduction.

3.1.1 The PNPLA3 I148M genetic variant in hepatic stellate cells and liver disease.

As mentioned above, genetic variants are a major determinant of the risk of development and progression of NAFLD and important in other chronic liver diseases[66]. Among them, the most robustly characterized and the one that accounts for the largest fraction of disease heritability[58] is the I148M variant of the PNPLA3 gene, which has been associated with liver fat accumulation, hepatic inflammation, and susceptibility to develop steatohepatitis[67]. Patatin-like phospholipase domain-containing 3 (PNPLA3, also called adiponutrin, ADPN) is a membrane-bound protein with lipase and transacylase activity towards triglycerides/phospholipids in hepatocytes and retinyl esters in HSCs[68,69]. PNPLA3 is highly expressed in HSCs, where it is regulated by retinol availability, and involved in lipid droplet remodelling, promoting the extracellular release of retinol[70]. Several studies have proven the association between I148M PNPLA3 and the development and severity of liver fibrosis, which might be at least partially independent from the predisposition to hepatic fat accumulation. Further, the I148M PNPLA3 has been associated with HCC development[70–72]. Previous studies have shown how the PNPLA3 I148M variant facilitates HSCs activation and how its expression is associated with a pro-fibrogenic, myofibroblast-like phenotype characterized by an increased release of pro-inflammatory and pro-fibrogenic cytokines, enhanced proliferation and migration compared to the wild type PNPLA3[43,73]. Although the presence of the PNPLA3 I148M variant in HSCs has been associated with deregulation of Yap signalling[74] and cholesterol metabolism[75], a comprehensive overview of the different mechanisms driving the progression of liver disease via PNPLA3 variants has still to be provided. A disadvantage in analysing the effects of the PNPLA3 variant is the lack of adequate pre-clinical models. Although mice models carrying the *PNPLA3* I148M variant have been generated and show hepatic fat accumulation[76–78], they present a key difference with humans in the tissue expression and distribution of *PNPLA3*, which is the highest in adipose tissue in mice[79] compared to the liver in humans[80]. On the other hand, the most common used human cell lines (HepG2 and LX2) are already carriers of the PNPLA3 I148M mutation, thus hampering the possibility of observing differences between a wild-type and mutant genotype[81].

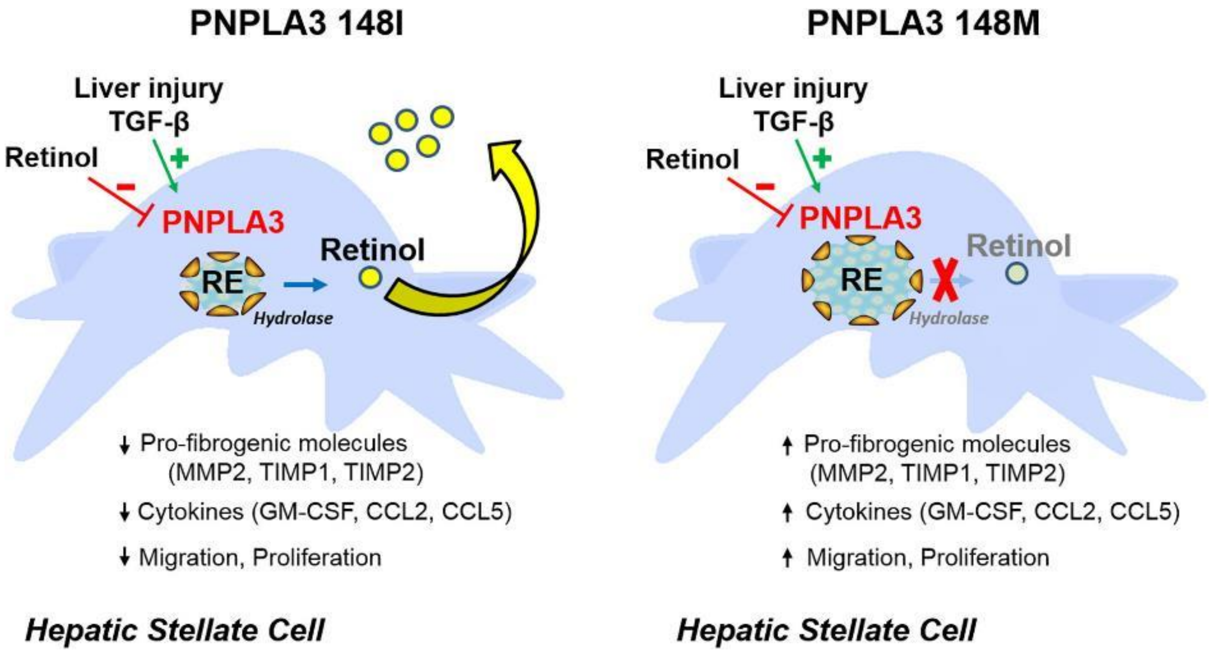

Figure 4: Role of PNPLA3 in HSCs. *From Pingitore, Romeo "The role of PNPLA3 in health and disease", BBA – Molecular and cell biology of lipids, 2019*

3.1.2 Decellularized liver ECM scaffolds as three-dimensional *in vitro* models.

Biological scaffolds have now long been attractive in the field of tissue engineering and disease modelling for their biocompatibility, bioactivity and capacity to support cells[82]. Among those, decellularized scaffolds refer to biomaterials formed by human or animal organs, or tissue subjected to decellularization. Decellularization is the process of removing cellular and immunogenic materials from tissues and organs whilst maintaining the mechanical and bioactive properties of the tissue[83]. According to the source of ECM, decellularized scaffolds can be classified as organ/tissue-derived scaffolds or cell-derived scaffolds. Cell-derived decellularized ECM scaffolds are easy to produce and guarantee the possibility of deriving ECM from specific types of cells reducing the risk of pathogen transfer caused by tissue/organ derived scaffolds. On the other hand, the latter have the advantage of preserving the natural

3D architecture of the whole tissue or organ, which is important to regulate cell adhesion, proliferation and differentiation. Furthermore, because native ECM binds several growth factors and tissue-specific cues, tissue/organ decellularized scaffolds can retain tissue-specific memory which can drive tissue-specific cell differentiation. The preservation of the natural 3D microarchitecture means that mechanical properties of the tissue are also preserved, contrary to what happens in cell-derived decellularized scaffolds[82].

Recently, a study in our laboratory of Regenerative Medicine and Fibrosis, Institute for Liver & Digestive Health, established a new protocol for decellularizing small-scale human tissue for application in 3D *in vitro* models of liver diseases[36].

The newly described protocol allows the removal of immunogenic cellular materials, and, at the same time, preservation of the key ECM proteins in the cell-free scaffold and comparability of the ECM micro-architecture with that of the native tissue[36]. Thanks to these features, both parenchymal and non-parenchymal cells are able to engraft and to maintain their differentiation and functionality when seeded on Acellular Liver Tissue Cubes (ALCTs)[36]. Therefore, these human liver ECM 3D scaffolds represent a unique biomaterial which can be useful to understand the role of ECM in modulating cell phenotype and its role in liver fibrosis.

3.2 Materials and Methods.

3.2.1 Study population and genotyping.

The cohort of patients was formed of 116 obese individuals and previously characterized in the study by Baselli et al[84]. Briefly, patients underwent percutaneous liver biopsy performed by needle gauge during bariatric surgery, with individuals with at-risk alcohol intake (>30/20g/day in M/F), viral and autoimmune hepatitis or other causes of liver disease excluded from the study. Steatosis was graded based on the percentage of affected hepatocytes; disease activity was assessed according to the NAFLD Activity Score (NAS); fibrosis was staged according to the recommendations of the NAFLD clinical research network[85]. NASH was defined as the concomitant presence of steatosis, lobular inflammation, and ballooning. Clinical features of the cohort can be found in Table 1.

	PNPLA3 I148M II (WT) (N=60)	PNPLA3 I148M IM (I148M) (N=56)	p-value
Age	43.42±10.2	43.84±10.8	0.83
Sex, F	51	48	0.91
BMI, Kg/m2	40.80±6.1	40.56±8.5	0.86
Severe NAFLD, Yes	12	16	0.91
NAFLD, Yes	50	47	0.38
Diabetes, Yes	6	7	0.66
ALT, U/L	20 {15-26.75}	21 {15-31}	0.75
AST, U/L	18 {15-22.75}	17 {15-22}	0.73
Steatosis grade 0/1/2/3	10/29/11/10	9/18/16/13	0.28
Inflammation grade 0/1/2/3	32/26/2	28/20/8	0.10
Ballooning grade 0/1/2	55/5/0	48/7/1	0.43
Fibrosis stage 0/1/2/3/4	42/18/0/0/0	35/14/4/1/1	0.13
Cholesterol, mg/dL	212.56±43.6	208.76±44.20	0.50
LDL, mg/dL	130.52±36.6	132.60±38.2	0.76
HDL, mg/dL	56.88±14.1	52.05±14.2	0.06
Triglycerides, mg/dL	110 {81-140}	121 {88.25-179.8}	0.32

Table 1. Clinical features of patients analysed in the Human RNAsequencing dataset and stratified for PNPLA3 I148M genotype. *Data are presented as mean±SD, {}: interquartile range. Comparisons were performed by generalized linear models (Welch's test, Mann-Whitney test and Chi-quare test), and non-normally distributed variables were log-transformed before the analysis.*

The genotype of liver biopsies was determined by Taqman 5'-nuclease assays for the rs738409 C>G (PNPLA3 I148M) single-nucleotide polymorphism (Life Technologies, Carlsbard, USA).

The genotyping classified the study population as follows: PNPLA3 I148M CC (WT): n=60, PNPLA3 I148M CG (heterozygous mutant): n=56, PNPLA3 I148M GG (homozygous mutant): n=9. For the purpose of this study, only the PNPLA3 I138M CC and PNPLA3 I148M CG groups were included in the bioinformatics functional analysis.

3.2.2 Primary human HSCs isolation and culture.

Human primary HSCs were isolated according to Rombouts et al., (REC reference 21/WA/0388)[86]. Cells were cultured in Iscove's Modified DMEM (IMDM, Thermo Fisher Scientific, Watlham, USA), supplemented with 20% foetal bovine serum (FBS, Thermo Fisher Scientific, Watlham, USA), 2 mM Glutamine, 1X non-essential amino acids, 1.0 mM sodium pyruvate, 1X antibiotic-antimycotic (Life Technologies, Carlsbard, USA), and maintained under standard conditions in a humidified incubator under 5% CO_2 in air at 37°C. Medium was refreshed twice a week and cells were passaged when subconfluent with 1X Trypsin (Gibco, Thermo Fisher Scientific, Watlham, USA). Experiments were performed on cell preparations used between passage 5 and 8.

3.2.3 DNA extraction and genotyping of primary human HSCs.

DNA was extracted from different HSCs donors using DNA Blood and Tissue Extraction Kit (Qiagen, Hilden, Germany) and subsequently used for genotyping. The genotype of each isolated HSC donor was determined by real-time PCR for the rs738409 C>G (PNPLA3 I148M) single-nucleotide polymorphism using a TaqMan SNP Genotyping Assay (Life Technologies, Carlsbard, USA).

3.2.4 Whole transcriptome amplification and RNA sequencing (NGS).

Bulk transcriptomic analysis of liver biopsies was performed by NGS as described in the study by Baselli et al.[84]. Briefly, RNA from human tissue was sequenced in paired-end mode (read length 150nt) using the Illumina HiSeq 4000 (Novogene, Hong Kong, China). Reads were mapped by a custom pipeline[87] encompassing reads quality check (FastQC software, Babraham Bioinformatics, Cambridge, UK), low-quality reads trimming and mapping on GRCh37 reference genome by STAR mapper[88]. Reads count (ENSEMBL human transcript reference assembly v75) was performed using RSEM package[89]. Counts were normalised using DESeq2 package[90].

NGS of primary human HSCs (n=3 per each genotype) was performed as previously described[91]. Briefly, samples were sequenced on the NextSeq 500 instrument (Illumina, San Diego, USA) using a 75bp single read run with a corresponding 8bp unique molecular identifier (UMI) read. Samples were sequenced over 1.5 NextSeq 500 runs. Run data were demultiplexed and converted to fastq files using Illumina's bcl2fastq Conversion Software v2.19. Fastq files were then aligned to the human genome UCSC hg38 using RNA-STAR 2.5.2b then UMI deduplicated using Je-suite (1.2.1). Reads per transcript were counted using FeatureCounts and differential expression was estimated using the BioConductor package SARTools, a DESeq2 wrapper. All annotation and sequences were obtained from Illumina iGenomes (http://emea.support.illumina.com/sequencing/sequencing_software/igenome.html). Library preparation and sequencing was performed at UCL Genomics, Zayed Centre for Research into Rare Disease in Children, UCL.

3.2.5 Bioinformatics functional analyses.

After statistical analysis, differentially expressed genes within groups were studied using Ingenuity Pathway Analysis (IPA - Qiagen, Hilden, Germany). IPA is a functional analysis tool for omics data which takes into consideration both significance and fold change of the differentially expressed gene to provide:

-*Canonical Pathway Analysis:* indicates which metabolic and cell signalling pathways show a significance of enrichment for a group of genes;

-*Upstream Regulator Analysis:* identifies upstream regulators by using published experimental molecular interactions and determining gene enrichment in downstream genes; it also predicts their activity state by correlating literature reported effects with observed gene expression;

-Disease and Biofunction Analysis: identifies key biological processes influenced by differentially expressed genes and understands whether they are being driven up or down by correlating observed expression with reported experimental gene effects.

For both Human Tissue dataset and Primary HSCs dataset, differentially expressed genes were used as input for IPA analysis and then filtered for analysis focusing on only statistically significant ($p<0.05$) genes with $-0.3785 \leq \log2(\text{fold change}) \geq 0.3785$. Pathways or Biofunctions analysis and Upstream Regulators networks were generated and ranked in terms of significance of participating genes ($p<0.05$) and activation status (Z-score) per each single data set. Specifically, in the Primary HSCs dataset, Canonical Pathways had $-0.5 \leq$ Z-score ≥ 0.5, Disease and Biofunctions had $-3\leq$ Z-score ≥ 3 and Upstream Regulators had $-2.5 \leq$ Z-score ≥ 2.5. Afterwards, Pathways or Biofunctions and Upstream Regulators were compared between the two data sets and common Pathways, Biofunctions or Upstream Regulators were selected according to their Z-score (going in the same direction, either > 0 or < 0, and therefore either upregulated or downregulated for both datasets) and their p-value ($p<0.05$ for both datasets). Specifically, Canonical Pathways had $-1 \leq$ Z-score ≥ 1 for at least one dataset and going in the same direction for the other dataset; Disease and Biofunctions had $-4 \leq$ Z-score ≥ 4 for at least one dataset and going in the same direction for the other dataset; predicted Upstream Regulators had $-4 \leq$ Z-score ≥ 4 for at least one dataset and going in the same direction for the other dataset. Common target genes between the two datasets were selected in a similar manner (log2(fold change) going in the same direction and FDR<0.05/p-value<0.05 in both data sets). All the raw data and analysis can be provided upon request.

3.2.6 Preparation of 3D human liver scaffolds.

Livers were obtained after approval by the UCL Royal Free BioBank Ethical Review Committee (NRES Rec Reference: 21/WA/0388). Informed consent was obtained for each donor and confirmed via the NHSBT ODT organ retrieval pathway. Healthy human livers were retrieved for transplantation but judged unsuitable due to prolonged cold ischemic time, the presence of extra-hepatic cancer, or other significant extra-hepatic diseases in donors or recipients. Cirrhotic liver was explanted from a patient with alcoholic cirrhosis. Healthy liver was defined if there was no evidence of fibrosis and fat accumulation. 3D human liver scaffolds were prepared (Table 2) and quality control (Figure 5) was performed according to the methodologies developed by Mazza G et al.[36,37]. 3D human liver scaffolds were then sterilized using 0.1% peracetic acid (PAA, Sigma-Aldrich, St. Louis, USA) and repopulated with primary HSCs as previously described[36].

Reagent	Frequency (Hz)	Duration (min)	Repetitions
Healthy liver scaffold			
Deionized Water	20	2	5
Deionized Water	25	2	5
Deionized Water	30	2	5
Reagent Mix	20	2	1
Deionized Water	20	2	10
Phosphate Buffered Saline (1X)	20	5	3
Cirrhotic liver scaffold			
Deionized Water	20	2	20
Reagent Mix	15	2	1
Reagent Mix	15	4	2
Deionized Water	15	2	20
Reagent Mix	15	2	1
Reagent Mix	15	4	2
Deionized Water	15	2	20
Phosphate Buffered Saline (1X)	15	5	3

Table 2: Decellularization protocol.

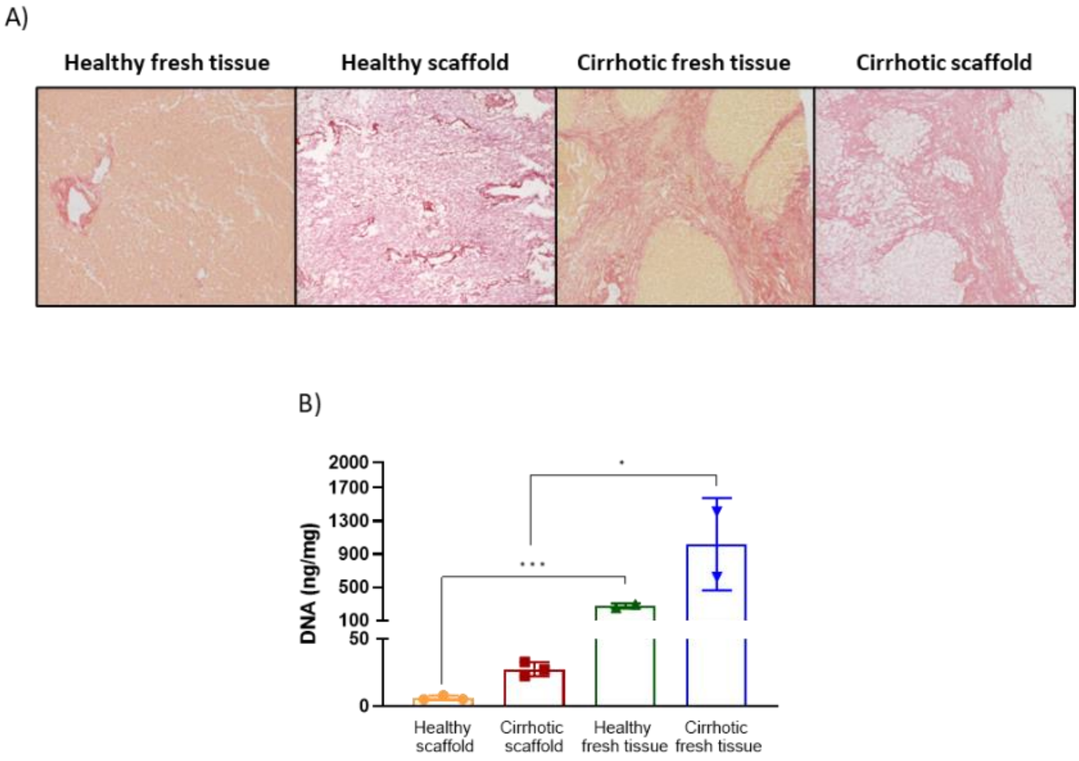

Figure 5:* *Decellularized human liver scaffolds quality control. *(A) Sirius Red staining of healthy and cirrhotic liver tissue before (fresh) and after decellularization process (scaffolds) (10x magnification). (B) Quantification of DNA content in healthy and cirrhotic liver tissue before (fresh) and after decellularization process (scaffolds) (N=3 biological replicates for liver scaffolds and N=2 biological replicates for liver fresh tissue; data analysed with Student t-test).*

3.2.7 Primary human HSCs culture on 3D human liver scaffolds or 2D.

Cells were cultured in the liver scaffolds for a total of 13 days. After 7 days of culture, cells were treated with either TGFB1 (5 ng/mL) (R&D Systems, Minneapolis, USA) alone for 3x48 hours, to create a chronic profibrotic microenvironment, or TGFB1 (5 ng/mL) with Csn-B (1 or 5 µM) (Merck, Rahway, USA) for 3x48 hours in Serum Free Medium (SFM). In parallel, cells were grown in 2D culture and, after 24 hours in SFM, cells were treated with TGFB1 (5 ng/mL) for 3x48 hours, and the experiment was terminated at day 6.

3.2.8 Histology and Immunostaining analysis.

Liver scaffolds samples were fixed in 10% formalin for 24 hours, processed and embedded in paraffin. Embedded samples were cut in 4µm thick sections, deparaffinized in xylene and rehydrated in alcohol before staining. Tissue sections were stained with Harris Haematoxylin and Eosin (H&E) (Leica, Wetzlar, Germany) or subjected to immunohistochemistry. For immunostaining, samples were retrieved with sodium citrate buffer (pH 6.0) in a microwave (640W) for 10 minutes. Nonspecific binding was blocked with normal horse serum (VECTASTAIN®, Vector Laboratories, UK) for 5 min at RT. Sections were incubated for 1 h at RT with primary antibodies (Table 3). After washing, sections were incubated with pre-diluted biotinylated pan-specific universal secondary antibody (VECTASTAIN®, Vector Laboratories, Burlingame, USA) for 30 min. Primary antibodies were detected with the Novolink™ Kit (Novocastra, UK). Slides were counterstained with haematoxylin, dehydrated, cleared, and mounted. Images were captured using Axiocam IcC5.

Antibody	Species	Catalogue number	Company	Dilution
NR4A1	Rabbit	HPA070142	Sigma Aldrich	1:50
NR4A1 (Phospho S351)	Rabbit	ab111962	Abcam	1:200

Table 3: Antibodies used for immunohistochemistry staining.

3.2.9 Viability assay.

PrestoBlue assay (Thermo Fisher Scientific, Watlham, USA) was used to assess cell viability according to the manufacturer's protocol and as previously described[92]. Fluorescence intensity at 600 nm was quantified (Fluostar Omega Plate reader, Bmg Labtech, Ortenberg, Germany).

3.2.10 RNA extraction, complementary DNA (cDNA) synthesis and quantitative real time PCR (RT-qPCR).

RNA was extracted from 3D scaffold samples and 2D samples using RNeasy® Plus Universal Mini Kit (Qiagen, Hilden, Germany) according to the manufacturers' protocol. RNA concentration and purity was measured with Nanodrop spectrophotometer (Thermo Fisher Scientific, Watlham, USA). Reverse transcription from mRNA to cDNA was performed using the High Capacity cDNA Reverse Transcription Kit (Applied Biosystems®, Watlham, USA). RT-qPCR analysis was performed using specific TaqMan Probes (Table 4) for the different human target genes (Applied Biosystems®, Watlham, USA). The comparative CT method[93] was used to quantify relative gene expression, using either Glyceraldeyde-3-phospate dehydrogenase (GAPDH) or 18S ribosomal RNA (18S) as an internal control.

Gene name	Gene abbreviation	Taqman gene assay number
Ribosomal protein S18	RP18S	Hs01375212_g1
Alpha 2 smooth muscle actin	Acta2	Hs05005341_m1
Bone morphogenetic protein 1	Bmp1	Hs00241807_m1
Cytoglobin B	CygB	Hs00370478_m1
Collagen Type 1, alpha 1 chain	Col1A1	Hs00164004_m1
EGF containing fibulin like extracellular matrix protein 1	Efemp1	Hs00244575_m1
Glyceraldehyde-3-phosphate dehydrogenase	Gapdh	Hs02786624_g1
Kelch like ECH associated protein 1	Keap1	Hs00202227_m1
Interleukin 1 beta	Il1β	Hs01555410_m1
Interleukin 6	Il6	Hs00174131_m1
Lysyl oxidase	Lox	Hs00942480_m1
Nuclear receptor subfamily 4 group A member 1	Nr4a1	Hs00374226_m1
Nuclear receptor subfamily 4 group A member 2	Nr4a2	Hs01117527_g1
Nuclear receptor subfamily 4 group A member 3	Nr4a3	Hs00545007_m1
Nuclear factor, erythroid 2 like 2	Nrf2	Hs00975960_m1
Prostaglandin-endoperoxide synthase 2	Ptgs2	Hs00153133_m1
Serpin family E member 1	Serpin1	Hs00167155_m1
Serum/glucocorticoid regulated kinase 1	Sgk1	Hs00178612_m1
Snail family transcriptional repressor 1	Snai1	Hs00195591_m1
Transforming growth factor β1	Tgfβ1	Hs00990133_m1
Valyl-tRNA synthetase 2, mitochondrial	Vars2	Hs00383681_m1

Table 4: Applied Biosystem Taqman gene expression assays used for qPCR

3.2.11 Nanostring analysis.

Total mRNA was purified from liver scaffolds-cultured HSCs and multiplexed using the nCounter® analysis system (Nanostring Technologies, Seattle, USA) combined with the nCounter®Human Fibrosis Panel which includes 770 genes covering core pathways defining human fibrosis. Briefly, 62 ng total RNA per sample (n=3 WT or PNPLA3-148M and n=3 healthy or cirrhotic scaffolds) was loaded and hybridized with probes for 16h at 65C following the manufacturer's protocol. Counts for target genes were normalized to the best fitting house-keeping genes as determined by Nanostring™ nSolver software v4.0 to account for variation in RNA content. The background signal was calculated as the mean value of the negative hybridization control probes. The expression data were excluded when they had lower than average background signals from the negative controls, and less than 20 counts. Significant genes were identified by differential expression analysis which calculates a t-statistic for each gene against each covariate in the model; p-value was adjusted by Benjamini-Yekutieli correction. Gene Set Analyis (GSA) was performed by using Nanostring™ nSolver software v4.0. Raw data of all differentially expressed genes can be provided upon request.

3.2.12 Flow Cytometry Analysis.

Proliferation of primary HSCs was evaluated by flow cytometry using Cell Proliferation Staining Reagent – Cytopainter (Abcam, Cambridge, UK). Briefly, HSCs were stained with Cytopainter 1x and then subcultured on plastic; after 7 days, cells were trypsinized and labelled with Live/Dead blue fluorescence dye (Life Technologies, Carlsbad, USA). Cells were analysed by fluorescence-activated cell sorting (FACS) using a BD Fortessa II instrument (BD Biosciences, Franklin Lakes, USA). Samples were examined by side scatter area (SSC-A) *versus* forward scatter area (FSC-A), then using forward scatter height (FSC-H) *versus* FSC-A to select single cells and eliminate clumps of cells from the analysis. Alive cells were selected by subgating for Live/Dead staining and subsequently, amount of Cytopainter fluorescence in cells collected at day0 and at day7 was measured to evaluate proliferation. After acquisition, data were exported and analyzed using FlowJo (FlowJo, LLC, Ashland, USA).

3.2.13 Protein extraction and quantification.

HSCs cultured on 2D or liver scaffolds were lysed with radio-immunoprecipitation assay (RIPA) buffer (Sigma Aldrich, St. Louis USA) supplemented with 1mM phenylmethylsulfonyl fluoride, 1X Protease Inhibitors Mix, 1mM Na_3VO_4 and 1mM NaF, using either a cell scraper or 5mm stainless steel beads in a TissueLyser (Qiagen, Hilden, Germany) as previously described[37,92]. Protein quantity was measured by using the micro-bicinchoninic (BCA) Assay Kit (ThermoFisher Scientific, Waltham, USA) according to the manufacturer's protocol. Samples were stored at -80C° for further analysis.

3.2.14 Western Blot.

Protein analysis was performed as previously described[94]. To separate proteins, 40 or 20 µg of protein lysate of each sample was loaded onto sodium dodecyl sulfate-polyacrylamide gel electrophoresis (SDS-PAGE) using commercially available 4–12% SurePAGETM, Bis-Tris gels (Genscript®, Piscataway, USA). Proteins were transferred to polyvinylidene fluoride (PVDF) membrane (Immobilon-P Transfer Membranes, MilliporeTM, Billerica, USA) with a transfer buffer containing 25 mM Tris, 192 mM Glycine, and 10% Methanol at 100 V for 60 min. The membranes were stained with NoStain Protein Labelling Reagent (ThermoFisher Scientific, Waltham, USA) to verify efficient transfer and measure total protein loading[95]. After blocking with 5% bovine serum albumin (BSA) or 5% skimmed milk for 1 h, membranes were probed overnight at 4°C with primary antibodies and 1 h at RT with corresponding secondary antibodies. Immunoreactive bands were detected by enhanced chemiluminescence with protein A-horseradish peroxidase and the Supersignal® West Pico Chemiluminescent Substrate (ThermoFisher Scientific, Waltham, USA). Equal protein loading was confirmed by either quantifying total protein loading or using GAPDH/Vinculin as housekeeping. Analysis was performed using ImageLab Software (Biorad, Hercules, USA). Details of primary and secondary antibodies used in this study are listed in Table 5.

Type	Antibody	Species	Catalogue number	Company	Dilution
Primary Antibody	COL1A1	mouse	Sc-293182	SantaCruz Biotechnology	1:200
	GAPDH	mouse	sc-47724	SantaCruz Biotechnology	1:2000
	MTCO1	mouse	Ab14705	Abcam	1:1000
	MTCO2	mouse	ab110258	Abcam	1:1000
	NR4A1	rabbit	3960	Cell Signaling Technology	1:750
	NR4A1 (phospho S351)	rabbit	PA5-105155	Invitrogen	1:500
	NRF2	Rabbit	16396-1-AP	Proteintech	1:500
	SOD1	Rabbit	2770	Cell Signaling Technology	1:1000
	SOD2	Rabbit	13141	Cell Signaling Technology	1:1000
	TGFB1	mouse	sc-130348	SantaCruz Biotechnology	1:100
	VARS2	rabbit	15776-1-AP	Proteintech	1:500
	Vinculin	Mouse	Ab129002	Abcam	1:10000
Secondary Antibody	Anti-rabbit IgG-HRP	Goat	7074	Cell Signaling Technology	1:2000
	Anti-mouse IgG-HRP	Goat	P0447	Dako	1:1000

Table 5: Antibodies used for Western Blot analysis

3.2.15 Protein secretion analysis.

Supernatants from HSCs cultured on liver scaffold samples were analysed for CXCL8, proCOL1A1, Latent TGFB1 (LAP) and 4-HNE protein secretion using Human IL-8 ELISA Kit (Abcam, Cambridge, UK), Human Pro-Collagen1alpha1 SimpleStep ELISA Kit (AbCam, Cambridge, UK), ELISA Pro: Human Latent TGF-β1 kit (MabTech, Cincinati, USA) and Universal 4-Hydroxynonenal ELISA Kit (Novus Biologicals, Englewood, USA), respectively.

3.2.16 ROS secretion analysis.

Supernatants from HSCs cultured on liver scaffold samples were tested for ROS content using OxiSelect™ In Vitro ROS/RNS Assay Kit (Green Fluorescence) (Cell Biolabs, San Diego, USA).

3.2.17 Complex IV and citrate synthase activity assay.

Complex IV and citrate synthase activities were determined spectrophotometrically in lysates of HSCs grown on plastic or on liver scaffolds. After trypsinization or collagenase extraction from liver scaffolds as previously described[92], cells were lysed in lysis buffer (10 mM Tris·HCl (pH 7.4), 320 mM sucrose, 1 mM EDTA, 1 mM phenylmethylsulfonyl, 1 µg/ml of leupeptin and 1 µg/ml of pepstatin A, 1% n-dodecyl-β-D-maltoside) and assays were performed as described[96].

3.2.18 Blue Native electrophoresis.

Detection of mitochondrial respiratory chain enzyme complexes was performed using Blue Native polyacrylamide gel electrophoresis (BN-PAGE). Briefly, 20-40 µg of samples were loaded onto non-commercial 4-12% acrylamide gels and were sufficiently resolved as previously described[97]. Membranes were subsequently processed as standard. Analysis was performed using ImageLab Software (Biorad, Hercules, USA) and Complex II (SDHA) was used as loading control. Details of primary and secondary antibodies used are listed in Table 6.

Type	Antibody	Species	Catalogue number	Company	Dilution
Primary Antibody	ATP5A	mouse	Ab14748	Abcam	1:1000
	MTCO1	mouse	Ab14705	Abcam	1:500
	NDUFB6	mouse	Ab110244	Abcam	1:500
	SDHA	mouse	Ab14715	Abcam	1:1000
	UQRCQ	mouse	Ab14745	Abcam	1:3000
Secondary Antibody	Anti-mouse IgG-HRP	Goat	P0447	Dako	1:1000

Table 6: Antibodies used for BN-PAGE

3.2.19 Extracellular Flux analysis.

Extracellular flux analysis was carried out on the Seahorse XFp platform (Agilent Technologies, Santa Clara, USA) as recommended by the supplier. HSCs were plated in wells of an XFp cell culture microplate and cultured for one day. To analyse oxidative phosphorylation function, the medium in the wells was replaced with XF Base medium (Agilent Technologies, Santa Clara, USA) pH 7.4 (NaOH), containing 10 mM D-(+)-glucose, 1 mM sodium pyruvate, 2 mM l-glutamine. After 1 hour of humidified incubation at 37 °C, oxidative phosphorylation was evaluated on the XFp platform with the Seahorse XFp Mito Stress Test Kit (Agilent Technologies, Santa Clara, USA), with subsequent injections of oligomycin A (final concentration: 1 µM), carbonyl cyanide 4-(trifluoromethoxy)phenylhydrazone (FCCP) (0.5 µM) and rotenone (1uM)-antimycin A (1 uM)-Hoechst 33342 (1µM). On each XFp cell culture microplate, triplicates of WT-PNPLA3 HSCs were compared with triplicates of I148M-PNPLA3 HSCs. To determine the number of cells per well, the nuclear Hoechst 33342 fluorescence was evaluated using a Cytation 1 Cell Imaging multimode reader (Agilent, Santa Clara, USA). Data were analysed with Wave Desktop 2.6 software and a Microsoft Excel Macro provided by Agilent Technologies. Results were expressed per number of cells.

3.2.20 Data analysis and statistics.

The statistical analysis was performed using GraphPad Prism 9.0c software for Windows (Graph Pad CA, USA). Values are expressed as mean and standard deviation (SD). Statistical significance was analysed using t Student’s test or one/two-way or three-way ANOVA with Tukey’s multiple comparison test.

3.3 Results

3.3.1 Transcriptomic analysis of WT-PNPLA3 and I148M-PNPLA3 HSCs and human liver biopsies.

To investigate the impact of the PNPLA3 I148M variant on the fibrogenic phenotype of HSCs, primary human HSCs were isolated, genotyped and classified as PNPLA3 rs738409 CC (wild-type – from now on referred as PNPLA3-WT) or PNPLA3 rs738409 CG (heterozygous mutant – from now on referred as PNPLA3-I148M). Primary HSCs were cultured on plastic, and next generation sequencing (NGS) of bulk transcriptome was used to study the biological processes modulated by the PNPLA3 variant. Ingenuity Pathway Analysis (IPA) highlighted a wide number of significantly deregulated “Canonical Pathways”, ranging from increased fibrogenesis, inflammation, metabolism, and proliferation, which were independently confirmed with specific markers in an additional experiment where HSCs were cultured on plastic (Figure 6).

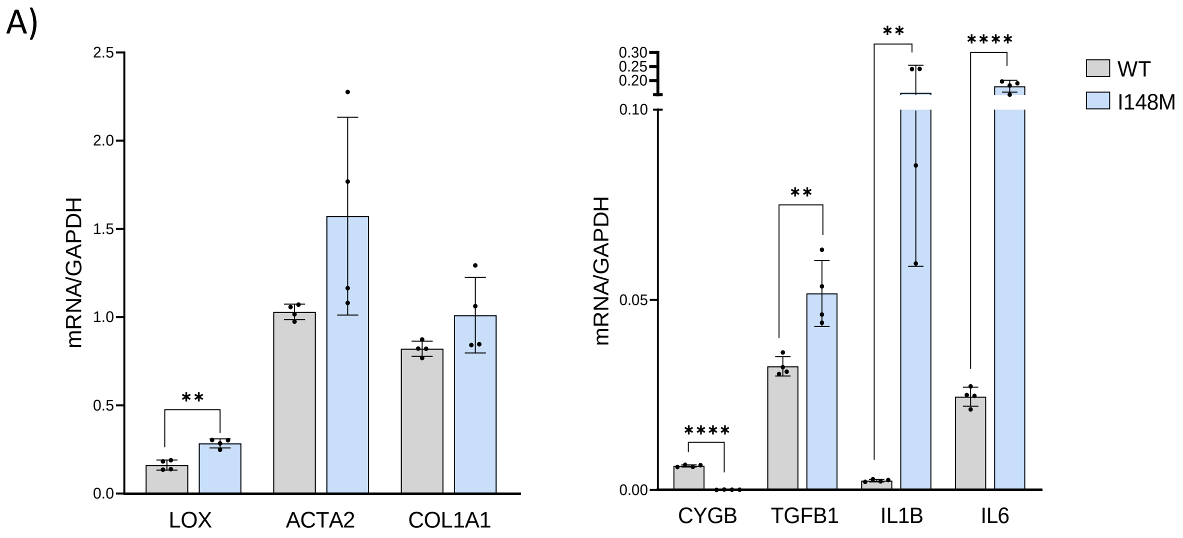

B)

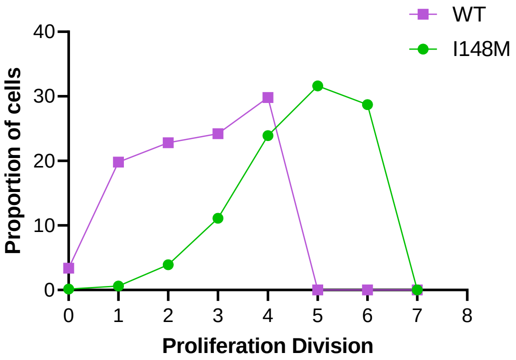

Figure 6: Characterization of HSCs genotyped WT or I148M for the PNPLA3 variant and cultured on plastic. *(A) Gene expression analysis of LOX, ACTA2, COL1A1, CYGB, TGFB1, IL1B and IL6 in HSC genotyped WT or I148M for PNPLA3 variant and cultured on plastic for 3 days. (B) Representative dot-plot showing proliferation of HSCs WT or I148M for PNPLA3 variant cultured on plastic and tracked with Cytopainter for 7 days; each dot represents the number of cells in each proliferation division (****/***/**/*p<0.001/0.005/0.01/0.05, N=1 donor per genotype, N=4 biological replicates per condition; data analysed with Student t-test).*

Most pathways modulated by the PNPLA3 variant were related to mitochondria metabolism and oxidative stress (increased “Oxidative Phosphorylation” and “NRF2-mediated oxidative stress response”) or to glucose and lipid metabolism (increased “Apeline adipocyte signalling pathway” and decreased “PPARα/RXRα activation”) along with ECM remodelling (increased “ILK signalling”) (Figure 7A). Increased fibrogenesis, synthesis of lipids and reduction of hydrogen peroxide in PNPLA3-I148M HSCs was also identified by Biofunctions analysis (Figure 7B).

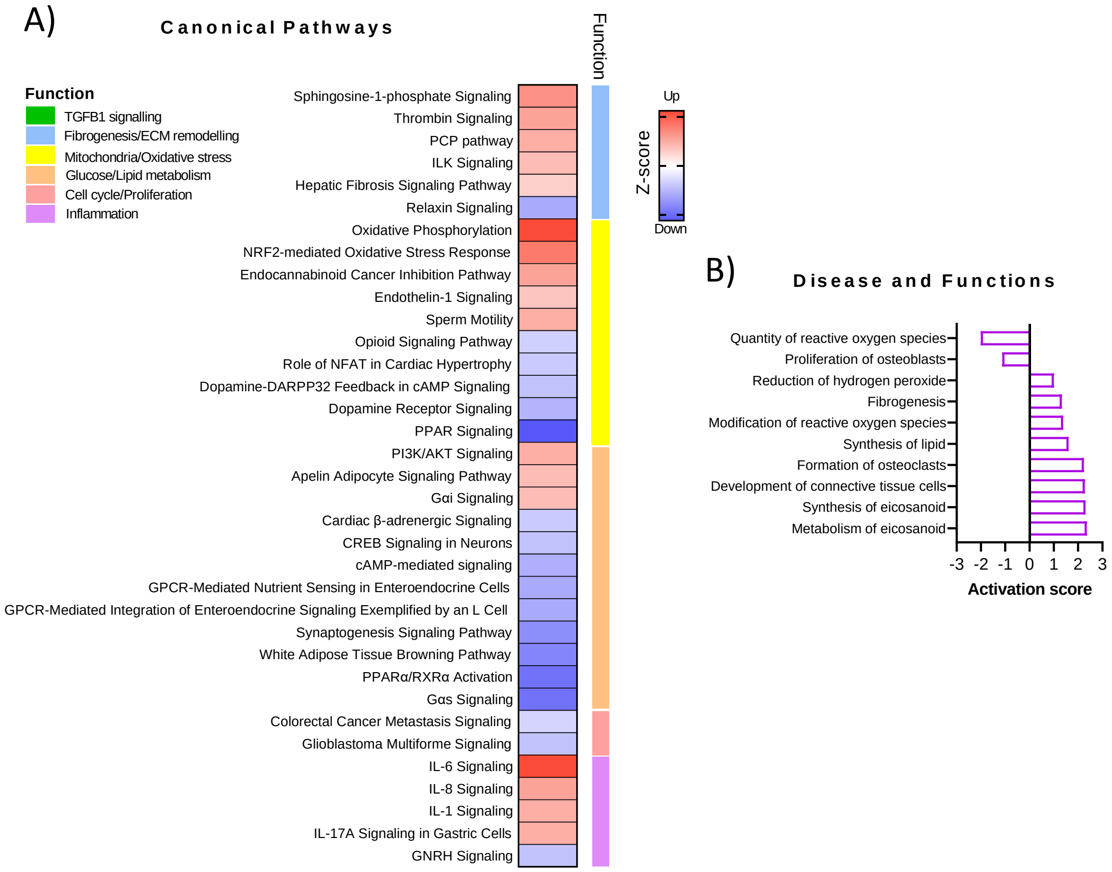

Figure 7: Gene expression profiled by NGS and analysed by IPA of in vitro-cultured primary human HSCs genotyped for WT-I148M PNPLA3 mutations: Canonical Pathways and Biofunctions. *(A-B) Significantly enriched (A) canonical pathways predicted as up- or down-regulated (-0.5 ≤ Z-score ≥ 0.5, p<0.05) or (B) significantly enriched biofunctions (-3 ≤ Z-score ≥ 3, p<0.05).*

Analysis of the activation status of the network of modulators which might drive the pathways dysregulation (upstream regulators analysis-URA) predicted a strong activation of inflammatory and proliferative genes, but also many activators linked to oxidative stress, lipid metabolism and an extended number of intracellular mediators of TGFB1 signalling (Figure 8A). In addition, transcriptomic analysis highlighted a group of significantly up-and down regulated target genes (Figure 8B).

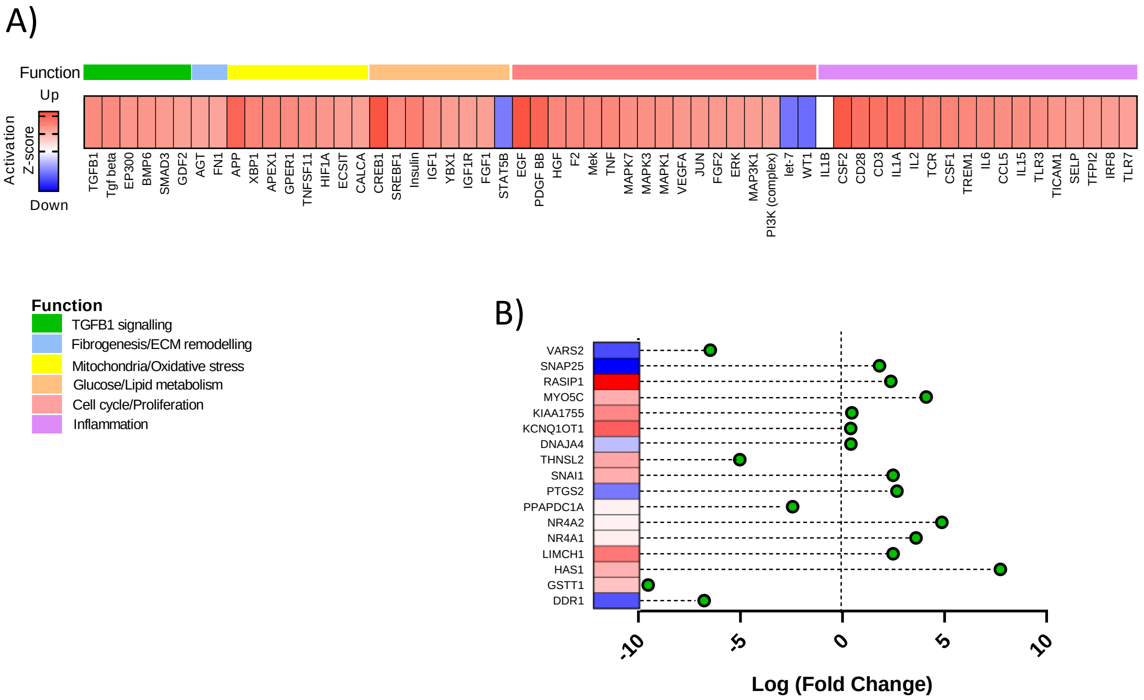

Figure 8: Gene expression profiled by NGS and analysed by IPA of in vitro-cultured primary human HSCs genotyped for WT-I148M PNPLA3 mutations: Upstream Regulators and target genes. *(A) Significantly enriched upstream regulators predicted as activated (red) or inhibited (blue) (-2.25 ≤ Z-score ≥ 2.25, p<0.05); (B) Main up- or downregulated target genes identified by NGS, p<0.05.*

Before proceeding to target validation, a second round of analysis was performed to select pathways and genes modulated by the PNPLA3 variant in HSCs and potentially relevant for NAFLD progression. This was achieved by combining transcriptomic data of primary HSCs isolated from different donors (In vitro) with transcriptomic data obtained from patients' biopsies (Human) where the PNPLA3 variant had previously been identified as major driver of NAFLD disease severity and gene expression variability[84]. Comparison highlighted a large pool of significantly modulated genes shared between the two datasets (Figure 9).

Figure 9: Comparative IPA analysis of in vitro-cultured primary human HSCs and human biopsies of patients stratified according to carriage of the I148M*. Comparison of transcriptomic data (NGS), showing shared number of significantly deregulated genes (p<0.05).*

Selection of shared pathways and biofunctions significantly enriched and modulated in the same direction in both the datasets confirmed that the presence of the PNPLA3 variant is associated to the presence of a large set of pathways related to mitochondria/oxidative stress (increased "NRF2-mediated oxidative stress response"), glucose/lipid metabolism (decreased "Glucose metabolism disorder") and ECM signalling (increased "Hepatic Fibrosis", "ILK Signalling") (Figure 10A and 10B). URA analysis showed a similar trend to the *in vitro* analysis, with a large set of activated modulators related to ECM signalling and TGFB1 having one of the highest activation Z-scores (Figure 10C). The analysis predicted TGFB1 to be a main upstream regulator of more than half of the deregulated canonical pathways and most of the target genes identified by transcriptomics (Figure 10A and 10D, pathways/genes marked by red asterisk). Overall, these data suggest an effect of the PNPLA3 I148M variant on the fibrogenic phenotype of HSCs with an involvement of mitochondria/lipid metabolism and oxidative stress, with TGFB1 playing a key role.

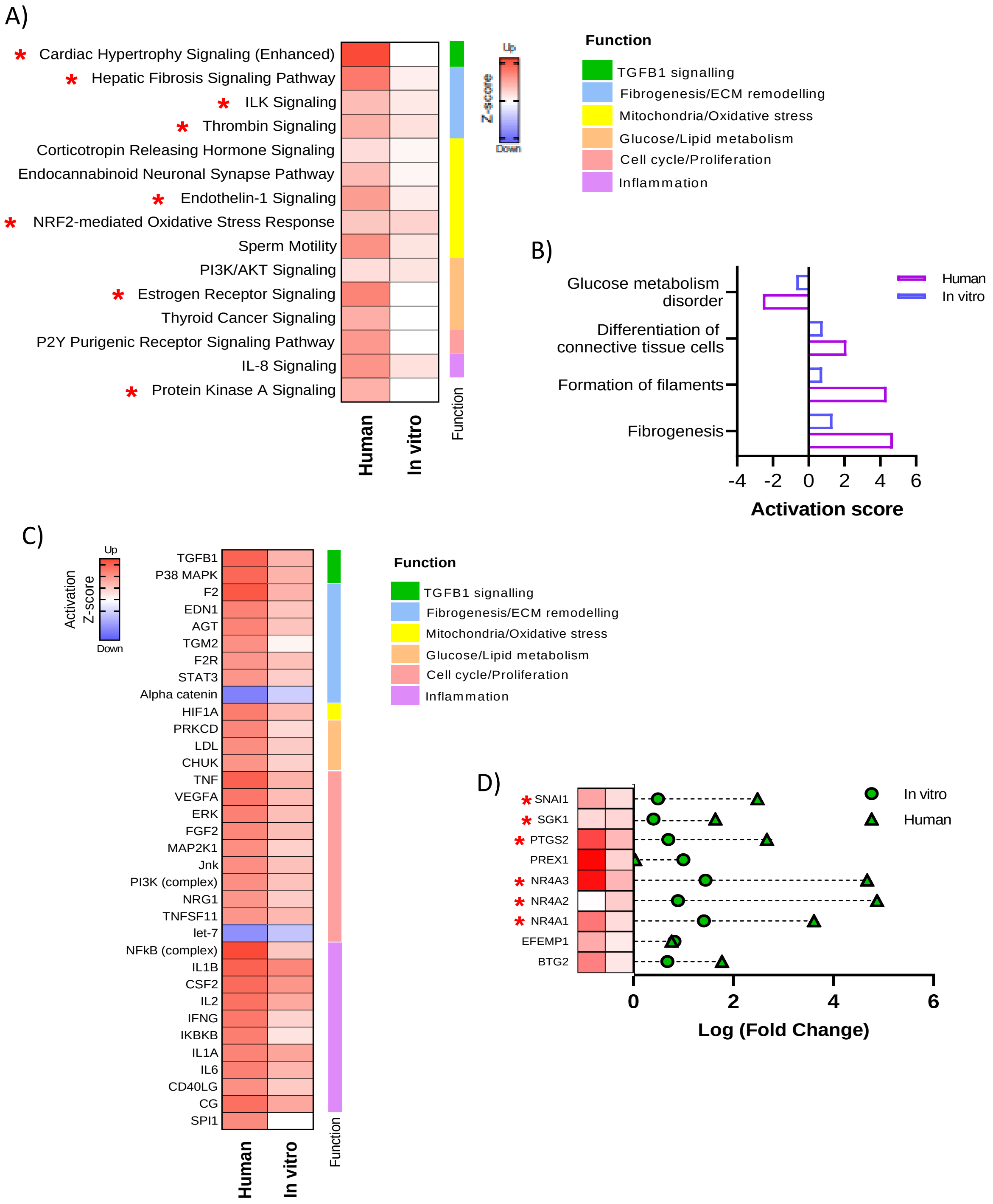

Figure 10: Gene expression profiled by NGS and analysed by IPA of in vitro-cultured primary human HSCs and human biopsies genotyped for WT-I148M PNPLA3 mutations. *(A-C) Comparative analysis of shared (A) significant canonical pathways. (-1 ≤ Z-score ≥ 1 for at least one group and going in the same direction for other groups, p ≤ 0.05, red asterisk indicates regulation by TGFB1) or (B) Biofunctions. (-4 ≤ Z-score ≥ 4 for at least one group and going in the same direction for other groups, p ≤ 0.05) or (C) predicted upstream regulators (-4 ≤ Z-score ≥ 4 for at least one group and going in the same direction for other groups, p ≤ 0.05). (D) Major up-downregulated target genes identified by NGS, p<0.05. Red asterisk indicates regulation by TGFB1.*

Preliminary gene expression investigation (Figure 12) and literature study prompted us to focus on NR4A1, an antifibrotic target of TGFB1, which can also be modulated by the antioxidant related transcription factors JUN and FOS (Figure 11).

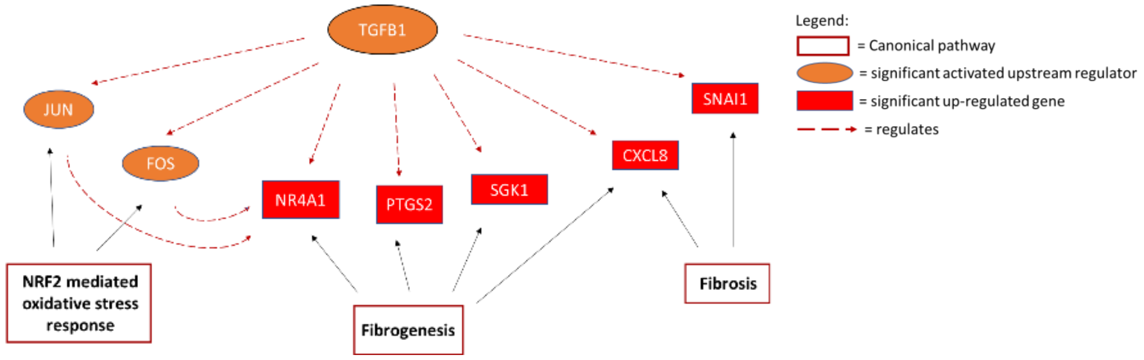

Figure 11: Gene expression profiled by NGS and analysed by IPA of in vitro-cultured primary human HSCs and human biopsies genotyped for WT-I148M PNPLA3 mutations: schematic. *Schematic representation of the upstream regulator, canonical pathways and target genes highlighted by IPA analysis and selected for further investigation.*

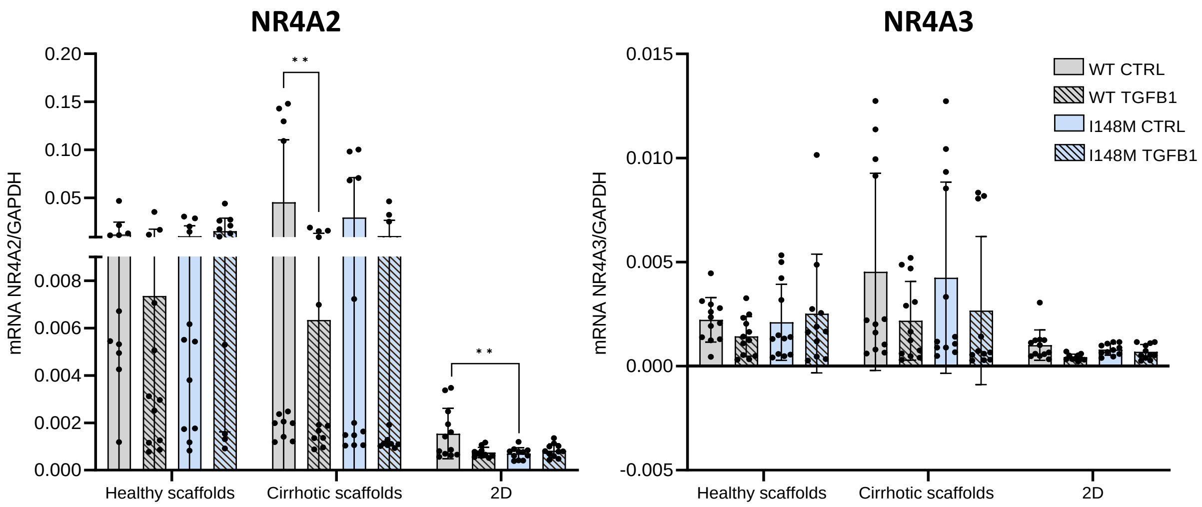

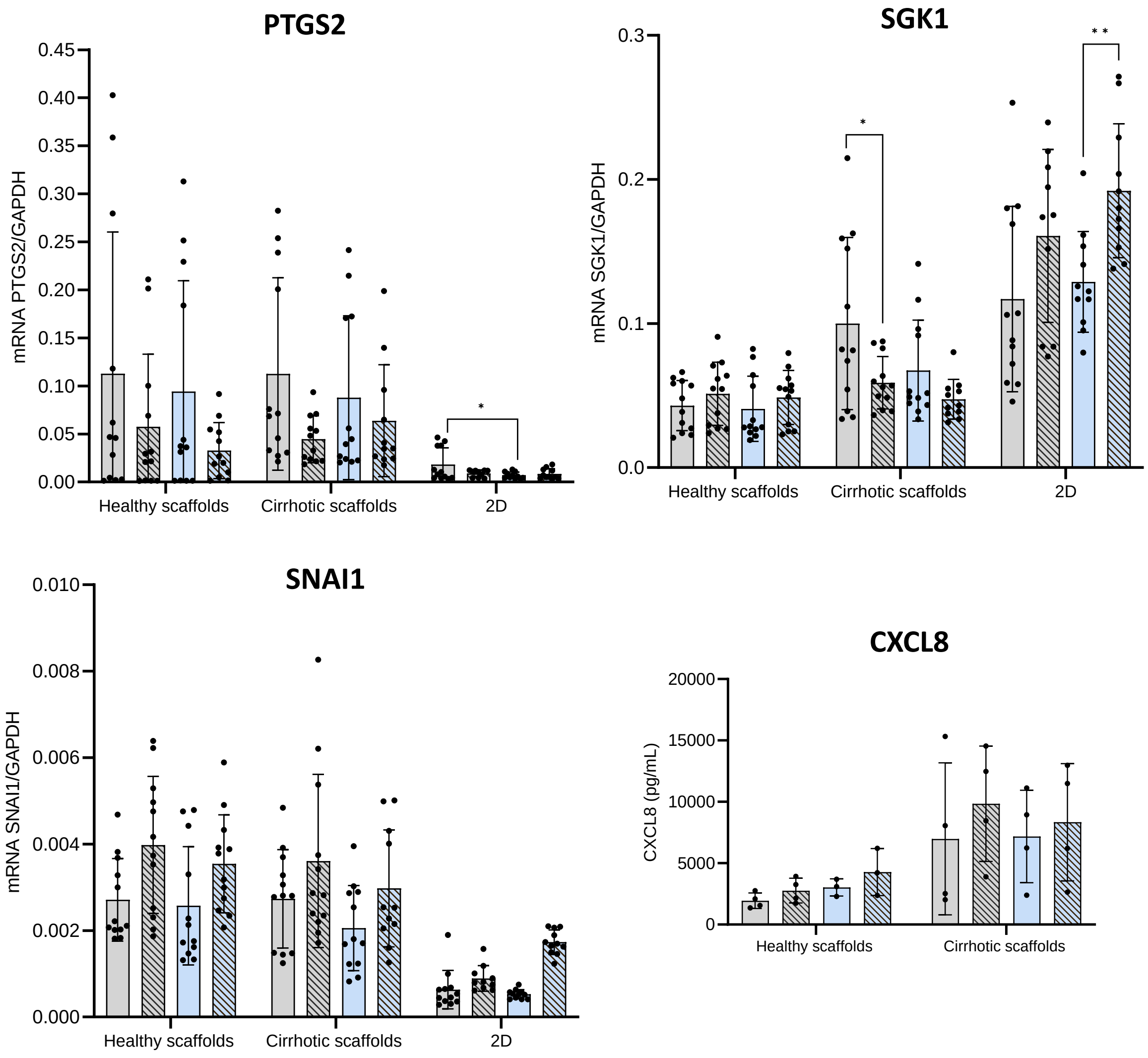

Figure 12: Validation of target genes highlighted by comparative NGS analysis of in vitro-cultured primary human HSCs and human biopsies genotyped for WT/I148M-PNPLA3 mutations. *(A) Gene expression analysis of NR4A2, NR4A3, PTGS2, SGK1, and SNAI1 in HSC genotyped WT or I148M for PNPLA3 variant and cultured in healthy or cirrhotic scaffolds for 14 days with or without TGFB1 (5ng/mL). (B) Protein secretion of CXCL8 measured in HSC genotyped WT or I148M for PNPLA3 variant and cultured in healthy or cirrhotic scaffolds for 14 days with or without TGFB1 (5ng/mL) (**/*p<0.01/0.05, Gene expression: N=3 donors per genotype, N=4 biological replicates per condition; Protein secretion: N=1 donor per genotype, N=4 biological replicates per condition; data analysed via three-way ANOVA and Tukey's multiple comparison test).*

3.3.2 The 3D HSCs model recapitulates PNPLA3 I148M-induced modulation of intracellular pathways observed in human livers and 2D models.

Findings from transcriptomic data were validated using an established extracellular matrix scaffolds 3D model[36,37]. The healthy and cirrhotic liver microenvironment was recapitulated by using acellular scaffolds obtained from healthy and cirrhotic human livers which were repopulated with patient-isolated PNPLA3-WT or PNPLA3-I148M HSCs and challenged with chronic TGFB1 treatment. Representative histology showing distribution of HSCs in the liver scaffolds is presented in Figure 13.

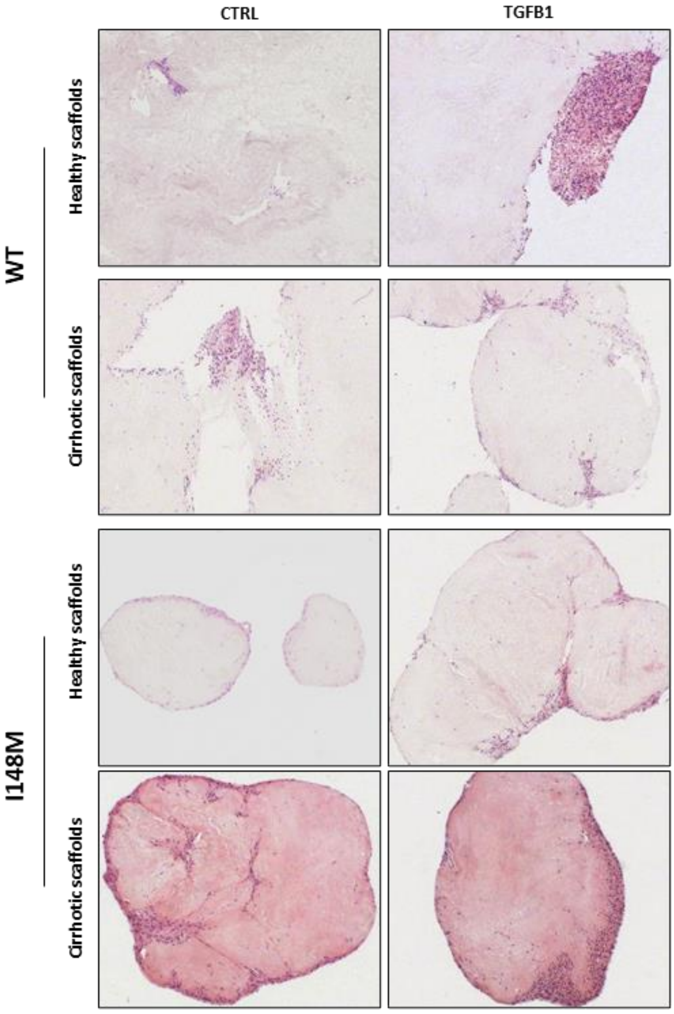

Figure 13: Characterization of the 3D model of HSCs genotyped WT or I148M for the PNPLA3 variant and cultured on healthy or cirrhotic human liver decellularized scaffolds: H&E. *H&E staining of HSCs genotyped WT or I148M for the PNPLA3 variant and cultured on healthy or cirrhotic human liver decellularized scaffolds for 14 days (10x magnification).*

Gene expression analysis on PNPLA3-WT or PNPLA3-I148M HSCs cultured on healthy and cirrhotic 3D scaffolds was performed by using Nanostring™ Technologies' nCounter® Human Fibrosis 700 genes panel (Figure 14). Gene set analysis (GSA) on these samples allowed to highlight pathways inducing differential expression driven either by the genotype (WT vs PNPLA3-I148M panel) or by the ECM (healthy vs cirrhotic ECM panel). Top 30 pathways driving differential expression in WT *versus* PNPLA3-I148M HSCs were related to “Collagen or ECM Biosynthesis and modification” (upregulation of thrombospondins and integrins with downregulation of MMPs), “TGFB1 signalling” (increasing F11R and SERPINE1), lipid metabolism (“PPAR Signalling”, “De novo lipogenesis” and “Fatty Acid metabolism”) and “Oxidative stress”. When comparing HSC cultures in 3D cirrhotic *versus* healthy ECM, top 30 impacted pathways showed differential expression of genes related to “Gluconeogenesis”, “Oxidative Stress”, “Hippo Pathways” but also TGFB1 and PDGF signalling (Figure 14).

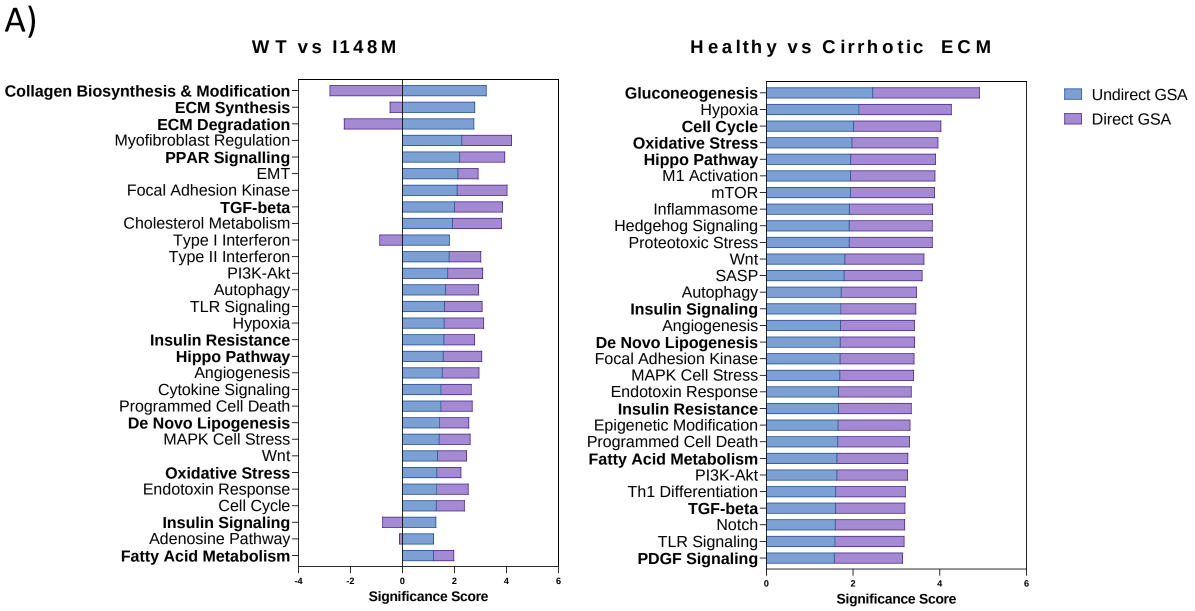

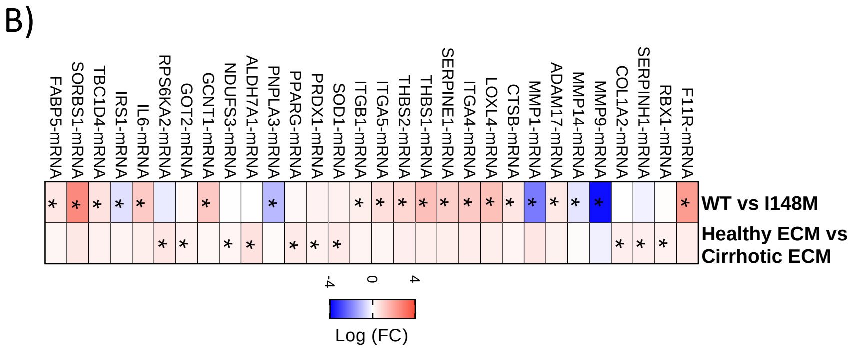

Figure 14: Characterization of the 3D model of PNPLA3 WT or I148M HSCs cultured on healthy or cirrhotic human liver decellularized scaffolds: Nanostring. *Nanostring nCounter RNA analysis for Human Fibrosis, showing list of up and down-regulated pathways in PNPLA3-I148M vs WT HSCs or HSCs cultured on cirrhotic ECM vs healthy ECM, analysed by Gene Set Analysis (GSA – Undirect or Direct) (A), and heatmap representing gene expression of single molecules in PNPLA3 I148M vs. WT HSCs or HSCs cultured on cirrhotic ECM vs healthy ECM (B). (*p<0.05, N=2 donors for each PNPLA3 genotype and N=4 for each ECM type).*

Next, TGFB1 signalling pathway was analysed: in PNPLA3-I148M HSCs and in cells cultured on the 3D cirrhotic ECM both TGFB1 protein expression (figure 15A-B) and latent TGFB1 secretion (Figure 15C) were significantly upregulated. Furthermore, in line with the TGFB1 upregulation, PNPLA3-I148M HSCs showed a pro-fibrotic behaviour which was demonstrated by the upregulation of SERPINE1, involved in ECM accumulation[98] (Figure 15D), COL1A1 and BMP1, the enzyme cleaving the C-terminal of pro-collagen 1a1 to mature COL1A1 (Figure 15E-H).

Overall, the pathways that appeared to be modulated in the 3D model were similar to those highlighted by the RNA sequencing data. In particular, TGFB1, highlighted by transcriptomic data as a key activated upstream regulator, showed increased signalling in PNPLA3-I148M HSCs *versus* PNPLA3-WT HSCs and in cirrhotic scaffolds compared to healthy scaffolds. Hence, the 3D model, which is able to recapitulate the changes identified by the RNA sequencing data, was chosen for further investigation.

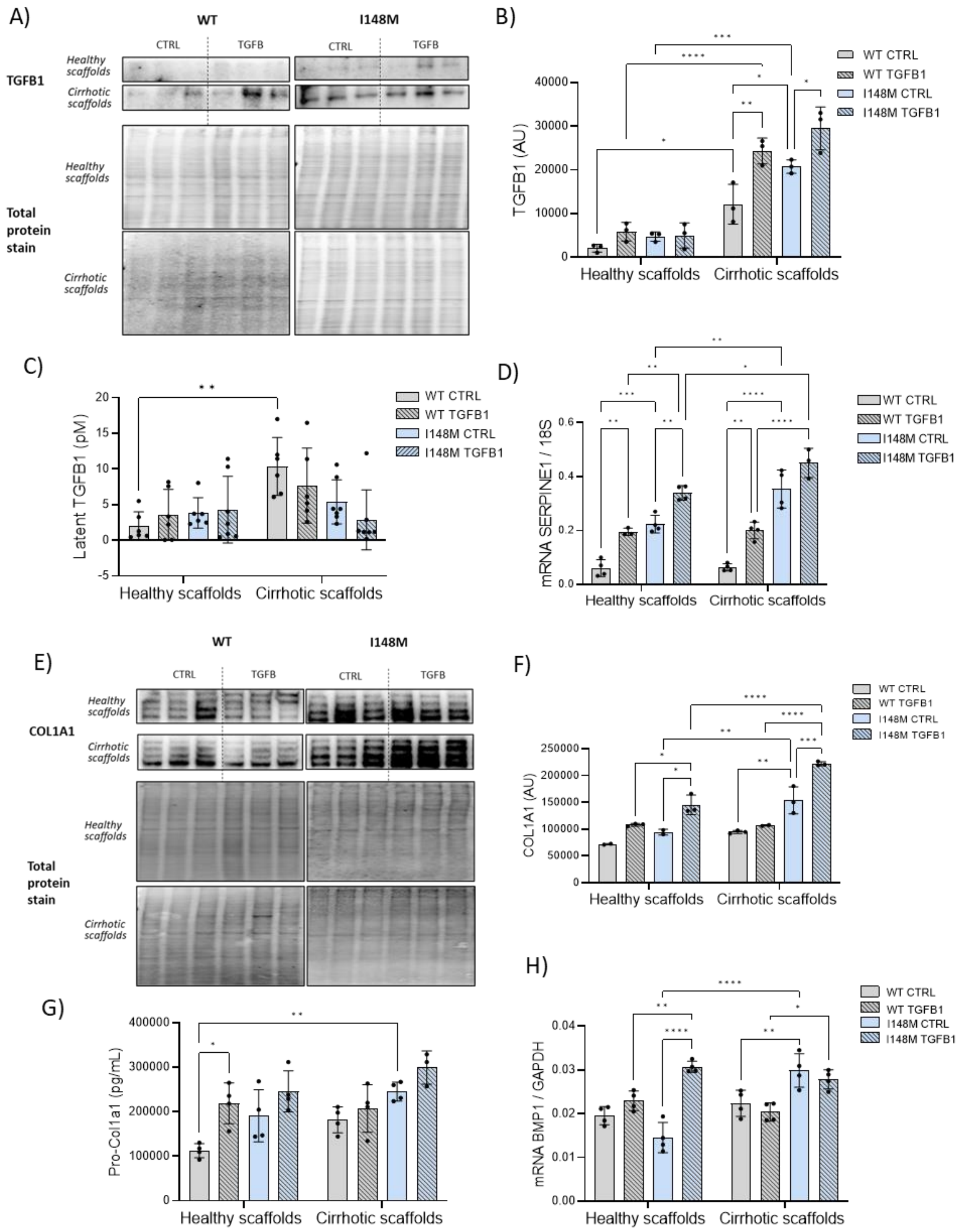

Figure 15: Characterization of the 3D model of PNPLA3 WT or I148M HSCs cultured on healthy or cirrhotic human liver decellularized scaffolds: TGFB1 and COL1A1. *Analysis of expression of genes and proteins in HSCs cultured on liver scaffolds for 14 days and treated with TGFB1 (5ng/mL). (A,B) TGFB1 protein expression. (C,D) Latent TGFB1 secretion and SERPINE1 gene expression. (E,F) COL1A1 protein expression. Blots from WT and I148M-PNPLA3 HSCs or healthy and cirrhotic scaffolds were processed in parallel. (G) Pro-COL1A1 protein secretion. (H) BMP1 gene expression; (****p<0.001/***p<0.005/**p<0.01/p<0.05; N= 1 donor per each genotype and N=3/4/6 biological replicates per each condition (protein expression/gene expression/protein secretion); data analysed via three-way ANOVA with Tukey's multiple comparison test).*

3.3.3 The PNPLA3 I48M variant causes mitochondrial dysfunction in HSCs

In vitro transcriptomic analysis highlighted a dysregulation of many mitochondrial metabolism related pathways, including the mitochondrial enzyme VARS2, which was downregulated in PNPLA3-I148M HSCs. This was confirmed on gene expression level in HSCs cultured in 2D with no changes on protein expression level (Figure 16A). When HSCs were cultured on 3D ECM scaffolds, the same trend of decreased VARS2 gene expression in PNPLA3-I148M HSCs was observed, with protein expression of VARS2 also significantly downregulated by the presence of the I148M variant and of the cirrhotic ECM (Figure 16B).

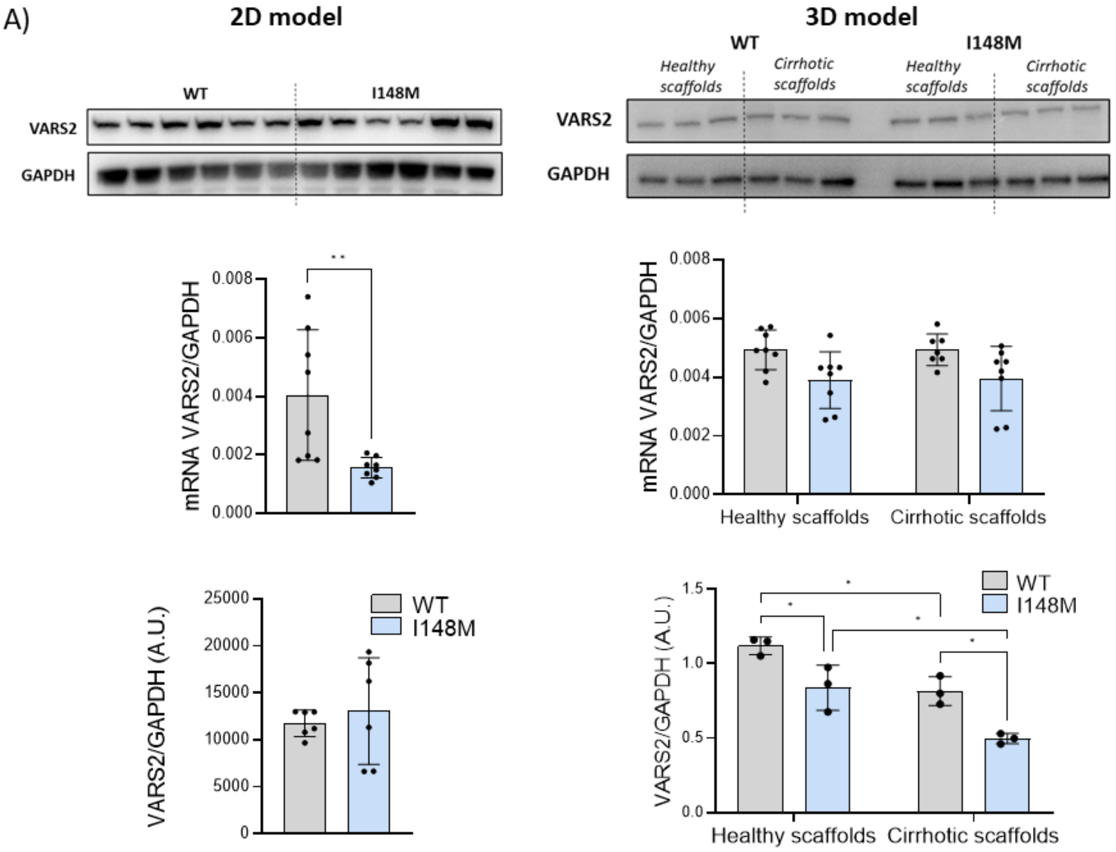

Figure 16: PNPLA3-I148M HSCs have impaired mitochondrial function compared to PNPLA3-WT HSCs: VARS2. *Analysis of expression of genes and proteins in PNPLA3-I148M vs WT HSCs. (A,B) VARS2 gene and protein expression in HSCs cultured (A) in 2D for 3 days or (B) in healthy or cirrhotic scaffolds for 14 days; (**/*p<0.01/0.05, Gene expression: N=2 donors per genotype, N=4 biological replicates per condition; Protein expression: N=3 (2D) or 1 (3D) donors per genotype, N=2/3 biological replicates per condition; data analysed via Student t-test or two-way ANOVA with Tukey's multiple comparison test).*

VARS2, the mitochondrial valyl tRNA synthetase, is a key enzyme in the synthesis of the mitochondrial DNA-encoded subunits of the respiratory chain enzyme complexes[99]. Hence, the abundance of two of the 13 mitochondrial DNA-encoded subunits and the five mitochondrial respiratory chain complexes (Complex I-V) was measured in WT and PNPLA3-I148M HSCs cultured in 2D or 3D scaffolds. The two mitochondrially encoded subunits of Complex IV, MTCO1 and MTCO2, were significantly downregulated in cells carrying the PNPLA3 I148M variant, with MTCO1 content being also lower in presence of the 3D cirrhotic ECM compared to healthy ECM, while no significant difference was observed in cells cultured in 2D (Figure 17A and 17B). Complex IV enzymatic activity was also lower in PNPLA3-I148M *versus* WT HSCs cultured in 2D or 3D healthy scaffolds, but not in cirrhotic scaffolds (Figure 17C).

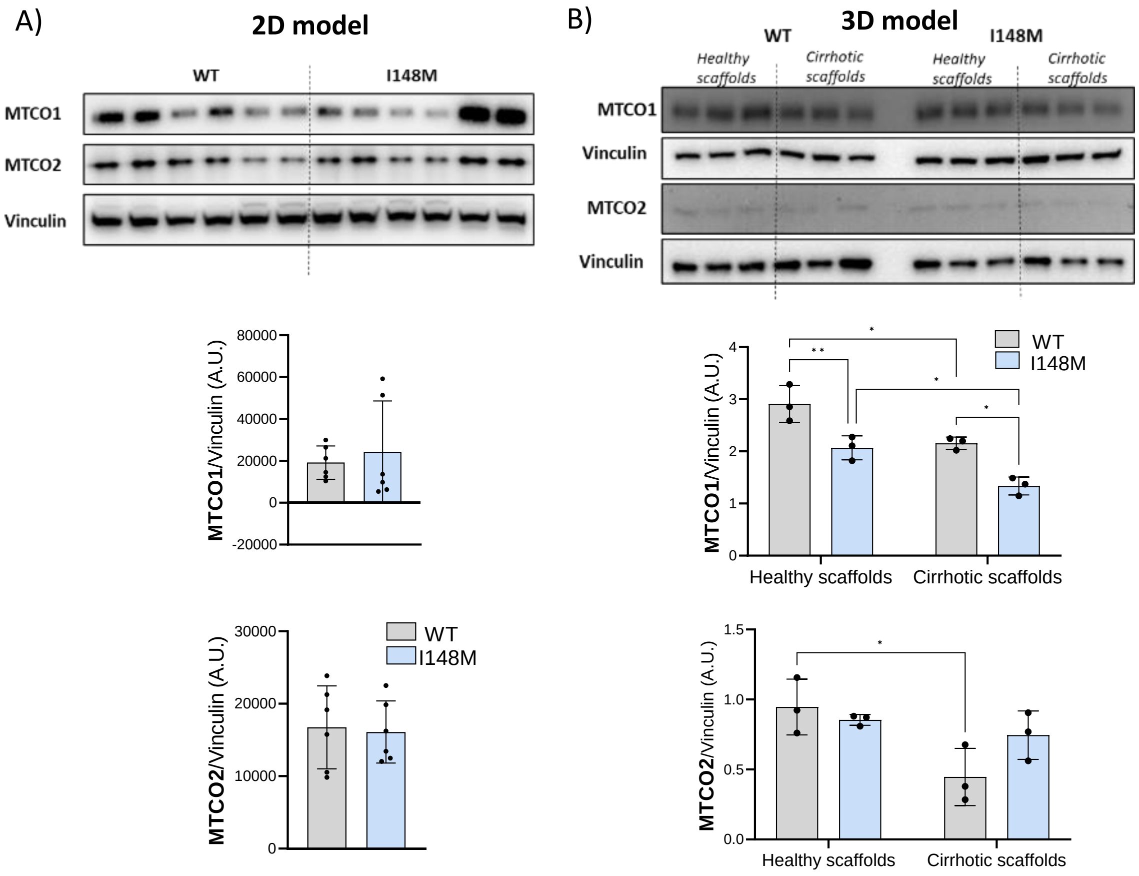

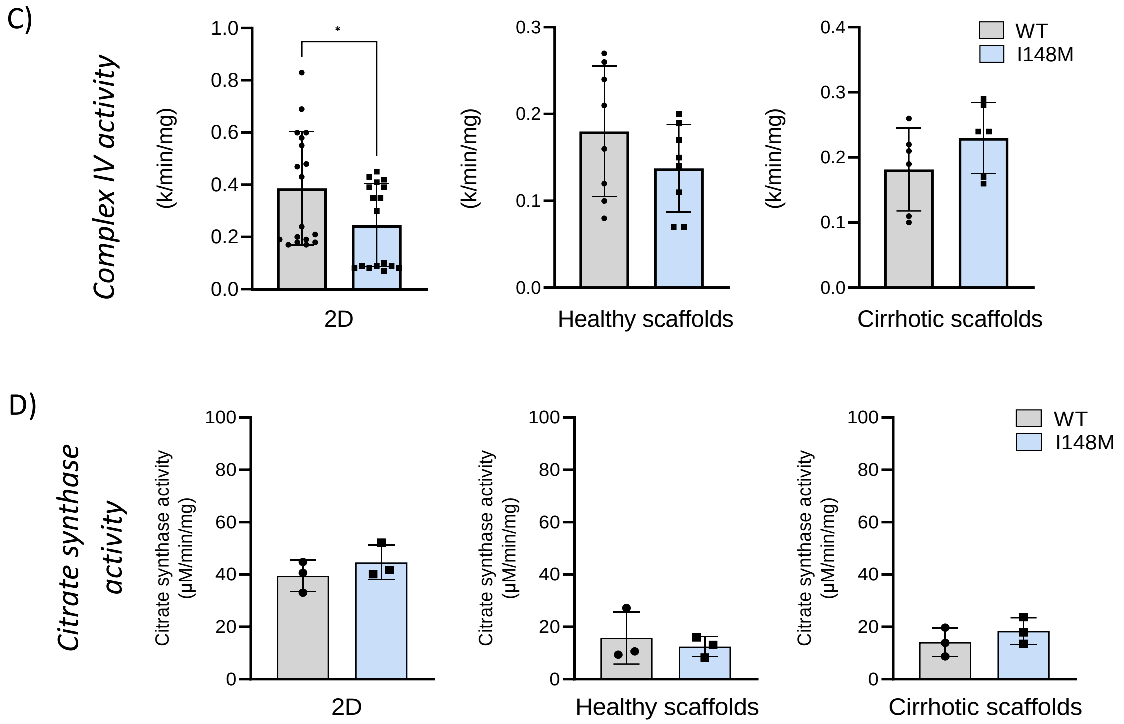

Figure 17: PNPLA3-I148M HSCs have impaired mitochondrial function compared to PNPLA3-WT HSCs: Complex IV. *Analysis of expression of genes and proteins in PNPLA3-I148M vs WT HSCs. (A,B) Protein expression of Complex IV mitochondrially encoded subunits MTCO1 and MTCO2 in HSCs cultured (A) in 2D for 3 days or (B) in healthy or cirrhotic scaffolds for 14 days; (C,D) Complex IV and Citrate synthase activity in HSCs cultured in 2D, healthy or cirrhotic scaffolds for 3 or 14 days; (**/*p<0.01/0.05, Protein expression: N=3 (2D) or 1 (3D) donors per genotype, Enzymatic activity: N=3 donors per genotype, N=3/6 biological replicates per condition; data analysed via Student t-test or two-way ANOVA with Tukey's multiple comparison test).*

In contrast, the expression of the other mitochondrial respiratory chain complexes, resolved on blue native gels, was not significantly affected by the PNPLA3 I148M variant or 3D cirrhotic ECM (Figure 18A and 18B). Furthermore, mitochondrial respiratory activity, which was quantified by measuring the Oxygen Consumption Rate (OCR), was decreased in PNPLA3-I148M *versus* WT HSCs. Specifically, while basal respiration was equal regardless of the presence of the PNPLA3 I148M mutation, maximal respiration observed in stress conditions (FCCP injection) was lower in PNPLA3-148M HSCs compared to WT (Figure 18C). These results suggest a PNPLA3 I148M driven mitochondrial dysfunction in HSCs, not due to a lower mitochondrial number, supported by unchanged activity of the citrate enzyme system (Figure 17D), but rather to a deficiency in Complex IV expression and activity.

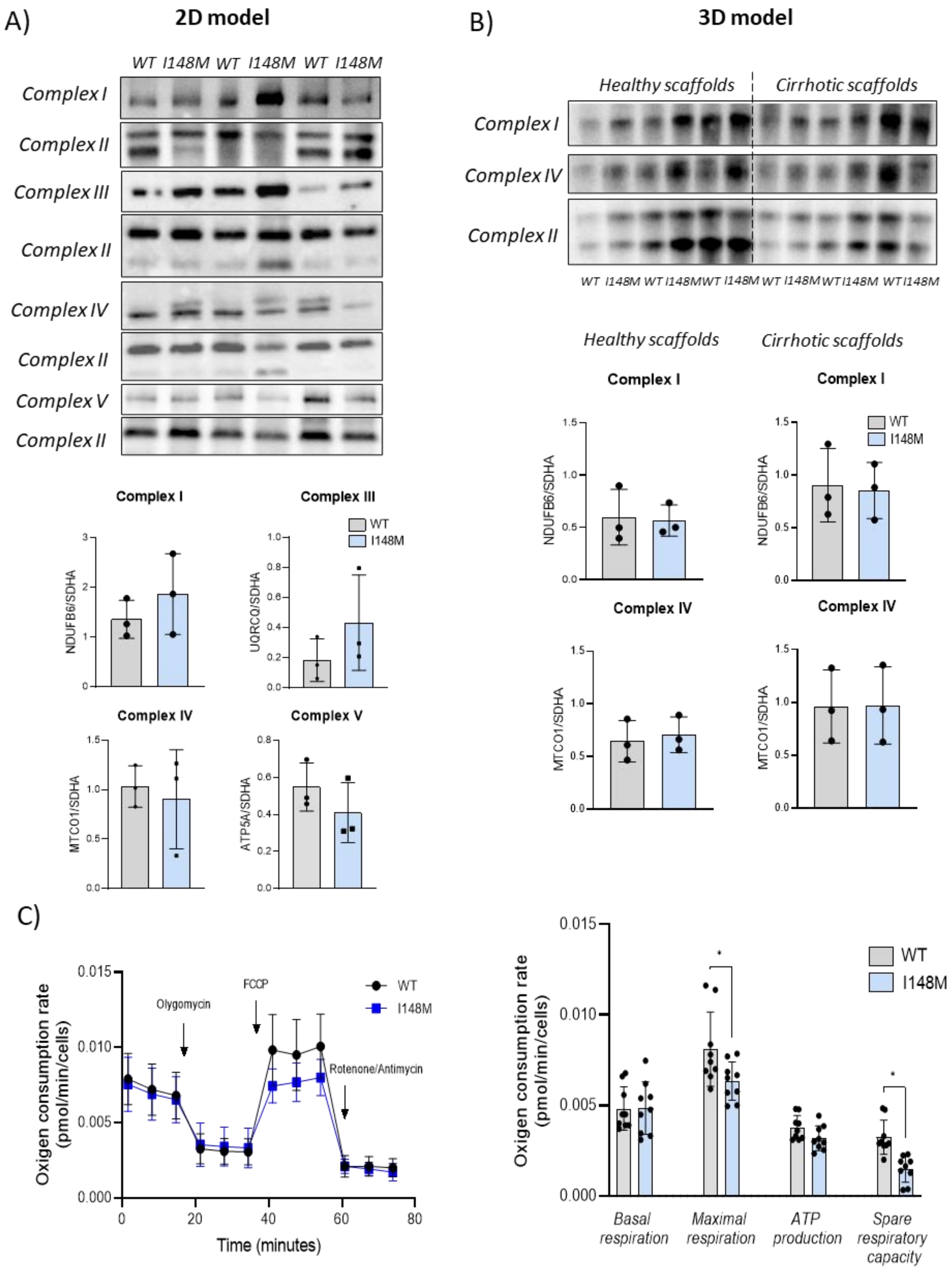

Figure 18: PNPLA3-I148M HSCs have impaired mitochondrial function compared to PNPLA3-WT HSCs: Mitochondrial respiratory chain complexes and OCR. *Analysis of expression of genes and proteins in PNPLA3-I148M vs WT HSCs. (A,B) Quantification of mitochondrial respiratory chain complexes using BN-PAGE in HSCs cultured (A) in 2D for 3 days or (B) on healthy or cirrhotic scaffolds for 14 days; SDHA (Complex II) was used as loading control; (C) Seahorse analysis showing the OCR (Oxygen Consumption Rate) in HSCs. (N=3 donors per genotype, N=1/3 biological replicate per condition for BN-PAGE/Seahorse; data analysed via Student t-test or two-way ANOVA with Tukey's multiple comparison test).*

3.3.4 Antioxidant response is reduced in PNPLA3-I148M HSCs.

In the presence of mitochondrial dysfunction, inefficient nutrient oxidation leads to a low ratio of ATP production/oxygen consumption. This can lead to an increased production of superoxide anions and consequent oxidative stress, which is known to play a key role in the progression of fatty liver disease[100]. Given the identification by IPA of several oxidative stress-related pathways which were dysregulated by the PNPLA3 I148M variant, and the mitochondrial dysfunction observed in the 3D model of HSCs, we further investigated the antioxidant capacity of the cells. Thus, HSCs grown in 3D model of healthy and cirrhotic ECM were exposed to TGFB1, known to be involved in oxidative stress processes[101] and identified as a key upstream regulator of gene expression variability in PNPLA3-I148M HSCs by NGS. Gene expression of CYGB, an oxygen transporter, was significantly decreased in HSCs carrying the PNPLA3 I148M variant or by TGFB1 treatment in healthy scaffolds. Gene expression of NRF2, a key antioxidant enzyme, followed a similar pattern, and its repressor, KEAP1, was downregulated following TGFB1 treatment in PNPLA3-I148M *versus* WT cells in presence of the cirrhotic ECM (Figure 19A). These results were further confirmed by protein expression analysis showing a decrease of NRF2 in presence of the PNPLA3 I148M variant and in the 3D cirrhotic ECM (Figure 19B).

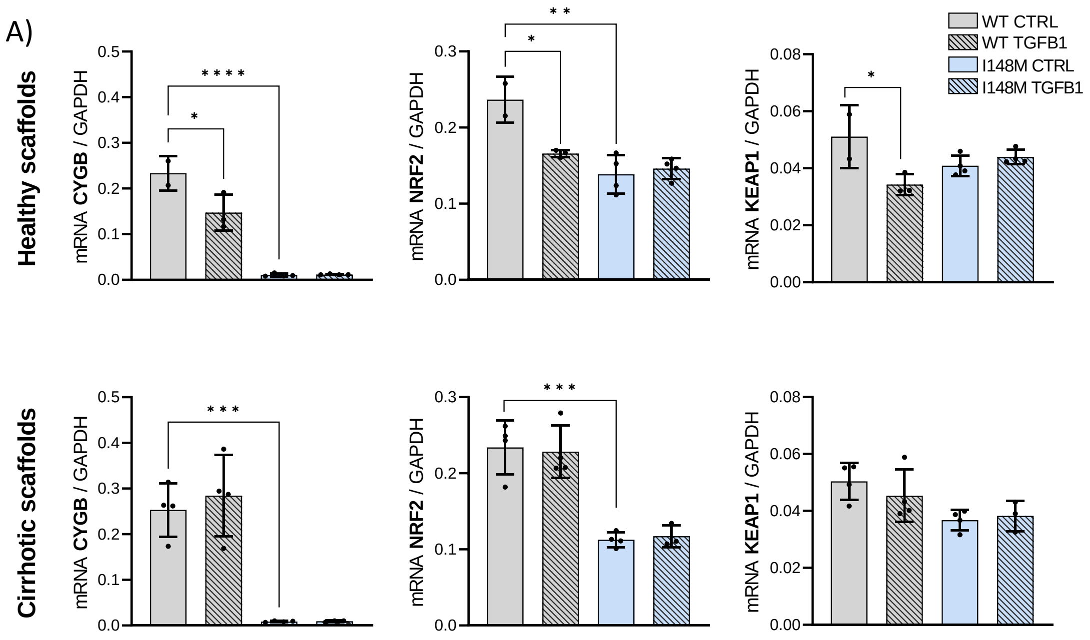

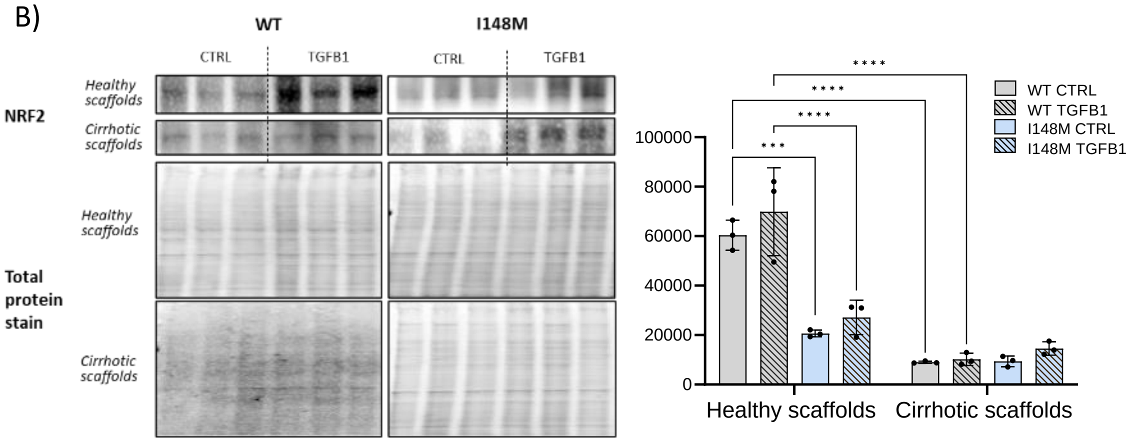

Figure 19: Characterization of antioxidant response of HSCs PNPLA3-I148M WT HSCs cultured in healthy or cirrhotic scaffolds: CYGB, NRF2 and KEAP1. *Analysis of expression of genes and proteins in PNPLA3-I148M vs WT HSCs cultured on healthy or cirrhotic scaffolds with or without TGFB1 (5ng/mL). (A) Gene expression analysis of CYGB, NRF2, KEAP1; (B) NRF2 protein expression. Blots from WT and I148M-PNPLA3 HSCs or healthy and cirrhotic scaffolds were processed in parallel. (****/***/**/*p<0.001/0.005/0.01/0.05, N= 1 donor per genotype, N= 3 or 4 biological replicates per condition (protein expression/gene expression); data analysed via two or three-way ANOVA with Tukey's multiple comparison test).*

Interestingly, the amount of SOD2, the mitochondrial-specific superoxide dismutase, was decreased in PNPLA3-I148M *versus* WT HSCs, whereas the same pattern was not observed for the cytoplasmic superoxide dismutase SOD1 (Figure 20A). In addition, measurement of ROS release showed a significant increase in the amount of lipid peroxidation products such as 4-Hydroxynonenal (4-HNE), driven by the presence of the PNPLA3 I148M variant and further increased by the 3D cirrhotic ECM. A similar pattern was not observed in the release of other endogenous ROS such as H_20_2, although this was increased by the TGFB1 treatment in cirrhotic scaffolds (Figure 20B). These data indicate an impaired antioxidant response in PNPLA3-I148M HSCs, which leads to an increase in ROS. Importantly, this effect is significantly enhanced in the presence of the cirrhotic ECM or after exposure to TGFB1 and supports the findings from transcriptomic data.

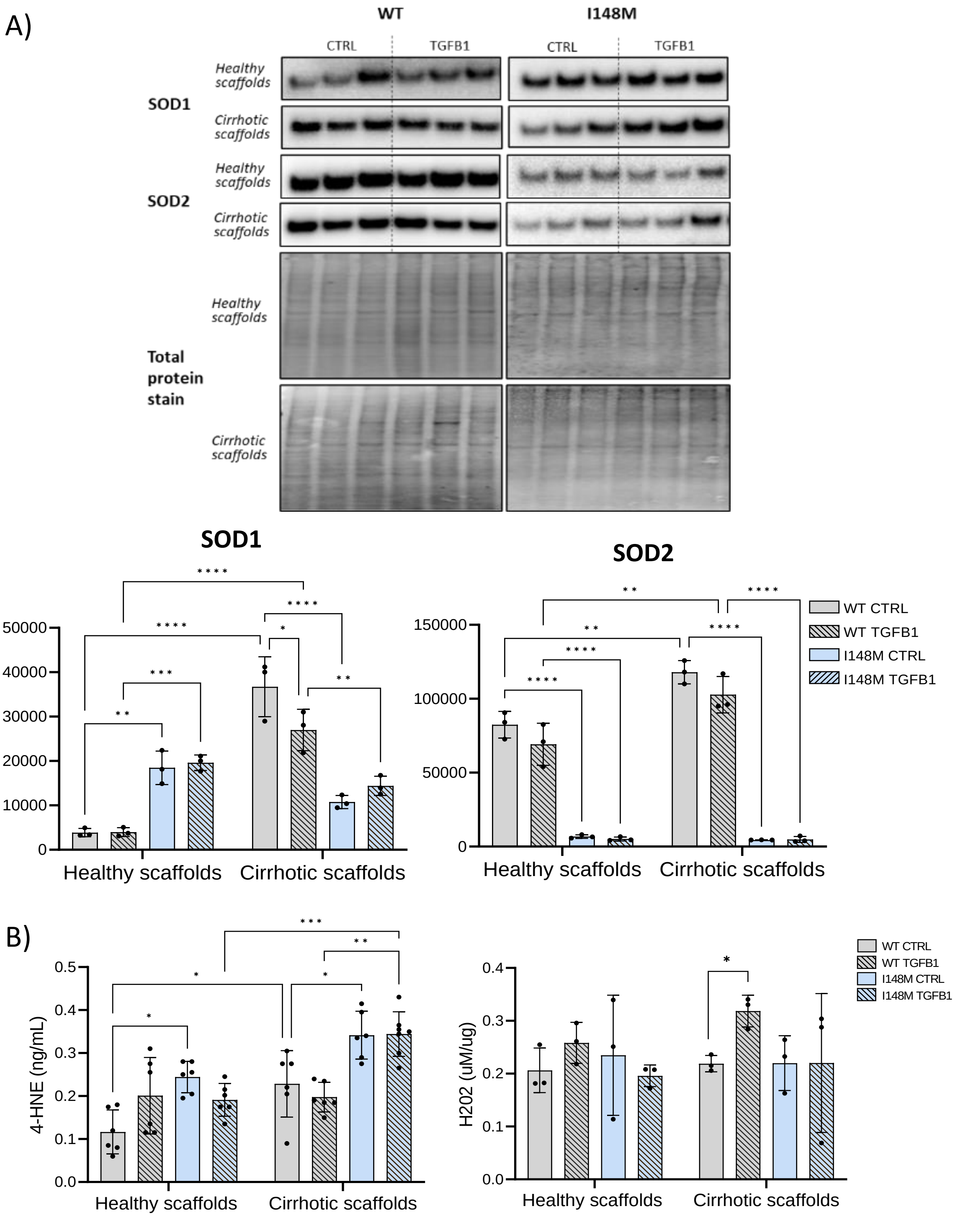

Figure 20: Characterization of antioxidant response of HSCs PNPLA3-I148M WT HSCs cultured in healthy or cirrhotic scaffolds: SOD1, SOD2 and ROS.** Analysis of expression of proteins in PNPLA3-I148M vs WT HSCs cultured on healthy or cirrhotic scaffolds with or without TGFB1 (5ng/mL). (A) SOD1 and SOD2 protein expression. Blots from WT and I148M-PNPLA3 HSCs or healthy and cirrhotic scaffolds were processed in parallel. (B) Quantification of secreted H_2O_2 and 4-HNE; (*/***/**/*p<0.001/0.005/0.01/0.05, N= 1 donor per genotype, N= 3/6 biological replicates per condition (western blot/ELISA); data analysed via three-way ANOVA with Tukey's multiple comparison test).*

3.3.5 Antifibrotic NR4A1 is downregulated in PNPLA3-I148M vs WT HSCs.

NR4A1, also known as Nur77, is a transcription factor of the Nuclear Receptors superfamily that governs multiple cell functions including metabolism[102,103], oxidative stress[104] and multiple aspects of wound-healing. It is also described as an antifibrotic gene modulated by TGFB1 i.e., upon NR4A1 phosphorylation, induced by chronic TGFB1 presence, NR4A1 protein translocate from the nucleus to the cytoplasm, becoming inactive and unable to counteract the pro-fibrogenic effect of TGFB1[105]. NR4A1 was highlighted as differentially modulated in presence of the PNPLA3 I148M variant by NGS. NR4A1 gene expression was decreased following chronic TGFB1 treatment only in HSCs grown in cirrhotic scaffolds (Figure 21A). In addition, the total amount of NR4A1 protein was strikingly lower in PNPLA3-I148M *versus* WT HSCs, whereas the phosphorylated fraction of NR4A1 was higher in PNPLA3-I148M *versus* WT HSCs and further increased by chronic treatment with TGFB1 when cells were cultured in the 3D cirrhotic scaffold (Figure 21B).

A)

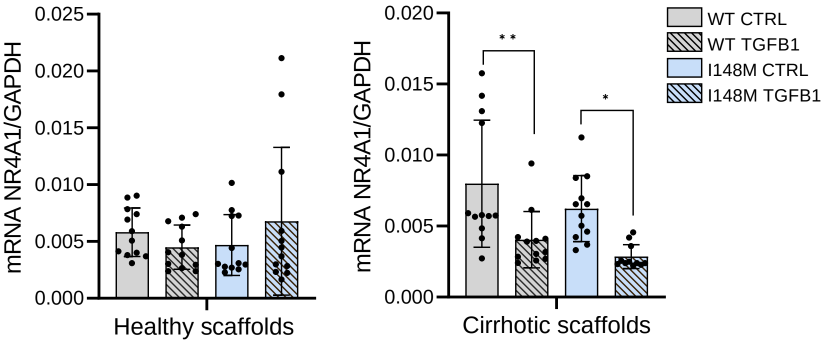

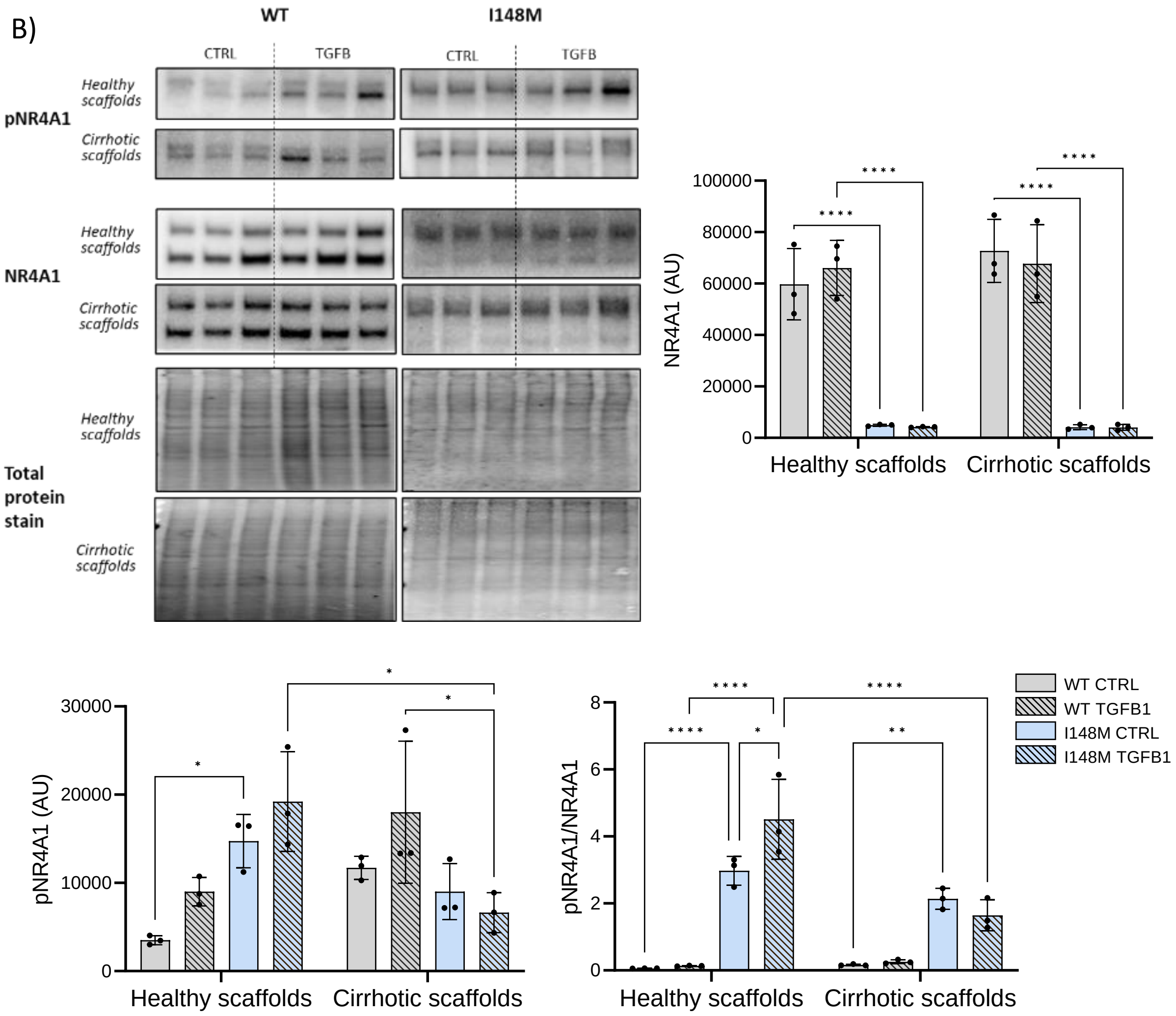

Figure 21: NR4A1 expression and TGFB1 regulation in WT-PNPLA3 or I148M-PNPLA3 genotyped HSCs: gene and protein expression. *Analysis of expression of genes and proteins in PNPLA3-I148M vs WT HSCs cultured on healthy or cirrhotic scaffolds with or without TGFB1 (5ng/mL). (A) Gene expression of NR4A1 (**/*p<0.01/0.05, N= 3 donors per genotype, N=4 biological replicates per condition; data analysed via two-way ANOVA with Tukey's multiple comparison test); (B) Protein expression of NR4A1, pNR4A1 and ratio of pNR4A1 to NR4A1. Blots from WT and I148M-PNPLA3 HSCs or healthy and cirrhotic scaffolds were processed in parallel. (****/***/**/*p<0.001/0.005/0.01/0.05, N= 1 donor per genotype, N=3 biological replicates per condition; data analysed via three-way ANOVA with Tukey's multiple comparison test).*

Importantly, inactivation of NR4A1 in PNPLA3-I148M HSCs was confirmed by the downregulation of gene expression of NR4A1 targets as analysed by Nanostring™ nCounter® for Human Fibrosis and shown in Table 7.

NR4A1 target	Log (FC)	P-value
EGR1	-1.21	2.50E-05
HMOX1	-2.95	0.00663
JUN	-0.978	0.0462

Table 7. NR4A1 expression and TGFB1 regulation in WT-PNPLA3 or I148M-PNPLA3 genotyped HSCs: NR4A1 activity. *Gene expression fold change of NR4A1 target genes in I148M-PNPAL3 HSCs vs WT-PNPLA3 HSCs cultured on ECM scaffolds (N=3 donors per genotype, N=2 biological replicates per condition) obtained from Nanostring™ analysis.*

Immunohistochemistry of NR4A1 and phospho-NR4A1 confirmed the localization of the active NR4A1 mainly in the cellular nuclei and of the inactive phosphorylated NR4A1 mainly in the cytoplasm in both WT (Figure 22A) and PNPLA3-148M (Figure 22B) HSCs.

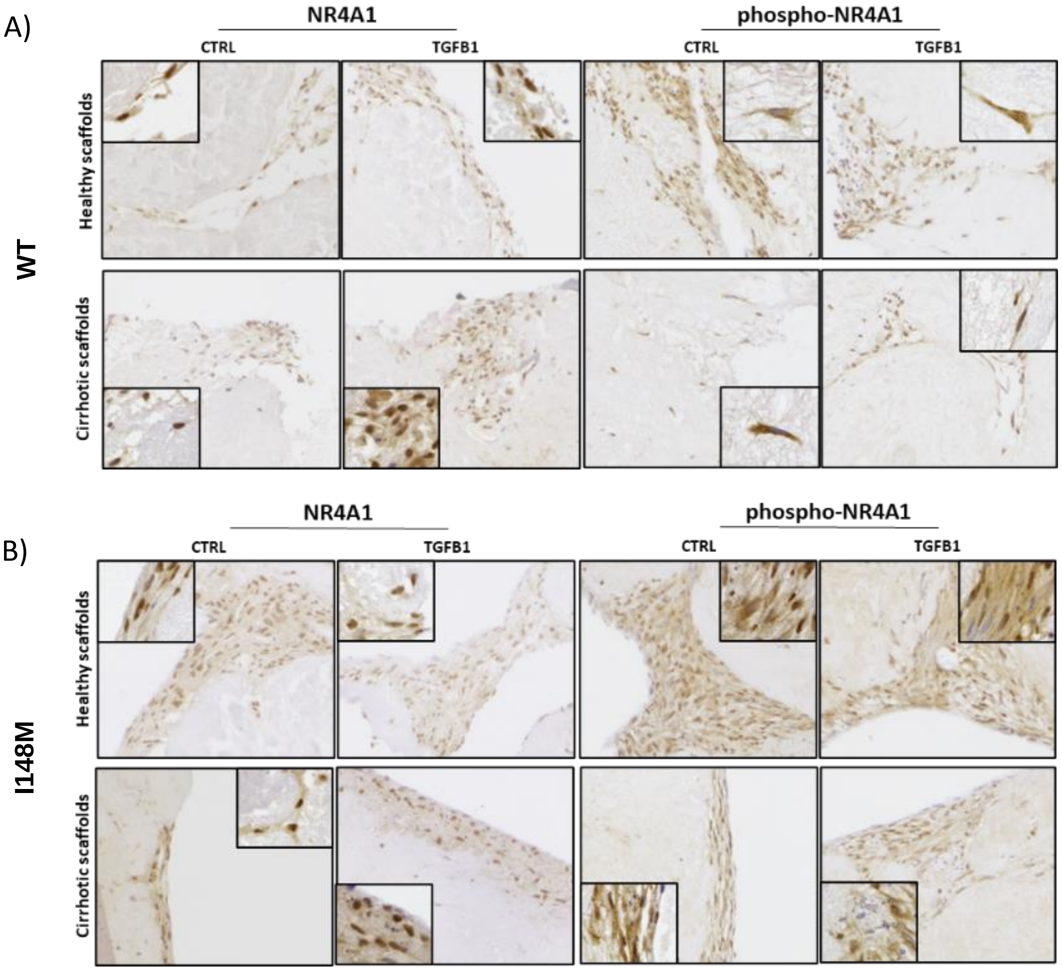

Figure 22: ***NR4A1 expression and TGFB1 regulation in WT-PNPLA3 or I148M-PNPLA3 genotyped HSCs: IHC.*** *Analysis of expression of genes and proteins in PNPLA3-I148M vs WT HSCs cultured on healthy or cirrhotic scaffolds with or without TGFB1 (5ng/mL). (A,B) Immunohistochemical staining of NR4A1 and phospho-NR4A1 in (A) WT HSCs or (B) I148M-PNPLA3 HSCs. (brown – NR4A1/phosphoNR4A1, blue/purple – chromatin).*

3.3.6 NR4A1 agonist Cytosporone-B increases NR4A1 only in HSCs cultured in 3D healthy scaffolds.

To further explore whether an increase in NR4A1 affects the mitochondrial/antioxidant/profibrogenic features of HSCs, and whether this process can be modulated by PNPLA3 genotype, HSCs exposed to TGFB1 were supplemented with the NR4A1 natural agonist Cytosporone-B (Csn-B)[106]. Dosage of Csn-B was determined by performing a dose-response curve of increasing Csn-B concentrations which were tested on both WT and PNPLA3-I148M HSCs cultured in 2D and in the 3D healthy scaffold. Csn-B was toxic for cells cultured in 2D only at the highest concentration (20µM), while in the 3D model, toxicity of Csn-B was detectable at 10µM (Figure 23).

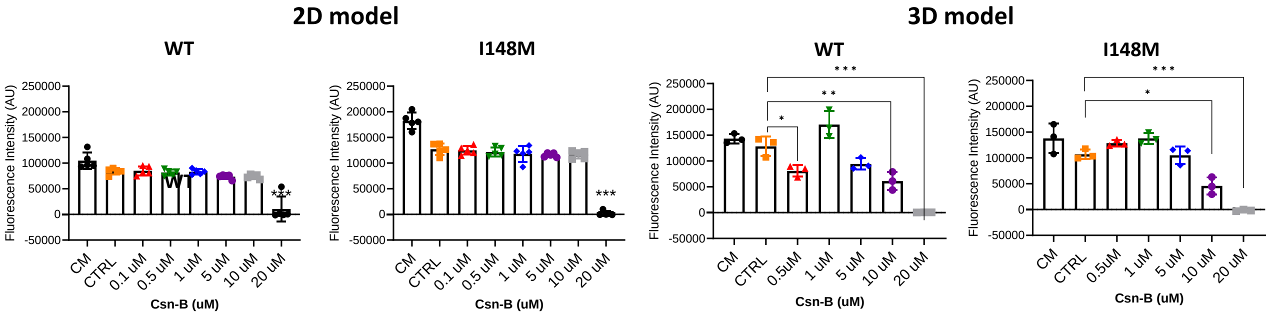

*Figure 23: **Effect of the natural agonist Csn-B on NR4A1 expression in WT-PNPLA3 or I148M-PNPLA3 genotyped HSCs: dose-response.** Viability response of HSCs WT or I148M-PNPLA3 cultured in 2D or 3D healthy ECM liver scaffolds to Cytosporone B (Csn-B). Cells were exposed with a dose escalation of Csn-B (2D: 0.1, 0.5, 1, 5, 10, 20 uM for 24h, N =5 per condition; 3D: 0.5, 1, 5, 10, 20 uM for 48h*3, N= 3 per condition, N=1 donor per genotype; data analysed via one-way ANOVA with Tukey's multiple comparison test).*

Therefore, 1µM and 5µM were chosen as low and high concentrations of Csn-B for the following experiments. Gene expression analysis showed a Csn-B dependent upregulation of NR4A1 only in PNPLA3-WT HSCs grown in healthy scaffolds (Figure 24A), while total NR4A1 protein was significantly increased by Csn-B (1µM) only in I148M-PNPLA3 HSCs cultured on healthy scaffolds. Interestingly, the phosphorylated fraction of NR4A1 was decreased by Csn-B (1µM) in both WT and PNPLA3-I148M HSCs, but only when the cells were cultured in healthy scaffolds (Figure 24B and 24C).

A)

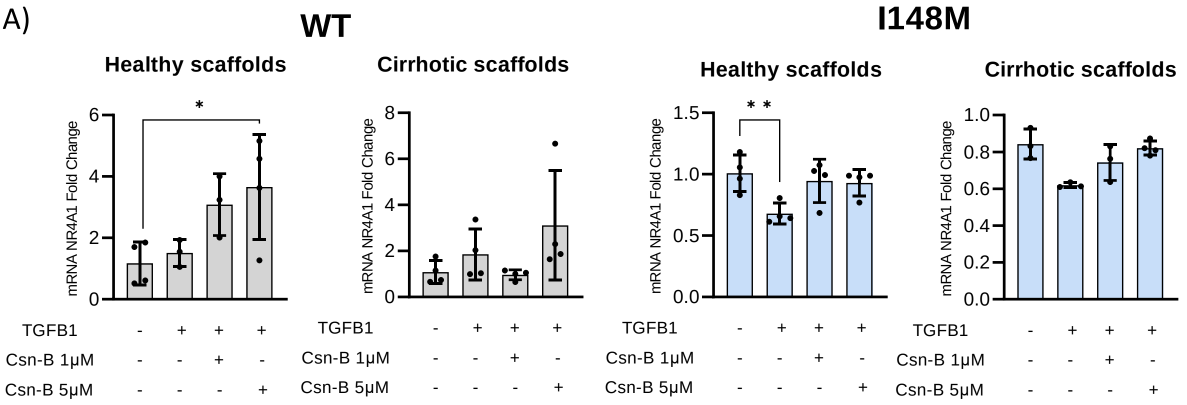
WT
I148M
Healthy scaffolds
Cirrhotic scaffolds
Healthy scaffolds
Cirrhotic scaffolds
mRNA NR4A1 Fold Change
*
* *
TGFB1 - + + +
Csn-B 1μM - - + -
Csn-B 5μM - - - +

B)

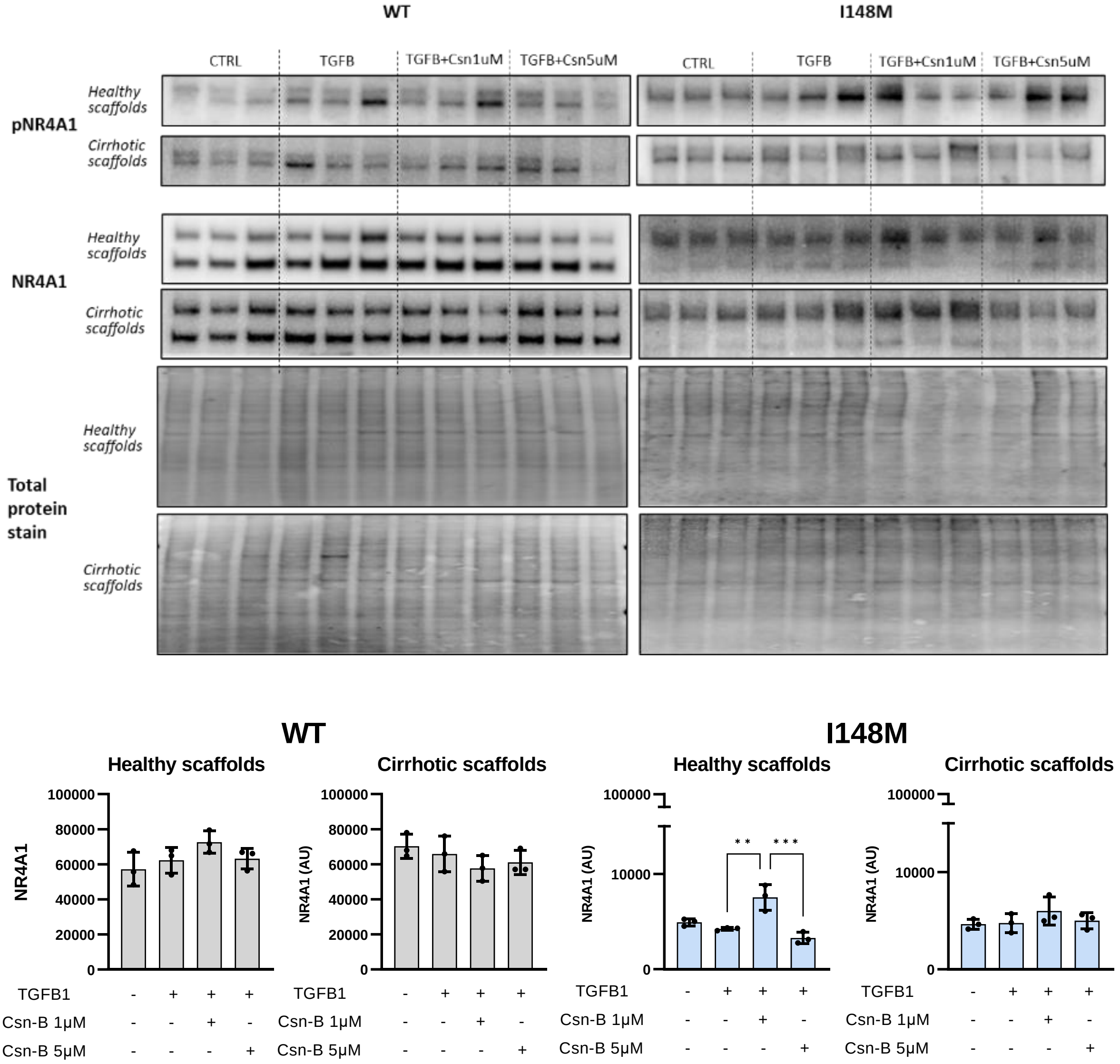
WT
I148M
CTRL
TGFB
TGFB+Csn1uM
TGFB+Csn5uM
pNR4A1
NR4A1
Total protein stain
Healthy scaffolds
Cirrhotic scaffolds
WT
I148M
Healthy scaffolds
Cirrhotic scaffolds
Healthy scaffolds
Cirrhotic scaffolds
NR4A1
NR4A1 (AU)
* *
* * *
TGFB1 - + + +
Csn-B 1μM - - + -
Csn-B 5μM - - - +

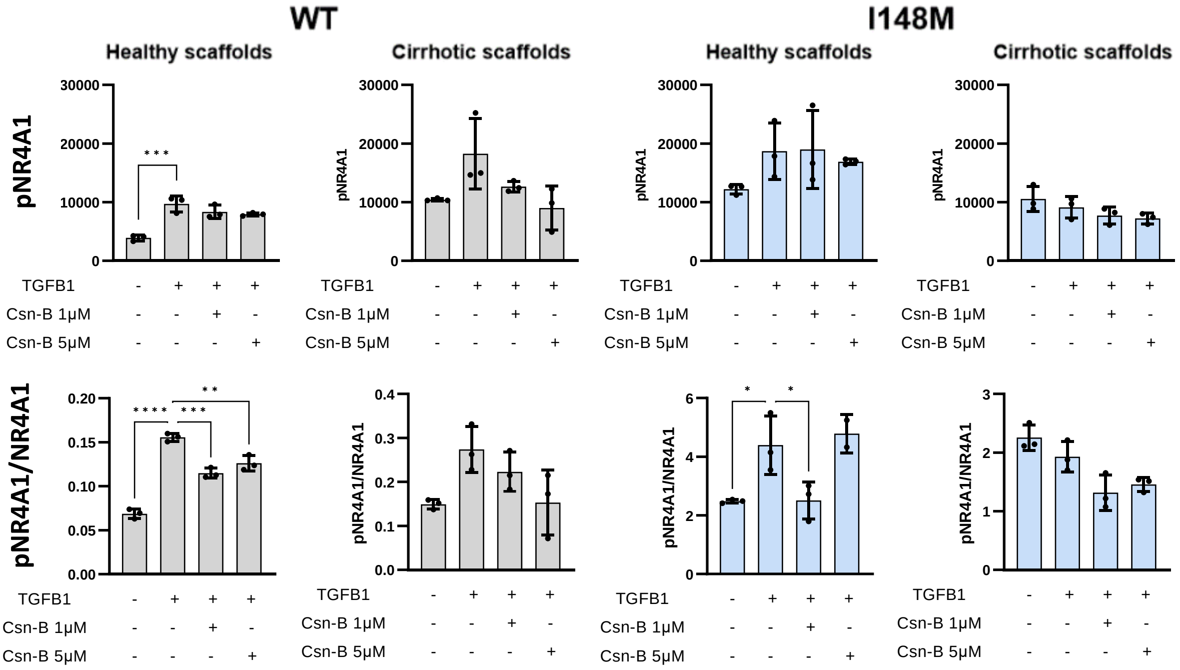

Figure 24: Effect of the natural agonist Csn-B on NR4A1 expression in WT-PNPLA3 or I148M-PNPLA3 genotyped HSCs: NR4A1. Analysis of expression of genes and proteins in PNPLA3-I148M vs WT HSCs cultured on healthy or cirrhotic scaffolds with TGFB1 (5ng/mL) and Csn-B (1µM or 5 µM). (A) Gene expression of NR4A1. (B) Protein expression of NR4A1, pNR4A1 and ratio of pNR4A1 to NR4A1. Blots from WT and I148M-PNPLA3 HSCs or healthy and cirrhotic scaffolds were processed in parallel. (****/***/**/*$p<0.001/0.005/0.01/0.05$, N=1 donor per genotype, N=4/3 biological replicates per condition (gene expression/protein expression); data analysed via one way ANOVA with Tukey's multiple comparison test).

3.3.7 Cytosporone-B attenuates TGFB1-induced production of COL1A1 and increases antioxidant enzymes in both WT and PNPLA3-I148M HSCs.

Treatment with Csn-B decreased COL1A1 protein expression at both 1µM and 5µM and in both WT and PNPLA3-I148M HSCs cultured in healthy and cirrhotic scaffolds (Figure 25). TGFB1 protein expression was also downregulated by Csn-B in PNPLA3-WT HSCs, whereas the effect was not significant in PNPLA3-I148M HSCs (Figure 26).

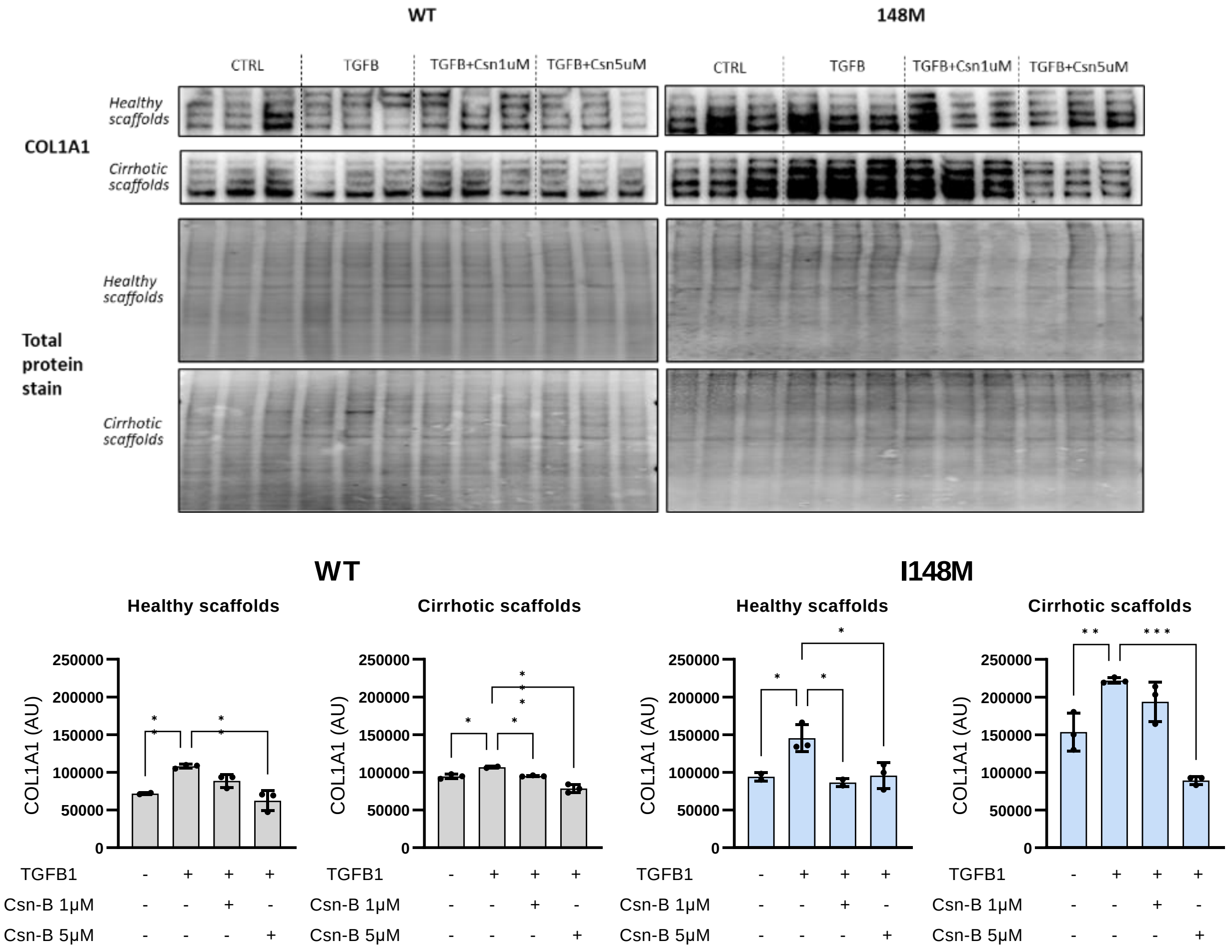

Figure 25: Effect of the natural agonist Csn-B on activation markers and antioxidant enzymes in WT-PNPLA3 or I148M-PNPLA3 genotyped HSCs: COL1A1. *Protein expression of COL1A1 in PNPLA3-I148M vs WT HSCs cultured on healthy or cirrhotic scaffolds with TGFB1 (5ng/mL) and Csn-B (1μM or 5 μM). Blots from WT and I148M-PNPLA3 HSCs or healthy and cirrhotic scaffolds were processed in parallel. (***/**/*p<0.005/0.01/0.05, N=1 donor per genotype, N=3 biological replicates per condition; data analysed via one way ANOVA with Tukey's multiple comparison test).*

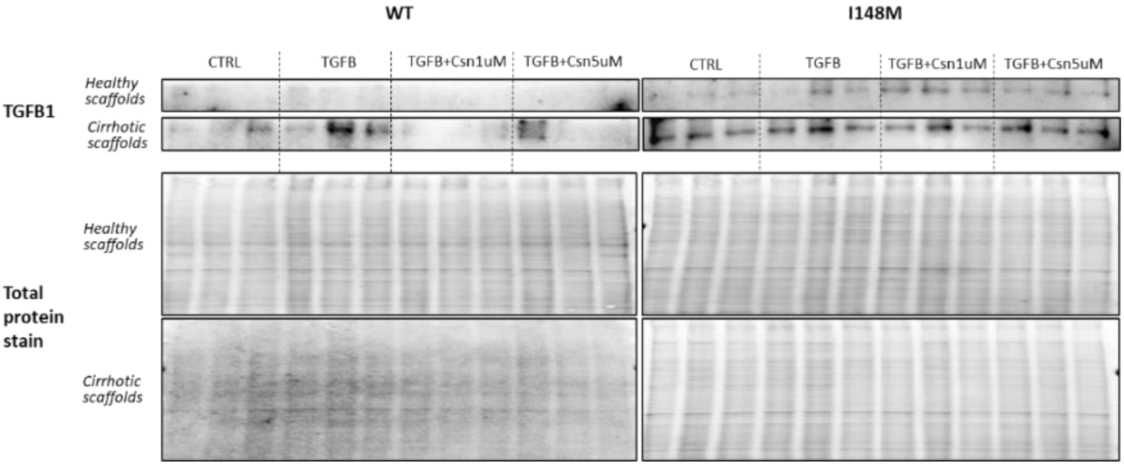

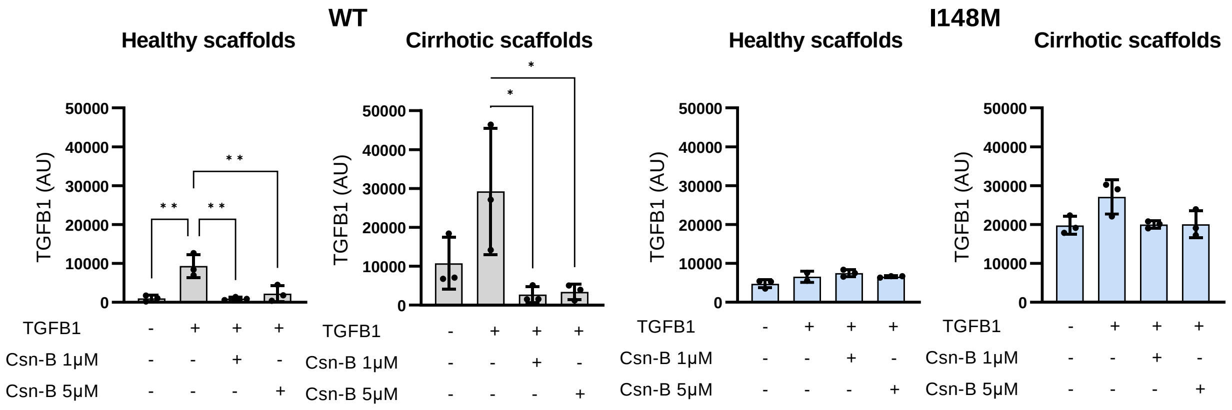

Figure 26: Effect of the natural agonist Csn-B on activation markers and antioxidant enzymes in WT-PNPLA3 or I148M-PNPLA3 genotyped HSCs: TGFB1. *Protein expression of TGFB1 in PNPLA3-I148M vs WT HSCs cultured on healthy or cirrhotic scaffolds with TGFB1 (5ng/mL) and Csn-B (1µM or 5 µM). Blots from WT and I148M-PNPLA3 HSCs or healthy and cirrhotic scaffolds were processed in parallel. (***/**/*p<0.005/0.01/0.05, N=1 donor per genotype, N=3 biological replicates per condition; data analysed via one way ANOVA with Tukey's multiple comparison test).*

Furthermore, secretion of Pro-Col1a1 followed a similar trend when HSCs were cultured in the healthy scaffolds but without reaching statistical significance (Figure 27).

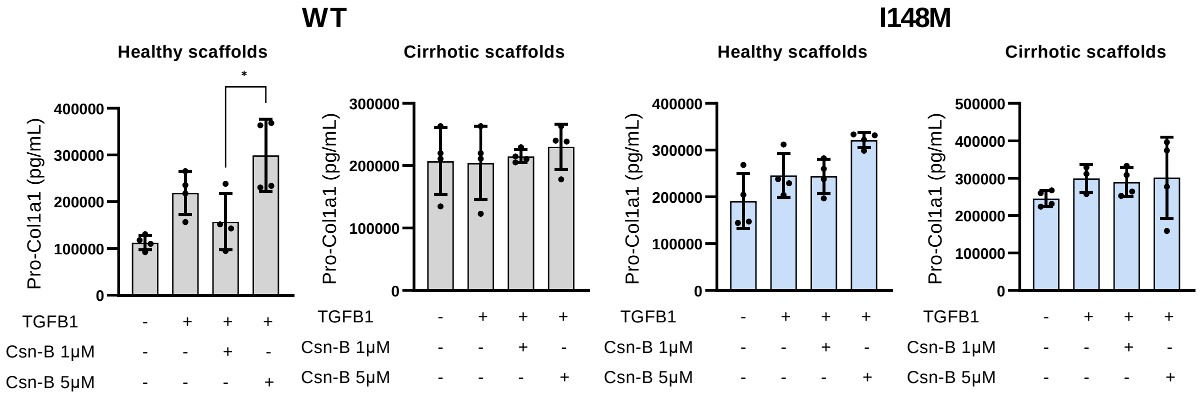

Figure 27: Effect of the natural agonist Csn-B on activation markers and antioxidant enzymes in WT-PNPLA3 or I148M-PNPLA3 genotyped HSCs: pro-COL1A1. *Protein secretion of pro-COL1A1 in PNPLA3-I148M vs WT HSCs cultured on healthy or cirrhotic scaffolds with TGFB1 (5ng/mL) and Csn-B (1µM or 5 µM). (***/**/*p<0.005/0.01/0.05, N=1 donor per genotype, N=3 biological replicates per condition; data analysed via one way ANOVA with Tukey's multiple comparison test).*

Important, treatment with Csn-B also increased NFR2 and CYGB gene and protein expression in PNPLA3-I148M HSCs cultured in healthy scaffolds, with a similar trend observed in PNPLA3-WT HSCs (Figure 28 and 29). Therefore, increasing total NR4A1 with consequent decrease of phospho-NR4A1 in HSCs induced a downregulation of pro-fibrogenic markers, with a stronger effect in PNPLA3-WT HSCs, and an increase in antioxidant enzymes in PNPLA3-I148M HSCs. This effect was not associated with significant differences when the cells were cultured in the 3D cirrhotic ECM, clearly indicating an ECM-specific induced effect.

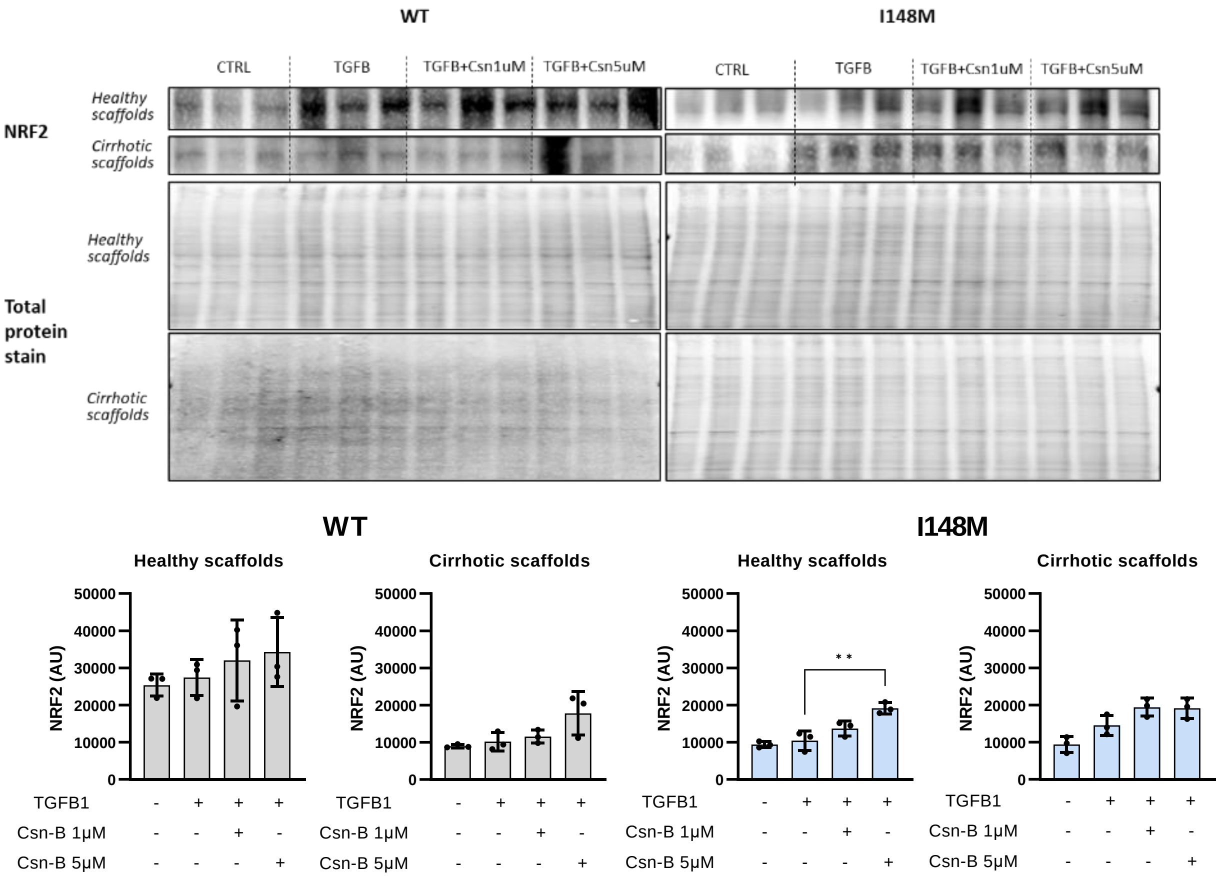

Figure 28: Effect of the natural agonist Csn-B on activation markers and antioxidant enzymes in WT-PNPLA3 or I148M-PNPLA3 genotyped HSCs: NRF2. *Protein expression of NRF2 in PNPLA3-I148M vs WT HSCs cultured on healthy or cirrhotic scaffolds with TGFB1 (5ng/mL) and Csn-B (1µM or 5 µM). Blots from WT and I148M-PNPLA3 HSCs or healthy and cirrhotic scaffolds were processed in parallel. (***/**/*p<0.005/0.01/0.05, N=1 donor per genotype, N=3 biological replicates per condition; data analysed via one way ANOVA with Tukey's multiple comparison test).*

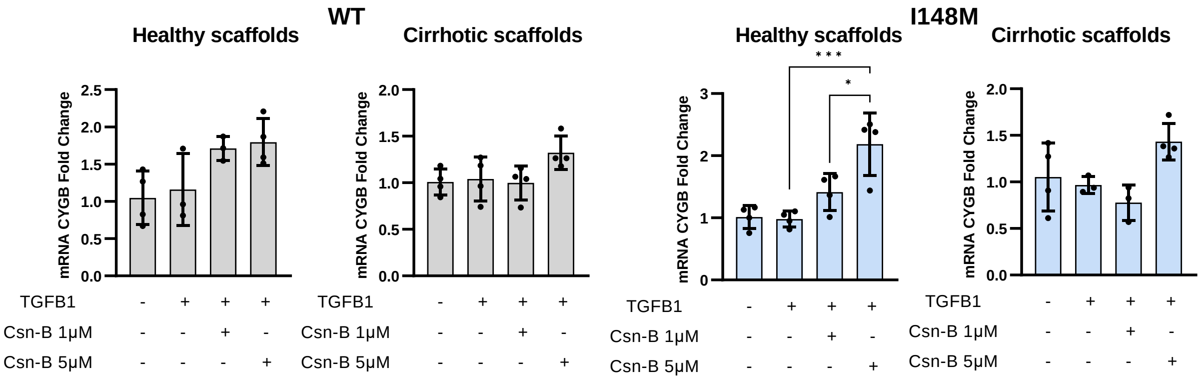

Figure 29: Effect of the natural agonist Csn-B on activation markers and antioxidant enzymes in WT-PNPLA3 or I148M-PNPLA3 genotyped HSCs: CYGB. *Gene expression of CYGB in PNPLA3-I148M vs WT HSCs cultured on healthy or cirrhotic scaffolds with TGFB1 (5ng/mL) and Csn-B (1µM or 5 µM). Blots from WT and I148M-PNPLA3 HSCs or healthy and cirrhotic scaffolds were processed in parallel. (***/**/*p<0.005/0.01/0.05, N=1 donor per genotype, N=4 biological replicates per condition; data analysed via one way ANOVA with Tukey's multiple comparison test).*

3.3.8 NR4A1 phosphorylation is differently regulated in WT vs I148M-PNPLA3 HSCs

In chronic fibrogenic conditions, NR4A1 phosphorylation is reportedly mediated by Akt[105,107], while other MAPK kinases can be involved in inflammatory and cancerous conditions[108,109].To understand which mechanism might be driving NR4A1 phosphorylation in WT and PNPLA3-I148M HSCs, the expression of different kinases in HSCs treated with TGFB1 and Csn-B 1 or 5 µM was investigated.

In PNPLA3-WT HSCs, TGFB1 increased the phosphorylated fraction of Akt, and when combined with Csn-B, this effect was annihilated, suggesting a consequent Akt-driven phosphorylation of NR4A1 in these cells; this was not observed in PNPLA3-I148M HSCs (Figure 30A). Important, TGFB1 increased the phosphorylated fraction of Erk, and this effect was annihilated when combined with Csn-B, in PNPLA3-I148M but not WT HSCs (Figure 30B). This suggests a different mechanism of phosphorylation of NR4A1, which is driven by Akt in HSCs PNPLA3-WT but by ErK in PNPLA3-I148M HSCs.

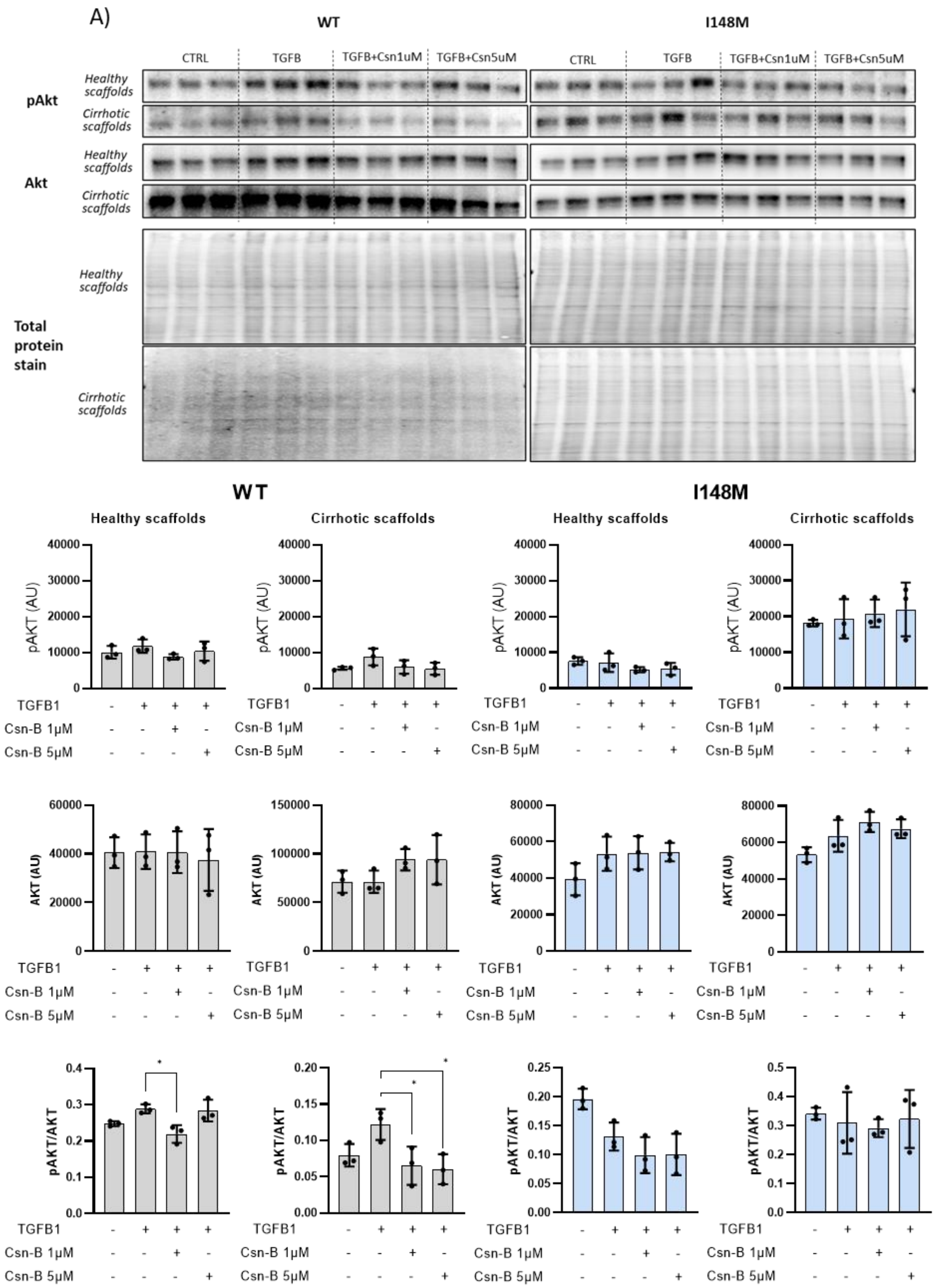
A)
WT
I148M
CTRL
TGFB
TGFB+Csn1uM
TGFB+Csn5uM
pAkt
Akt
Total protein stain
Healthy scaffolds
Cirrhotic scaffolds
WT
I148M
Healthy scaffolds
Cirrhotic scaffolds
pAKT (AU)
AKT (AU)
pAKT/AKT
TGFB1
Csn-B 1µM
Csn-B 5µM
*

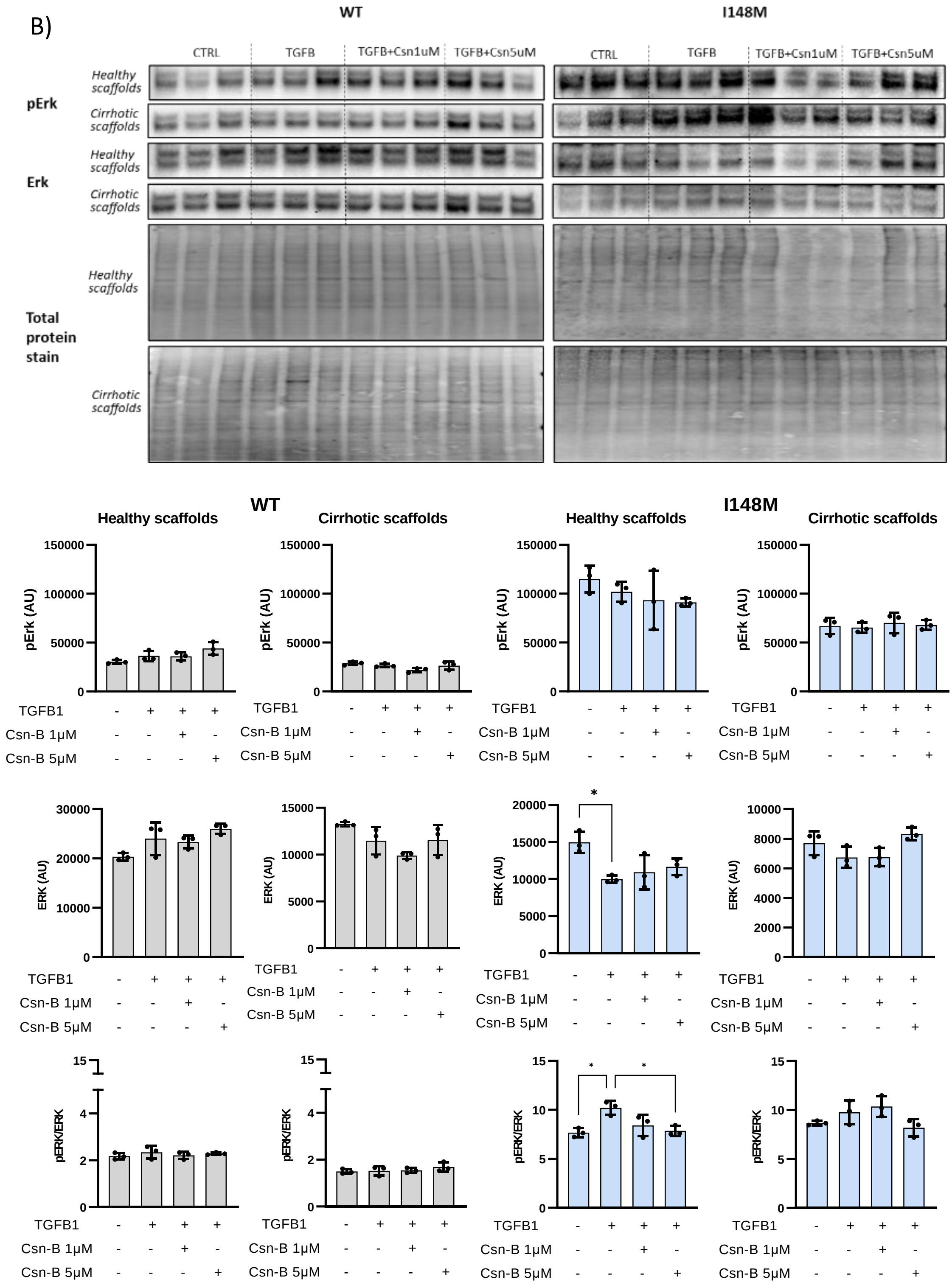

*__Figure 30: Mechanism controlling NR4A1 activation in WT-PNPLA3 or I148M-PNPLA3 HSCs cultured on healthy or cirrhotic scaffolds.__ A) Protein expression of Akt and phospho-Akt in WT-PNPLA3 or I148M-PNPLA3 genotyped HSCs cultured on healthy or cirrhotic scaffolds treated with TGFB1 (5ng/mL) and Csn-B (1 µM or 5 µM) for 48h*3; B) Protein expression of Erk and phospho-Erk in WT-PNPLA3 or I148M-PNPLA3 genotyped HSCs cultured on healthy or cirrhotic scaffolds treated with TGFB1 and Csn-B (1 µM or 5 µM) for 48h*3. Blots from WT and I148M-PNPLA3 HSCs or healthy and cirrhotic scaffolds were processed in parallel. (*p<0.05, N=1 donor per genotype, N=3 biological replicates per condition).*

3.4 Discussion.

The PNPLA3 I148M variant accounts for the largest fraction of inherited predisposition to develop any progressive chronic liver disease, including evolution of cirrhosis and hepatocellular carcinoma[58,60,72]. This variant has been associated with liver fat accumulation, hepatic inflammation, and susceptibility to developing fibrosing steatohepatitis[58]. Furthermore, several studies have proven the association between I148M PNPLA3 and the development and severity of liver fibrosis[70–72] and have showed how PNPLA3 is correlated to HSCs activation[73]. Nonetheless, the mechanism underlying the profibrogenic effect of PNPLA3 on human HSCs have not been clarified yet. In this study, we used comparative transcriptomic analysis of both *in vitro* cultured HSCs and patient liver biopsies to identify a PNPLA3 I148M-driven disrupted mitochondrial function and antioxidant response in HSCs. This was accompanied by increased TGFB1 signalling dampening the antifibrotic NR4A1 activity.

Mitochondrial dysfunction is related to the development of various liver diseases[110] and has been established as one of the driving forces for the progression of NAFLD[111]. Despite the attempts of the liver to recover from fat accumulation by increasing OXPHOS in the initial phase of NAFLD, mitochondrial adaptation is insufficient to stop the progression of the disease, leading to impaired mitochondrial respiration and decreased OXPHOS in NASH[112,113]. The presence of the PNPLA3 I148M mutation has already been associated with a decreased mitochondrial function in Huh-7 hepatoma cells and LX2 cells overexpressing PNPLA3 I148M[74,114]. In this study we showed that patient-isolated HSCs carrying the PNPLA3 I148M mutation had a lower OCR compared to wild-type cells. In addition, we demonstrated in our model a lower expression and enzyme functionality of Complex IV of the mitochondrial electron chain contributing to this process. Complex IV showed to be decreased both in patients with NAFLD[115], in animal models of fatty liver disease[116], HBV-infected cells[117] and is the most common respiratory chain complex involved in liver failure[118]. Importantly, we were able to link complex IV insufficiency to the *PNPLA3* I148M variant and thus with mitochondrial dysfunction in HSCs. Abnormal reduction of respiratory complexes promotes the production of superoxides[119], which are strongly associated with the progression of chronic liver disease[120]. In physiological conditions, ROS are produced at different sites of the respiratory mitochondrial chain as by-products of energetic metabolism and are important for physiological redox signalling; overproduction of ROS and impaired capacity of the antioxidant system leads to oxidative stress[121]. Studies have shown that loss of Complex IV in brain and heart tissue causes a three-fold increase in the level of ROS produced at the level of complex I by mitochondria[122]; accordingly, we observed an increase secretion of ROS in HSCs carrying the PNPLA3 I148M variant. The major increase was observed for secreted 4-HNE, a product of lipid peroxidation, which happens when oxidants such as free radicals or nonradical species attack lipids such as PUFAs or cell membrane lipids[123]. Lipids peroxidation products have been shown to damage mitochondrial genome[124], and 4-HNE and MDA can directly attack and inactivate respiratory chain components including Complex IV[125], therefore suggesting a vicious circle triggering ROS generation by the respiratory chain[111].

In addition, we also observed a decreased antioxidant capacity of I148M-PNPLA3 HSCs, which showed low levels of CYGB, NRF2 and SOD2 compared to wild type cells. This is in accordance with patient and *in vivo* animal data of NAFLD and NASH[126–128], as well as the further hampering of antioxidant enzyme quantity caused by the presence of TGFB1.

As previously reported[74,129], TGFB1 modulates PNPLA3 expression in HSCs and we demonstrated in the present study that *PNPLA3*-I148M HSCs are characterized by an increased TGFB1 signalling, which is known to increase the pro-fibrogenic and inflammatory features[130] as well as oxidative stress in HSCs[101]. Recently, NR4A1 was identified as an inhibitor of TGFB1 signalling in the context of chronic fibrogenesis[105] and was reported to be enriched in HSCs in the liver (Human Protein Atlas, data available from v21.1.proteinatlas.org[131]), and proposed as a newly anti-fibrogenic marker[132–134]. Our transcriptomic data suggested a dysregulation of NR4A1, which we confirmed by a marked decrease and inactivation of the nuclear receptor protein in I148M-PNPLA3 HSCs, coinciding with an increase of TGFB1 and COL1A1 expression. This effect was abolished by treatment with Csn-B, an agonist of NR4A1, which decreased NR4A1 phosphorylation, thus counteracting the profibrogenic effect of TGFB1 and directly implicating NR4A1 in the mechanism by which PNPLA3-I148M promotes HSC activation. Interestingly, our data suggest that the mechanism leading to the phosphorylation of NR4A1 might be different between WT and PNPLA3-I148M HSCs. In fact, Akt seemed to drive the phosphorylation of NR4A1 in WT HSCs treated with TGFB1, in agreement with other studies on fibroblasts in chronic fibrotic conditions[105]. On the other hand, in HSC carrying the PNPLA3 variant the same process seemed to be driven by Erk, as it is mainly observed in cancerous conditions[108]. This will need to be confirmed by further studies but supports the existence of different molecular mechanisms and activated pathways related to the presence of the PNPLA3 I148M variant, and the potential for the variant to facilitate cancer development[135].

In addition, the increase in NR4A1 activity, induced by treatment with Csn-B, was associated with an increase in the antioxidant enzyme NRF2 in PNPLA3-I148M HSCs, suggesting an inhibitory effect of NR4A1 on both the fibrogenic and oxidative stress pathways in HSCs. NR4A1 is involved in regulating oxidative stress in different conditions depending on cell type and pathological conditions investigated[136–139]: while it is key in maintaining mitochondrial homeostasis in vascular smooth muscle cells (VMSCs)[136] and in a vascular model of diabetes[137], it also promotes oxidative stress in a model of diabetic cardiomyopathy[138] and one of hepatocyte ischemia-reperfusion injury[139], therefore further studies on the involvement of NR4A1 in oxidative stress in HSCs are needed. Importantly, NR4A1 expression has been found to be beneficial in mouse hepatocytes by promoting FGF21 secretion[140] and in HepG2 treated with FFAs by reducing lipid accumulation[141], which, together with our findings in HSCs, makes it an interesting target for the treatment of fatty liver disease.

It is important to note the differential response of both WT and I148M PNPLA3 HSCs when cultured on 3D cirrhotic ECM compared to 3D healthy ECM. More specifically, the impact on cell behaviour driven by the cirrhotic ECM on oxidative stress *versus* antioxidant enzymes expression, the increased TGFB1 and COL1A1 expression, and the decreased NR4A1 content together with the inability of Csn-B to increase NR4A1 expression when HSCs were cultured on the 3D cirrhotic scaffolds. These effects can be attributed to the differences in ECM protein composition[37], 3D-architecture, and physico-chemical properties[36], as previously shown by our group[35]. Overall, our study indicates the need of a complex 3D model which includes the presence and tissue architecture of the cirrhotic ECM that can provide much more information compared to cell culture on plastic or 3D models devoid of normal or pathological human liver ECM.

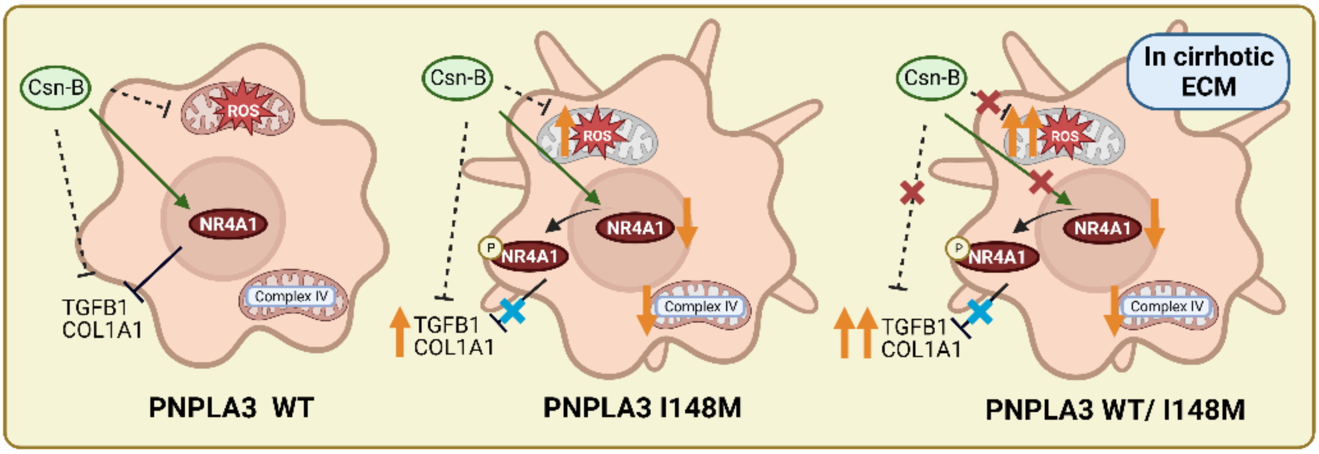

Figure 31: Schematic of the effect of the PNPLA3 I148M mutation on mitochondrial activity, oxidative stress and NR4A1 regulation in HSCs. *Created with Biorender.*

The development of a more complete model for NAFLD/NASH with the addition of other liver cell types and treatments with lipids and insulin to mimic the physiological conditions of the disease is though necessary to further confirm our findings and exploit the differences of healthy and cirrhotic ECM. Furthermore, investigation of how other mutations might impact the behaviour of HSCs in presence of the PNPLA3 I148M mutation would be useful, as combinations of different mutations has been proven to impact the development of NAFLD/NASH[142,143].

In summary, our study demonstrates the impact of the *PNPLA3* I148M variant on HSCs pathways deregulation, linking it for the first time with mitochondrial and antioxidant dysfunction. This was achieved by transcriptomic analysis of an *in vitro* model and patients' samples followed by validation of findings in a complex 3D model of human liver decellularized scaffolds recapitulating healthy and cirrhotic liver microenvironment. Furthermore, our study highlights the importance of TGFB1 and its endogenous inhibitor NR4A1 in HSCs fibrogenesis and in the context of the *PNPLA3* variant, with NR4A1 being a potential antifibrotic drug target for the treatment of chronic liver diseases.

4 Modelling liver fibrosis in three-dimensional liver extracellular matrix hydrogels

4.1 Introduction.

4.1.1 Hepatic stellate cells contraction and liver disease.

HSCs are well-known as the key mediators of liver fibrosis. As described above, upon liver injury, their activation and transdifferentiation into myofibroblast-like cells leads to increased proliferation and secretion of pro-fibrogenic and pro-inflammatory cytokines, initiating the fibrogenic progression of chronic liver disease[12]. Physiologically, HSCs function as liver specific pericytes[144], in reason of their capacity of contracting to maintain and adequate sinusoidal pressure. In fact, activated HSCs can contract in response to contractile stimuli such as Endothelin-1 or Angiotensin II, and are localized in the perisinusoidal space where they present with extended protrusions which can encircle one or more sinusoids[145]. Therefore, HSCs are involved in the regulation of blood flow and sinusoidal tone in the normal liver[146], while in presence of injury, HSCs have been indicated as the major players in the increase in portal pressure which is a key feature of fibrotic liver[144]. Portal pressure increase is not only due to HSCs contraction, but also to the extracellular matrix deposition and remodelling which induces architectural distortions in the sinusoids. This process is the results of a complex cross-talk between HSCs and liver sinusoidal endothelial cells (LSECs) which, upon injury, loose their ability to produce vasodilators such as nitric oxide (NO) to counteract the predominance of vasoconstrictors (so-called "endothelial dysfunction"), happening in the early phase ("initiation") of HSCs activation[12] (Figure 32).

Therefore, HSCs contraction has been shown to be a key contributor in the early fibrogenic phase of chronic liver disease, and an interesting target for disease management.

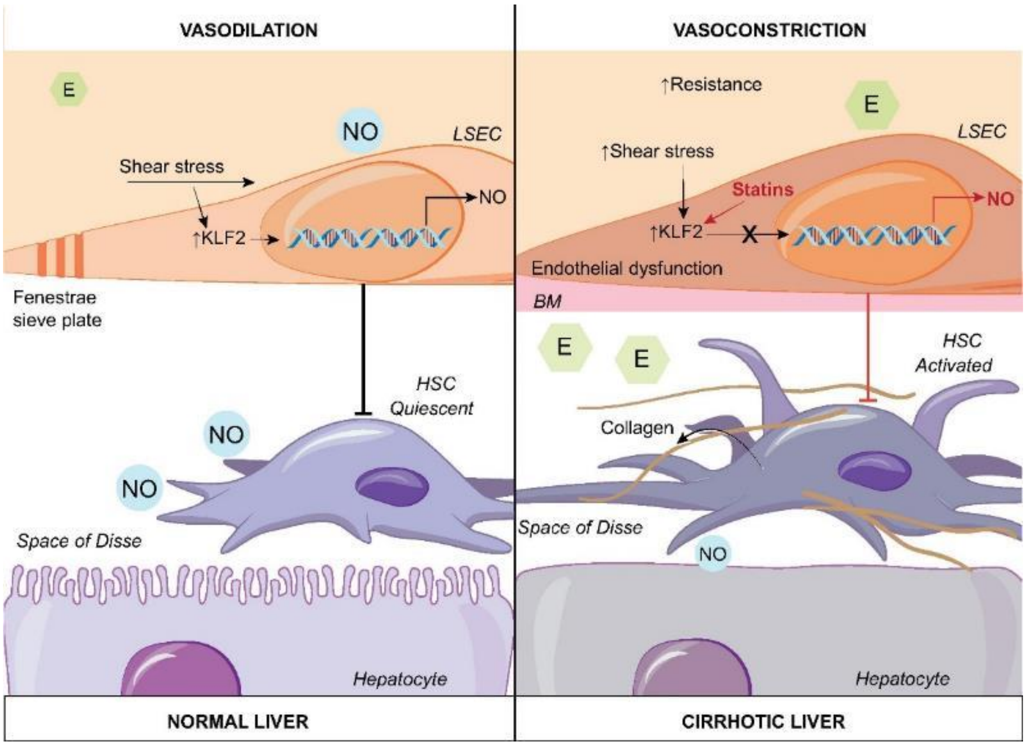

Figure 32: Crosstalk between LSECs and HSCs. *Poisson et al., "Liver sinusoidal endothelial cells: Physiology and role in liver diseases", Journal of Hepatology, 2017*

4.1.2 The TM6SF2 E156K genetic variant in hepatic stellate cells and liver disease.

Genetic variants have a significant impact in the predisposition to develop any chronic liver disease[66], and therefore, the combination of several genetic risk factors in polygenic risk scores has recently been proposed to improve diagnostic accuracy[147]. The cellular mechanisms induced by the additive weight of different mutations have only partially been explored[142,148], although combination of several variants has been shown to have important impacts on the severity and progression of CLD[149]. A recent study found that the prevalence of NAFLD was 5-fold higher in patients carrying both the PNPLA3 I148M and the TM6SF2 E156K mutations compared with patients with none or a single variant[150]. Therefore, the additive impact of the PNPLA3 I148M and TM6SF2 E156K variants on HSCs was explored in this chapter.

The transmembrane 6 superfamily member 2 (TM6SF2) E156K variant (rs58542926) is a single nucleotide polymorphism which had been initially identified as a risk locus for the development of NAFLD[59]. TM6SF2 is an enzyme mainly found in the kidney, small intestine and liver, and is predominantly expressed in the intermediate compartment of the endoplasmic reticulum[59] and involved in the regulation of hepatic lipid efflux[151]. The E156K variant leads to misfolding and increase degradation of the TM6SF2 protein[59], which results in reduced secretion of hepatic lipoproteins (very low-density lipoproteins (VLDL), triglycerides (TG) and apolipoprotein B (APOB), increased accumulation of hepatocellular lipid droplets, and higher TG levels[151]. In recent years, the E156K variant of the TM6SF2 protein has also been associated with advanced hepatic fibrosis and cirrhosis[152] and has been found to favour NASH development through regulation of cholesterol metabolism in hepatocytes[153]. Furthermore, the TM6SF2 E156K variant has been identified as a risk locus for the development of ALD-related cirrhosis[72], liver damage in patients with hepatitis B virus or HCV[154,155] and for the onset of HCC[156]. Although the effects of the TM6SF2 E156K variant in hepatocytes have been partially unravelled and are mostly related to lipid metabolism and triglycerides accumulation[157], very few studies have looked into the effect of the variant on HSCs. Recently, the loss of function of TM6SF2 has been shown to increase the expression of activation markers and responsiveness to TGFB1 in LX2 cells[158], but in-depth studies to further understand the topic are needed.

4.1.3 Hydrogels as three-dimensional *in vitro* models.

The development and functionalization of biomaterials have been actively pursued to enable more effective applications of tissue engineering. In particular, hydrogels have promising biomedical applications as *in vitro* 3D models for their capability to be scaled up in production and to be easily utilized in co-culture studies.

Hydrogels can be classified according to their physical properties, source of origin, method of preparation, nature of swelling, ionic charges, rate of degradation, biocompatibility and nature of crosslinking[159]. When looking at their origin, hydrogels can be classifies as natural, such as alginate, collagen, agarose or chitosan, or synthetic hydrogels, such as poly(vinyl alcohol) (PVA) or poly(ethylene glycol) (PEG)[160]. Composite hydrogels are formed by mixtures of different constituents with diverse chemical, physical and biological properties, and therefore are often preferred for the modelling of human tissues[161]. The method of crosslinking is another important feature of hydrogels; in fact, hydrogels can be divided into chemically or physically crosslinked hydrogels. While chemical crosslinking is irreversible, networks induced by physical crosslink can be reverted. Physical crosslinking can be due to radical polymerization, chemical reaction of complementary groups, ionic interactions, crystallization or environmental stimuli such as pH, temperature or light[159,162].

Hydrogels in tissue engineering must meet several design criteria to mimic the organ-specific ECM and consequently function appropriately and promote new tissue formation. In order to develop human-like scaffolds, hydrogels have been engineered to mimic as much as possible the native ECM: artificial matrices have been enriched with cell adhesive peptides like the RGD sequence, growth factors such as VEGF, or heparin as a reservoir for growth factors[163–165]. Nonetheless, synthetic hydrogels still fail to recapitulate important features of the ECM such as the fibrillar structure of collagen, the potential for cellular remodelling of it and the proper distribution of soluble factors[166].

To overcome these issues, many have attempted to use single, or combination of ECM proteins extracted from tissue to create 3D scaffolds *in vitro*. Different protocols have been developed to promote gelation of ECM proteins, mainly involving self-gelation or the usage of polysaccharides hydrogels. Though, ECM-resembling hydrogels produced in this manner are still mainly synthetic, or derived from xenogenic and/or carcinogenic origin, such as Matrigel[167]. Furthermore, recent studies have investigated the exact composition of the ECM in healthy and diseased human liver, identifying several hundreds of components and a significant difference in presence of liver disease[37,168]. The abundancy of different ECM proteins hampers the possibility of pooling them all together to create *in vitro* scaffolds and points out the limitations in resembling physiological and pathological complexity of the microenvironment by just adding small sets of ECM proteins within an artificial substrate[169,170]. To bypass this problem, our group has developed ECM solutions derived from the decellularization of healthy and cirrhotic human livers, which therefore retain all the major components of the human liver extracellular matrix[171]. These solutions can be combined with different gelling agents to form hydrogels which can be used for the set-up of *in vitro* cultures of human liver cells.

In this project, the liver ECM solutions have been combined with two different gelling agents: the first one is a thermo-responsive biocompatible PGMA-PHPMA diblock copolymer able to self-assemble in situ to form worm-like micelles and at 21°C, generating a soft free-standing physical hydrogel. Gel dissolution of this polymer occurs on cooling at 4°C, and the gel has proven to be biocompatible and support cell viability of human pluripotent stem cells and human embryos[162,172].

The second gelling agent is a commercially available mixture of alginate and nanofibrillated cellulose (Cellink Bioink) which forms a gel upon ionic crosslinking with an aqueous solution of calcium chloride, distributed by CELLINK and described in[173].

4.2 Materials and methods.

4.2.1 LX2 cells culture.

The Human HSC line LX2 was kindly given by Scott Friedman, Mount Sinai NY, USA, and was cultured in Iscove's Modified Dulbecco's Medium (IMDM) supplemented with 10% FBS, 2mM glutamine, 1X Antibiotic-Antimycotic, 1mM Sodium Pyruvate and 1X non-essential amino acids (Life Technologies, Paisley, UK). Cells were maintained in standard conditions in a humidified incubator under 5% CO_2 in air at 37°C. Medium was refreshed twice a week and cells were passaged when subconfluent with 1X Trypsin (2.5% trypsin 10x, Gibco).

4.2.2 DNA extraction and genotyping of primary human HSCs.

DNA was extracted from different HSCs donors using DNA Blood and Tissue Extraction Kit (Qiagen) and subsequently used for genotyping. The genotype of each isolated HSC donor was determined by real-time PCR for the rs738409 C>G (PNPLA3 I148M) and rs58542926 C>T (TM6SF2 E156K) single-nucleotide polymorphism using a TaqMan SNP Genotyping Assay (Life Technologies, UK) as described in Chapter 3 above.

4.2.3 Liver ECM solution preparation.

Scaffolds obtained from human livers unsuitable for transplantation were decellularized following the protocol developed and published by Mazza et al. in 2017/2019 and described in the previous chapter (Table 1)[36,37]. The human decellularized liver scaffolds were then lyophilized (VIRTIS benchtop) overnight to obtain a dried tissue that was then milled (rotary knife milling machine, Lavalaib) to create human liver ECM powder. Human liver ECM powder was solubilised in 0.5M acetic acid (Fisher Scientific) at a concentration of 6mg/mL, with the addition of 20% of Pepsin from porcine gastric mucosa (Sigma Aldrich), at 37 °C for 72 hours under magnetic stirring. The pH of the resultant ECM solution was then neutralised with 10N sodium hydroxide (30 µl per each ml of ECM solution), and the osmotic pressure was adjusted with 10X PBS (1:10 volume of ECM solution), (L. Frenguelli et al., unpublished data). This ECM solution was utilized to prepare both HepGel and ECM Gel.

4.2.4 Synthesis of $PGMA_{55}$-$PHPMA_{135}$ diblock copolymer worms for HepGel production.

The $PGMA_{55}$-$PHPMA_{135}$ diblock copolymer worms were synthetized in the laboratory of Prof. Giuseppe Battaglia (UCL, Department of Chemistry).

Poly(glycerol monomethacrylate) (PGMA) was obtained by purging with N_2 glycerol methacrylate (GMA) and 2-Cyanopropyl Dithiobenzoate (CPDB). After 4,4-azobis (4-cyanopentanoic acid) (ACVA) addition and degassing, the solution was immersed for 2 hours in an oil bath set at 70 °C to obtain $PGMA_{55}$. The polymer was purified by precipitating twice into excess dichloromethane from methanol, and the aqueous solution was freeze-dried overnight to obtain a pink powder.

$PGMA_{55}$ and 2-hydroproxyl methacrylate (HPMA) were purged with N_2. Then ACVA was added, and the solution was degassed. Phosphate Buffered Saline (PBS) solution was then added to obtain $PGMA_{55}$-$PHPMA_{135}$ diblock copolymer worms, which were then further diluted with PBS to reach a concentration of 10% w/v. The solution was cooled to 4°C to induce the worm-to-sphere transition to a cold low-viscosity fluid. The fluid was then ultrafiltered using a sterile 0.20 µm syringe filter and stored at 4°C[172].

4.2.5 HepGel preparation.

The desired amount of HepGel was prepared mixing the cold (4°C) $PGMA_{55}$-$PHPMA_{135}$ diblock copolymer solution and the cold (4°C) liver ECM solution in a 50:50 ratio (vol/vol) and kept in ice to obtain HepGel solution. The optimal ratio of liver ECM solution, and gelling agent, was previously optimized by L. Frenguelli[171].

4.2.6 ECM Gel preparation.

The desired amount of ECM Gel was prepared by mixing Cellink Bioink / ECM solution / cell suspension in a ratio 30/45/25. The optimal ratio was previously optimized (L.Frenguelli, unpublished). Healthy and cirrhotic ECM Gels were prepared with the same ratio of Cellink Bioink/ECM solution/cell suspension. Mock ECM Gels were prepared by using an ECM solution without ECM powder added. Nanocellulose only gels were prepared by using a Cellink Bioink/ECM solution/cell suspension ratio of 75/0/25.

4.2.7 Seeding of primary HSC and LX2 cells in HepGel.

A 48-well plate was pre-warmed in the incubator for at least 30 min, while the $PGMA_{55}$-$PHPMA_{135}$ diblock copolymer worm solution and the ECM solution were kept in ice before preparing the HepGel as described above.

Cells were washed with HBSS and trypsinised using Trypsin solution 1x in HBSS (2.5% trypsin 10x, Gibco). Trypsin was inactivated using HSC or LX2 complete culture medium and detached cells were centrifuged at 1600 rpm for 6 minutes at room temperature.

In a first experiment, optimal cell densities were established by using different concentrations of cells per HepGel. After discarding the supernatant, cells were resuspended in fresh HSCs or LX2 medium in order to have three different cell concentration for LX2 cells: 100 cells/μL – 300 cells/μL – 600cells/μL, and three different concentrations for primary HSCs: 300 cells/μL - 600 cells/μL - 1200 cells/μL. Afterwards, a volume of cell suspension was added to the ECM hydrogel solution in a 1:100 ratio. 50 μL of the HepGel comprising cells was pipetted in each well of a warm 48-well plate. After 5 min at room temperature to allow the ECM hydrogel solution to form a gel, 1 mL of warm cell culture medium was added in each well. After 24 hours, the cell culture medium was replaced with fresh warm cell culture medium; thereafter, the cell culture medium was replaced every 48 hours up to 11 days. Next, LX2 and HSCs behaviour in HepGel was investigated.

Treatment: After 7 days in culture, HepGel samples were treated with TGFB1 (5 ng/mL) for 2x 48 hours. The experiment was stopped at day 11. Samples were snap-frozen in liquid nitrogen and stored at -80°C until further experiments such as RNA extraction. For immunofluorescence staining, samples were fixed in formalin and immediately stained. Supernatants were collected at day7 and day 11 and kept at -80°C for further analysis.

4.2.8 Seeding of primary HSC in ECM Gels.

ECM Gel mixture was prepared as described above. Cells were washed with HBSS and trypsinised using Trypsin solution 1x in HBSS (2.5% trypsin 10x, Gibco). Trypsin was inactivated using HSC complete culture medium and detached cells were centrifuged at 1600 rpm for 6 minutes at room temperature.

In a first experiment, optimal cell densities were established by using different concentrations of cells per ECM Gel. After discarding the supernatant, cells were resuspended in fresh HSCs medium in order to have two different cell concentrations: 3000 cells/μL - 5000 cells/μL. Afterwards, a volume of cell suspension equal to the 25% of the total volume of the gel was added to the ECM Gel mixture. Fifty μL of the ECM Gel comprising cells mix was pipetted in each well of a 48-well plate. A 50 mM calcium chloride solution was added to the gels and incubated for 5 min to induce crosslinking and gel formation. After two washes with HBSS, 1 mL of warm cell culture medium was added in each well. After 24 hours, the cell culture medium was replaced with fresh warm cell culture medium; thereafter, the cell culture medium was replaced every 48 hours up to 14 days.

Treatment: After 7 days in culture, ECM Gel samples were treated with TGFB1 (5 ng/mL) for 3 x 48 hours. The experiment was stopped at day 14. Samples were snap-frozen in liquid nitrogen and stored at -80°C until further experiments such as RNA extraction. For contraction experiments, cells were treated at day14 with Endothelin-1 (1 μM) up to 30 minutes, with or without pre-treatment with TGFB1 (5ng/mL) for 3x48hours.

4.2.9 Live/Dead assay

The assay is based on two fluorescent dyes. Fluorescein Diacetate (FDA) is taken up by alive cells and converted into a green fluorescent metabolite, while Propidium Iodide (PI) stains the nuclei of damaged cells red. One sample for each cell density was stained with a solution of 4% PI and 2% FDA. Images were acquired with a Nikon Eclipse TE200 Fluorescence microscope. The assay was performed every 3 days from day0 to day11 or day14.

4.2.10 Immunofluorescence staining and contraction evaluation in HepGel.

After removing cell culture medium, samples were washed with PBS 1X pH 7.4 and fixed with Formalin 10% for 20 minutes at room temperature. After washing twice with

PBS 1X, samples were permeabilised with a solution of a 0.5% Triton X-100, 3% Bovine Serum Albumin (BSA) in PBS 1X for 1 hour at room temperature. After washing three times with PBS 1X, samples were stained for F-actin using Phalloidin TRICT (Sigma) diluted 1:200 in 3% BSA in PBS 1X for 1 hour at RT in the dark.

After washing for three times with PBS 1X, nuclei were counterstained with Hoechst 33258 diluted 2 µg/mL in PBS 1X for 30 minutes (Table 8). Before imaging, samples were washed three times with PBS 1X. All the steps were performed on an orbital shaker. Images were acquired with a Yokogawa CQ1 confocal microscope. Z-stacks of each part of the HepGel sample were acquired and then stitched together in order to have an image of the whole sample. The size of the whole sample/of each spheroid in the sample was measured with ImageJ/ CQ1 Yokogawa analysis software and compared between TGFB1-treated and untreated samples.

Staining	Name	Dilution	Company
F-actin	Phalloidin TRICT	1:200	Sigma-Aldrich
Nucleus	Hoechst 33258	2 µg/mL	Sigma-Aldrich

Table 8. List of fluorescent dyes used for immunofluorescence staining.

4.2.11 Contraction evaluation in ECM Gels.

Light photographs (1x magnification) were taken of the 50µL samples in order to investigate ECM Gels contraction (Figure 33). Endothelin-1 (AbMole BioScience) was dissolved in the appropriate volume of SFM to give a concentration of 1µM. An initial photograph was captured before stimulation (time=0). Subsequently, 100µL of the Et-1 solution was introduced into the ECM Gels medium and the samples were pictured after 10-seconds, 30-seconds, 1-minute, 2-minutes, 4-minutes, 8-minutes, 15-minutes, and 30-minutes. Total area of the hydrogels was calculated using ImageJ and expressed as reduced surface area percentage.

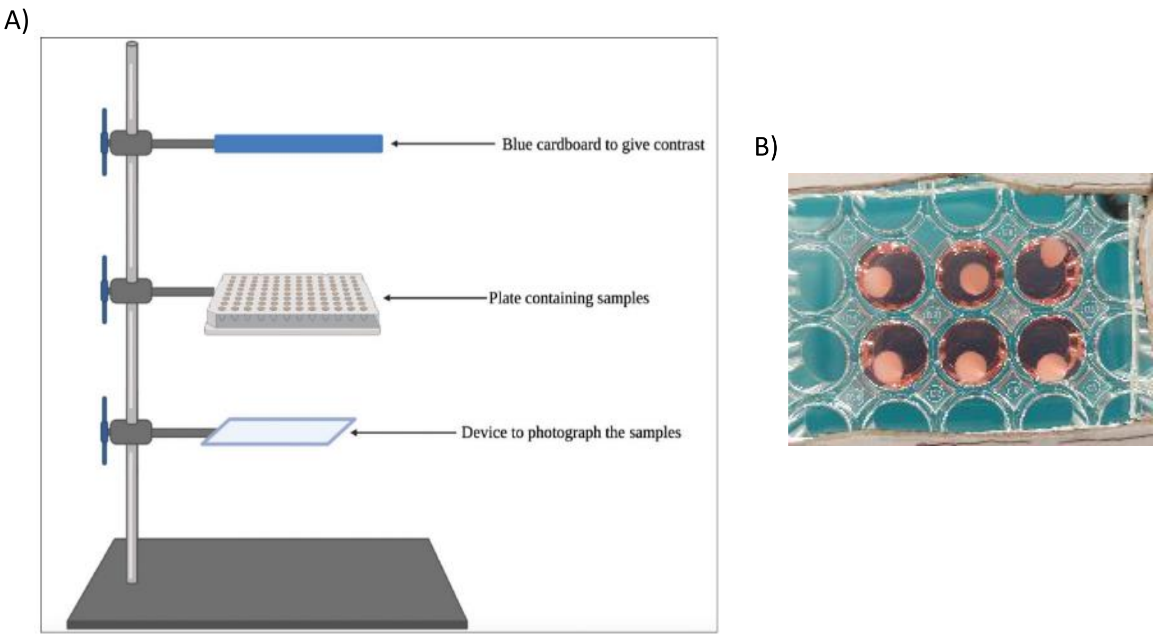

Figure 33: Set-up of the system to measure contraction of HSCs in ECM-gels. *(A) Schematic representation of the system set up to measure contraction in HSCs grown in healthy ECM-gels. (B) Representative picture of HSCs grown in ECM-gels for contraction quantification.*

4.2.12 Protein extraction and western blot.

The snap-frozen ECM Gels were lysed through the addition of radio-immunoprecipitation assay buffer (RIPA Buffer, Sigma Aldrich, Dorset, UK) containing protease inhibitor 1:100, sodium fluoride (NaF) 1:200, sodium vanadium oxide (NaVO) 1:200, and phenylmethylsulfonyl fluoride (PMSF) 1:100. The samples were agitated using the pipette then left on ice for 15-minutes and vortexed every 5-minutes followed by centrifugation for 15-minutes at 13000rpm 4°C. The supernatant was then collected in a 1.5ml Eppendorf and stored at -80°C. Western Blot was performed as described in the previous chapter.

4.2.13 Mechanical characterization.

ECM Gels in a 100µL volume were cast in a 96-well plate specifically for mechanical characterization, giving hydrogels of ~6.5mm diameter and ~2mm thickness. Hydrogels were characterized using dynamic mechanical analyser (DMA; Discovery DMA 850, TA instruments, New Castle, USA) at 37C as previously described[174]. Storage modulus (E') and Loss modulus (E") were measured by time sweep test where the hydrogels were subjected to a constant force of 10^{-3}N, constant frequency of 0.1

Hz and constant strain of 0.1% for 6 minutes. Young’s modulus was determined by static compression mode which was used to obtain stress/strain curves with ramp rate of 1mm/min. Moduli were calculated from the slope of the linear region on the stress/strain curve using GraphPad Prism v9.0.

4.2.14 Scanning Electron Microscopy.

ECM Gels were fixed by using glutaraldehyde 3% in 0.1M cacodylate buffer. The scanning electron microscopy images were taken by Carl Zeiss XB1540 SEM and SmartSEM software (equipped with tilt correction) at 5 kV operating voltage. Prior to the imaging, the samples were sputter-coated with Au.

4.2.15 Data analysis and statistics.

Immunofluorescence pictures were processed and analysed with ImageJ or Yokogawa CQ1 analysis software. The statistical analysis was performed using GraphPad Prism 9.0c software (Graph Pad CA, USA). Values are expressed as mean and standard deviation (SD). Statistical significance was analysed using t Student’s test or one/two/three-way ANOVA with Tukey’s multiple comparison test.

4.3 Results.

4.3.1 Thermo-responsive human liver extracellular matrix three-dimensional hydrogels for modelling liver fibrosis and evaluating HSCs contraction.

The preliminary results exposed in this subchapter were performed using only healthy extracellular matrix solution.

4.3.1.1 Assessment of LX2 cell density and viability in HepGel

Three different concentrations of LX2 cells (100 cells/µL – 300 cells/µL – 600 cells/µL) were seeded in HepGel and cultured for 14 days. Cell viability was evaluated every 3 days from day 0 to day 13 using PrestoBlue assay and Live/Dead assay.

As shown in Fig 34, LX2 cells were viable (Fig. 34A) and proliferated (Fig. 34B) when cultured in HepGel at both 300 cells/µL and 600 cells/µL concentrations but not at 100 cells/µL, with significant differences between cell densities at all time points, excluded day13, where the difference between 300 cells/µL and 600 cells/µL samples was not significant. Therefore, the concentration of 300 cells/µL was chosen as optimal cell density to perform the next set of experiments, and this in order to minimize the cell number needed for each sample but also to maintain a good cell proliferation level.

A)

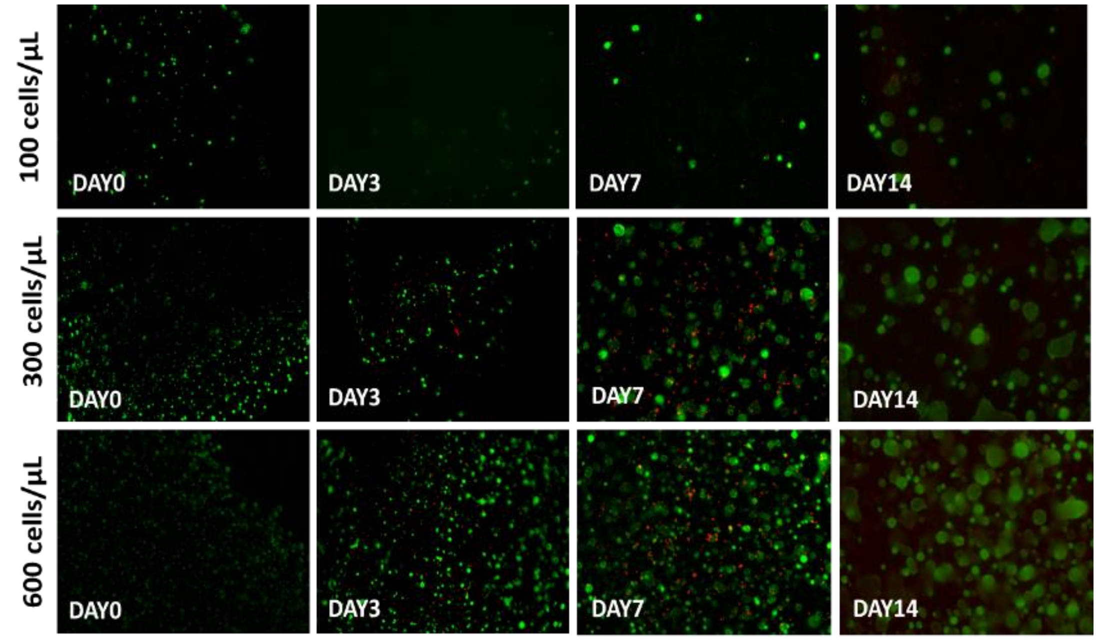

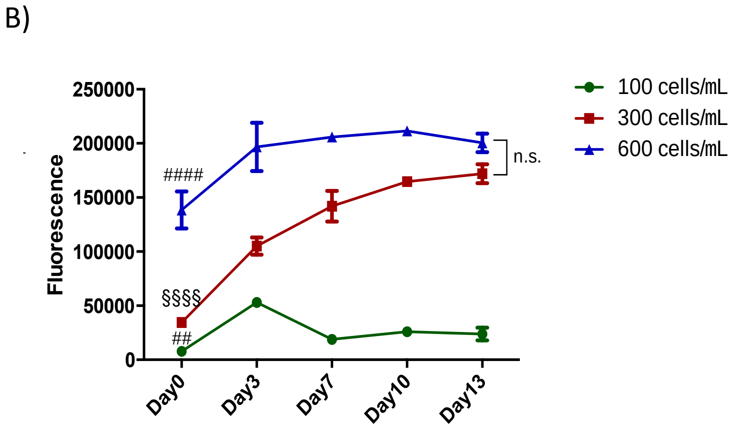

Figure 34: Viability of LX2 cells in HepGel. *A) Live Dead assay on different densities of LX2 cells seeded in HepGel. LX2 cells were seeded in HepGel at 100 cells/µL – 300 cells/µL – 600 cells/µL and cultured up to 14 days. Live Dead staining was performed on day0, day3, day7, and day 14. (n=1 for each cell density/time point). B) PrestoBlue assay on different densities of LX2 cells seeded in HepGel. LX2 cells were seeded in HepGel at 100cells/µL – 300 cells/µL – 600 cells/µL and cultured up to 14 days. PrestoBlue assay was performed on day0, day3, day7, day 10 and day13. (##P<0.01/0.001 100cells/µL vs 300 cells/µL and 600 cells/µL, constant for all the time points; §§§§P<0.001 300 cells/ µL vs 600 cells/µL, constant for all the time points. n=3 for each cell density).*

4.3.1.2 LX2 cultured in HepGel respond to pro-fibrogenic stimuli: gene and protein expression analysis.

In order to assess if LX2 cells cultured in HepGel were responsive to well-known profibrogenic stimuli, cells were treated after 7 days of culture with TGFB1 (5 ng/mL) for 2x 48 hours to recreate a pro-fibrogenic microenvironment. After 11 days of culture, samples were analysed for gene and protein expression of known fibrosis and HSCs activation biomarkers. Messenger RNA of COL1A1, COL3A1, ACTA2 and LOX were investigated. TGFB1 treatment induced a significant upregulation in COL1A1, COL3A1 and LOX in comparison to non-treated cells, whereas no effect was found on ACTA2 gene expression. Moreover, a significant increase in the secretion of proCOL1A1 protein was detected after TGFB1 treatment in comparison to non-treated cells (Figure 35).

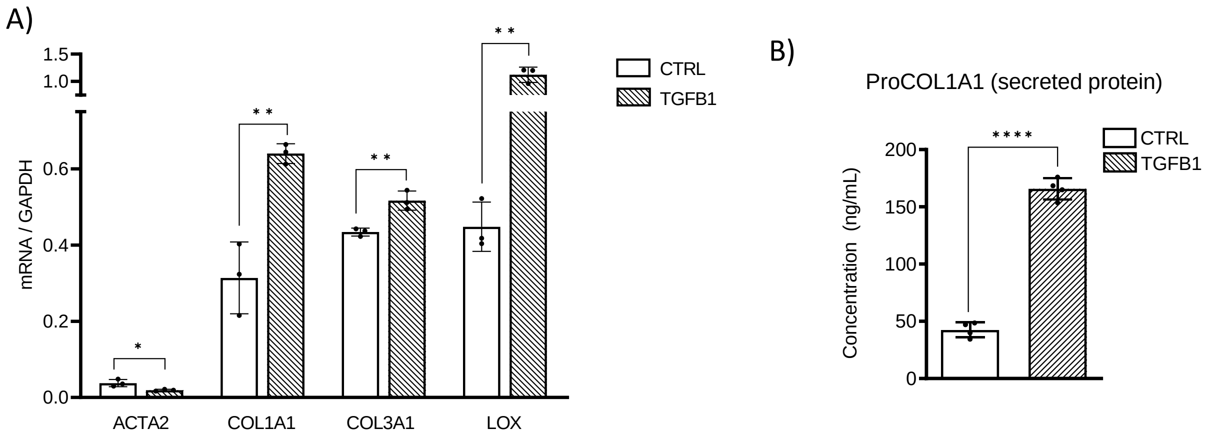

Figure 35: Gene and protein expression analysis of LX2 cells cultured in HepGel and treated with TGFB1. *LX2 cells (300 cells/ µL) were cultured in HepGel for 7 days and treated with TGFB1 (5 ng/mL) for 2x 48 hours. RNA was isolated and qPCR performed. Supernatants were collected and analysed with ELISA for the presence of proCOL1A1. A) ACTA2, COL1A1, COL3A1, and LOX gene expression, B) proCOL1A1 protein expression/secretion. (*/**/**** P<0.05/0.01/0.001, n=4 HepGel for each condition; gene expression was normalized to GAPDH. Data are expressed as mean ± SD).*

4.3.1.3 LX2 cultured in HepGel response to pro-fibrogenic stimuli: contraction

In order to understand whether HSCs cultured in HepGel could be a good model to evaluate HSCs contraction, immunofluorescence analysis was performed on both TGFB1-treated and non-treated samples. Cells were stained for F-actin with TRICT-Phalloidin and nuclei stained with Hoechst 33258. As shown in Figure 36, cells formed spheroids that eventually repopulated the whole HepGel, and a decrease in size was observed in the TGFB1-treated sample. This is probably due to the ECM deposition, cross-linking of ECM and the cellular cytoskeletal tension with which HSCs are characterized as shown in Figure 36.

The same set of experiments was then repeated using primary HSC, in order to confirm that HepGel also can support the maintenance and proliferation of primary cells.

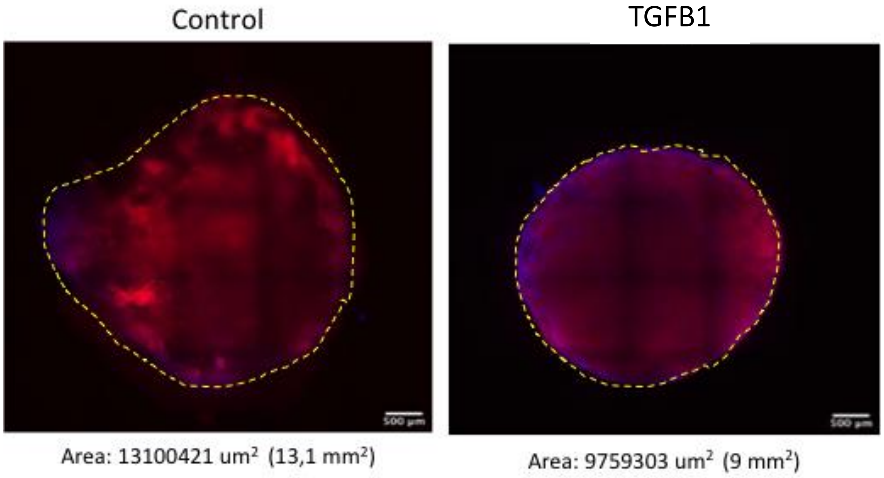

Control

TGFB1

Area: 13100421 um² (13,1 mm²)

Area: 9759303 um² (9 mm²)

Figure 36: Immunofluorescence staining of LX2 cells cultured on HepGel and treated with TGFB1. *LX2 (300 cells/ µL) were cultured on HepGel for 7 days and treated with TGFB1 (5 ng/mL) for 48h*2. Immunofluorescence staining was performed for F-actin (red) and nuclei were counterstained with Hoechst 32258 (blue). (N=1)*

4.3.1.4 Assessment of HSC viability and proliferation in HepGel.

Three different concentrations of HSCs (300 cells/µL – 600 cells/µL – 1200 cells/µL) were seeded in HepGel for 11 days. Cell viability was evaluated every 3 days from day 0 to day 11 using PrestoBlue assay and Live/Dead assay.

HSC cells were viable in the HepGel at both 600 cell/µL and 1200 cell/µL concentrations, with cells forming spheroids of increasing size detected at day 7 (Figure 37). This trend was not observed at 300 cells/µL concentration.

Since there was a significant difference in cell number at day11, 1200 cells/µL as cell density/concentration was chosen to perform the next set of experiments.

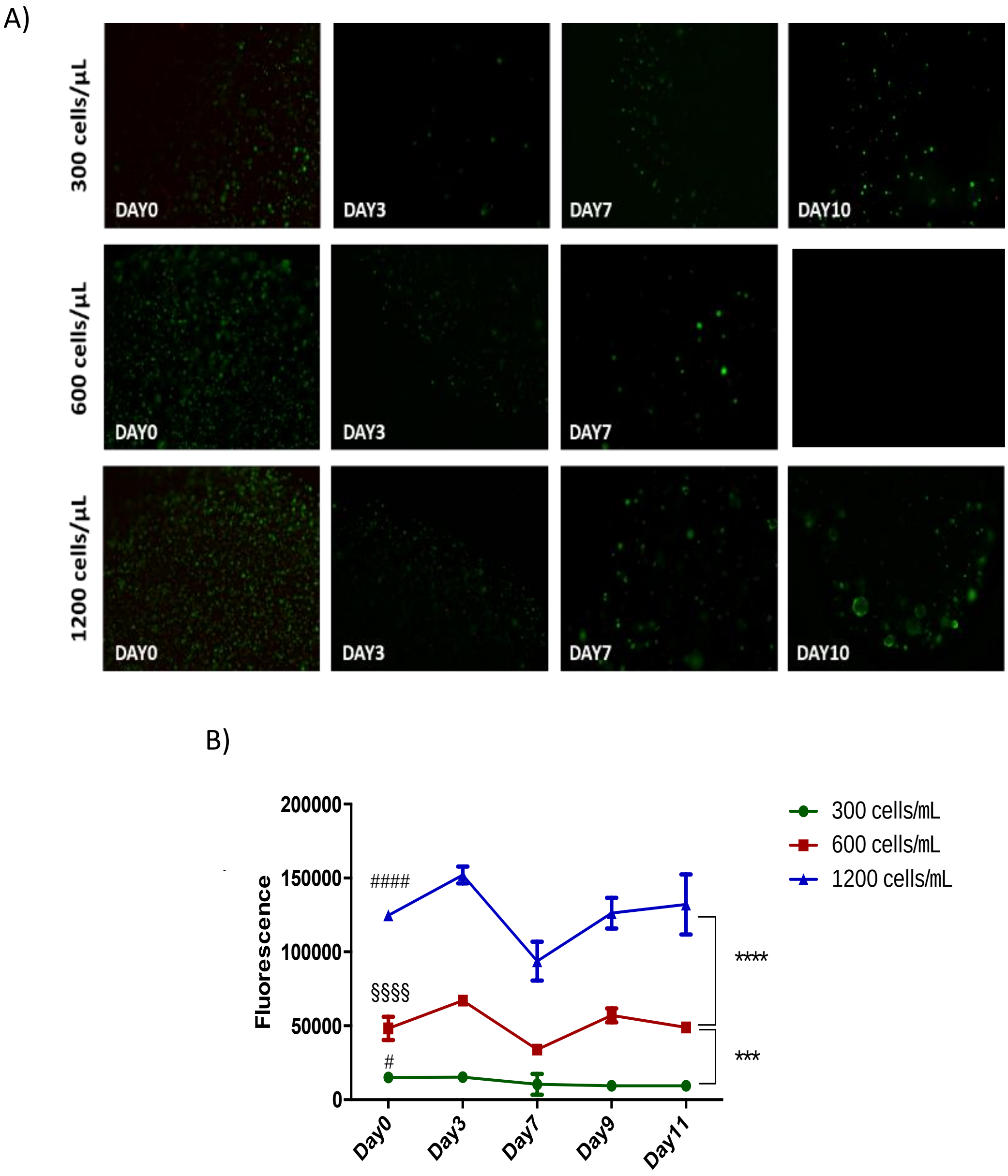

Figure 37: Viability of primary HSCs in HepGel. *A) Live Dead assay on different densities of primary HSCs cells seeded in HepGel. Primary HSCs were seeded in HepGel at 300 cells/uL – 600 cells/uL – 1200 cells/uL and cultured up to 11 days. Live Dead staining was performed on day0, day3, day7 and day 10. (n=1 for each cell density/time point); B) PrestoBlue assay on different densities of primary HSCs seeded in HepGel. PrestoBlue was performed on day0, day3, day7 and day 10. (n=3 HepGel samples for each cell density, #/####P<0.05/0.001 300cells/ul vs 600 cells/ul or 1200 cells/ul, constant at all time points, §§§§P<0.001 600 cells/ul vs 1200 cells/ul – constant at all time points, ***P<0.005 300cells/ul vs 600 cells/ul at day11, ****P<0.001 600cells/ul vs 1200 cells/ul at day11).*

4.3.1.5 HSC cultured in HepGel respond to pro-fibrogenic stimuli: gene and protein expression analysis.

In order to assess if HSC cells cultured in HepGel were responsive to well-known profibrogenic stimuli, HSCs at a density of 1200 cells/µL were seeded in HepGel. After 7 days of culture, cells were treated with TGFB1 (5 ng/mL) for 2x 48 hours. After 11 days of culture, samples were analysed for gene expression and protein expression. Messenger RNA of COL1A1, COL3A1, ACTA2, CYGB and LOX was investigated. As shown in Figure 38, TGFB1 treatment induced a significant upregulation in COL1A1, ACTA2 and LOX mRNA expression in comparison to non-treated cells, whereas no significant changes were found in COL3A1 and CYGB gene expression (Figure 38). The activation of HSC was further investigated by analysing the proCOL1A1 protein secretion in the culture medium by employing ELISA and showed to be significant upregulated in primary HSC treated with TGFB1 (Figure 38).

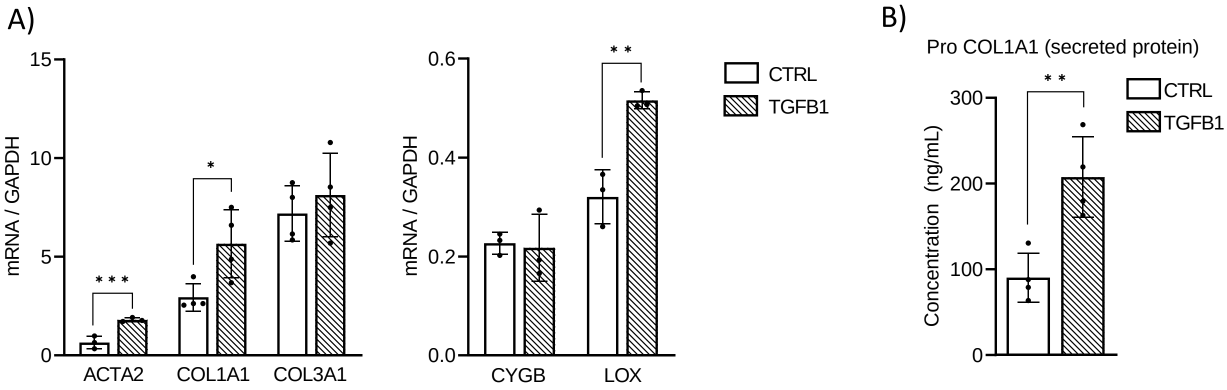

Figure 38: Gene and protein expression analysis of primary HSCs cultured in HepGel and treated with TGFB1. *Primary HSCs (1200 cells/ uL) were cultured in HepGel for 7 days and treated with TGFB1 (5 ng/mL) for 2x48 hours. RNA was isolated and qPCR performed. Supernatants were collected and analysed for the presence of proCOL1A1. A) ACTA2, COL1A1, COL3A1, CYGB, LOX gene expression; B) proCOL1A1 protein secretion. (*/**/***P<0.05/0.01/0.005 vs non-treated cells, n=4). Gene expression was normalized to GAPDH. Data are expressed as mean ± SD.*

In parallel, HSC were cultured on 2D plastic dishes following the same experimental set up, and this in order to compare HSC activation between 2D and 3D culture. As shown in Figure 39, a significant upregulation of mRNA expression of ACTA2, COL1A1 and LOX gene expression was observed in 2D cultured HSC compared to HSC cultured in HepGel. These data indicate that when using the human liver ECM as substrate in the HepGel, HSCs are less activated compared to when cultured in 2D.

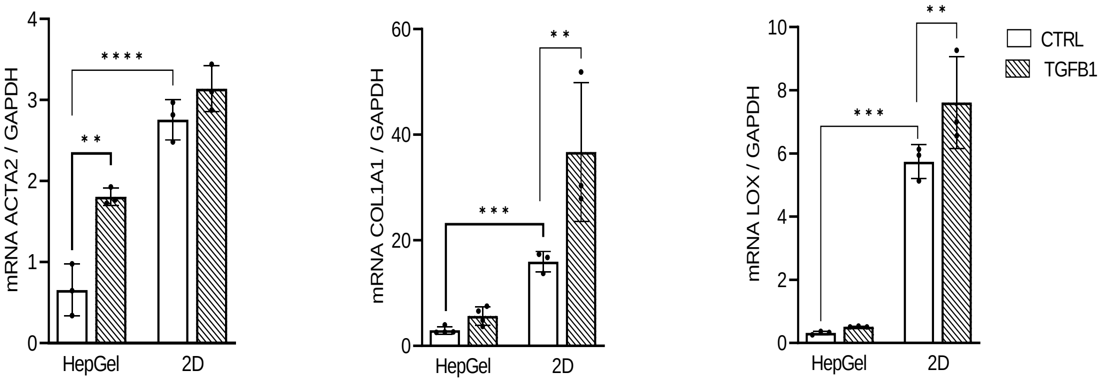

Figure 39: Gene expression analysis of primary HSCs cells cultured in HepGel or 2D and treated with TGFB1. *Primary HSCs cells (1200 cells/ uL) were cultured on HepGel or 2D plastic dishes for 7 days and treated with TGFB1 (5 ng/mL) for 2x48 hours. RNA was isolated and qPCR performed. Gene expression of ACTA2, LOX and COL1A1 (*/**/***/****P<0.05/0.01/0.005/0.001, n=4). Gene expression was normalized to GAPDH. Data are expressed as mean ± SD.*

4.3.1.6 HSCs cultured in HepGel response to pro-fibrogenic stimuli: contraction

In order to understand if HSCs cultured in HepGel could be a valuable new model to evaluate HSC contraction, immunofluorescence analysis was performed on one untreated sample and one sample treated with TGFB1 (5 ng/mL) for 2x 48 hours. Cells were stained for F-actin with TRICT-Phalloidin and nuclei with Hoechst 33258.

Cells grown in HepGel formed spheroids of different dimensions, their size was measured with the CQ1 Yokogawa analysis software and a significant decrease was observed when cells were exposed to TGFB1. This is probably due to the new ECM deposition which induces cytoskeletal tension (Figure 40).

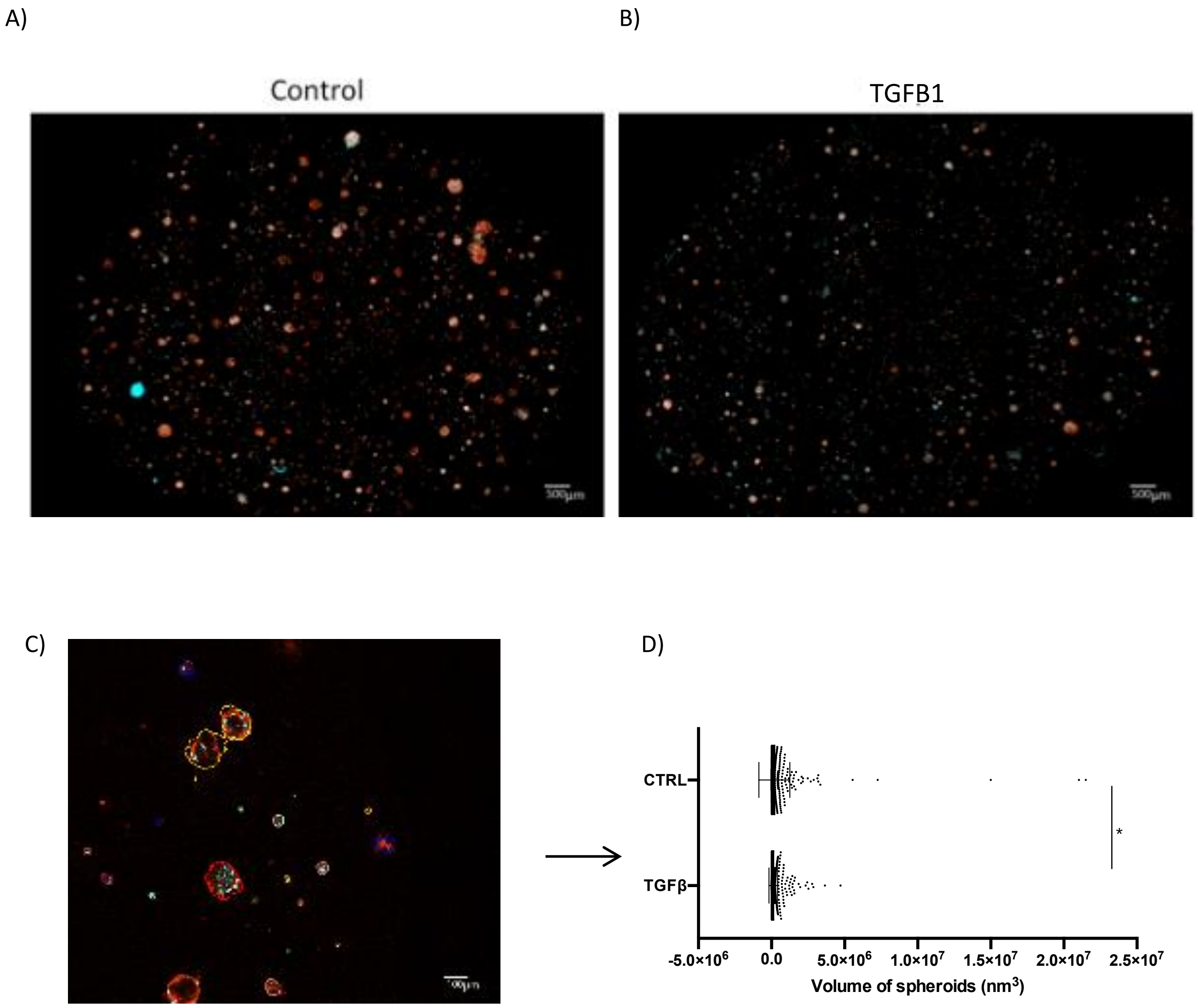

Figure 40: Immunofluorescence staining of primary HSCs cultured on HepGel and treated with TGFB1. *Primary HSCs (1200 cells/ uL) were cultured in HepGel for 7 days and treated with TGFB1 (5 ng/mL) for 2X 48 hours. Immunofluorescence staining was performed for F-actin (red) and nuclei were counterstained with Hoechst 32258 (blue). A) Picture of whole untreated HepGel (6x5 pictures stitched at 10x magnification); B) Picture of whole TGFB1-treated HepGel (6x5 pictures stitched at 10x magnification). C) Single 10x magnification picture with spheroid recognition by CQ1 analysis software. D) Graphical representation of spheroids volume in untreated and TGFB1-treated HepGel samples. (The number of spheroids for each sample was counted and the volume of every spheroid was quantified with CQ1 software). (*P<0.05, N=1)*

In 2019 the thermo-responsive PGMA-PHPMA diblock copolymer gelling reagent could not be produced anymore, hence experimental testing of HepGel had to stop and alternative gelling agents were sought. Based on previous results obtained in our laboratory[171], the commercially available CELLINK Bioink, a biomaterial composed of alginate and cellulose nanofibrils, was chosen to perform the following experiments.

4.3.2 Nanocellulose-based human liver extracellular matrix three-dimensional hydrogels (ECM Gels) for modelling liver fibrosis and evaluating HSCs contraction.

The experiments exposed in this subchapter were performed using both healthy and cirrhotic extracellular matrix solution derived from decellularized human healthy and cirrhotic livers.

4.3.2.1 Characterization of the mechanical properties of ECM Gels.

Rheological properties of ECM Gels were evaluated using Dynamic Mechanical Analysis (DMA). Specifically, storage modulus (E') and loss modulus (E") were measured in ECM Gels containing or not either healthy or cirrhotic ECM or composed of solely nanocellulose (Table 9) using a Time Sweep Test (Figure 41). E' and E" were stable throughout the test in all the ECM Gels composition tested, thus indicating a stable crosslinked status. Furthermore, in all the samples E" was 10-fold lower than E', suggesting a solid-like behaviour of the material which is typical of stable crosslinked hydrogels[175].

ECM Gel type	Composition
Healthy ECM Gel	45% healthy ECM solution + 30% Nanocellulose + 25% HBSS
Cirrhotic ECM Gel	45% cirrhotic ECM solution + 30% Nanocellulose + 25% HBSS
Mock ECM Gel	45% cirrhotic ECM solution (solvent only) + 30% Nanocellulose + 25% HBSS
Nanocellulose only Gel	75% Nanocellulose + 25% HBSS

Table 9. ECM Gel composition.

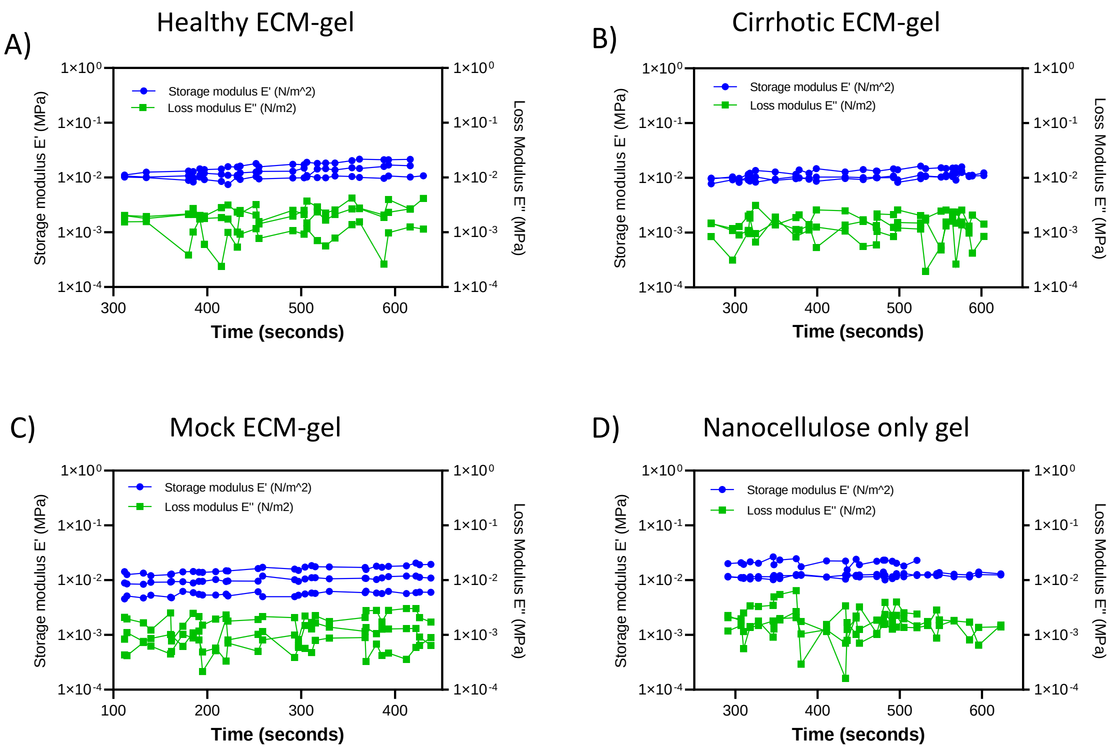

__Figure 41: Mechanical properties of ECM Gels: E' an E''.__ Storage and Loss Modulus of A) healthy ECM-gel, B) cirrhotic ECM-gel, C) mock ECM-gel and D) Nanocellulose only gel measured by time sweep for 6 minutes at 37C. (n=3 per each ECM-gel condition).

Stiffness of the ECM Gels was expressed as Young's modulus and measured using a Stress-Strain Test. Healthy, cirrhotic or mock ECM Gels showed no difference in stiffness, while they all presented with significantly lower stiffness than the gel composed of only nanocellulose (Figure 42).

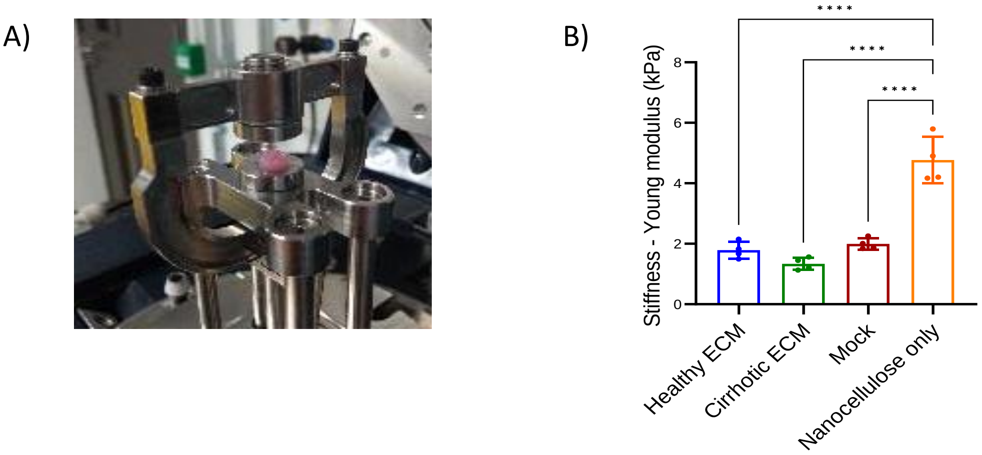

__Figure 42: Mechanical properties of ECM Gels: Young's modulus.__ A) Representative image of DMA measurement of ECM-gels; B) Young's modulus of healthy ECM-gel, cirrhotic ECM-gel, mock ECM-gel and nanocellulose only-gel measured by stress-strain ramp at 37°C. (n=3 per each ECM-gel condition).

The microarchitecture of ECM Gels was evaluated by Scanning Electron Microscopy (SEM). A regular porosity was observed for all the ECM Gel compositions, with pores having a more structured organization in the Nanocellulose-only gels. Importantly, small and reticulated ECM fibres could be seen in the healthy and cirrhotic ECM Gels, while their presence was not detected in the mock-ECM gels or nanocellulose-only gels (Figure 43).

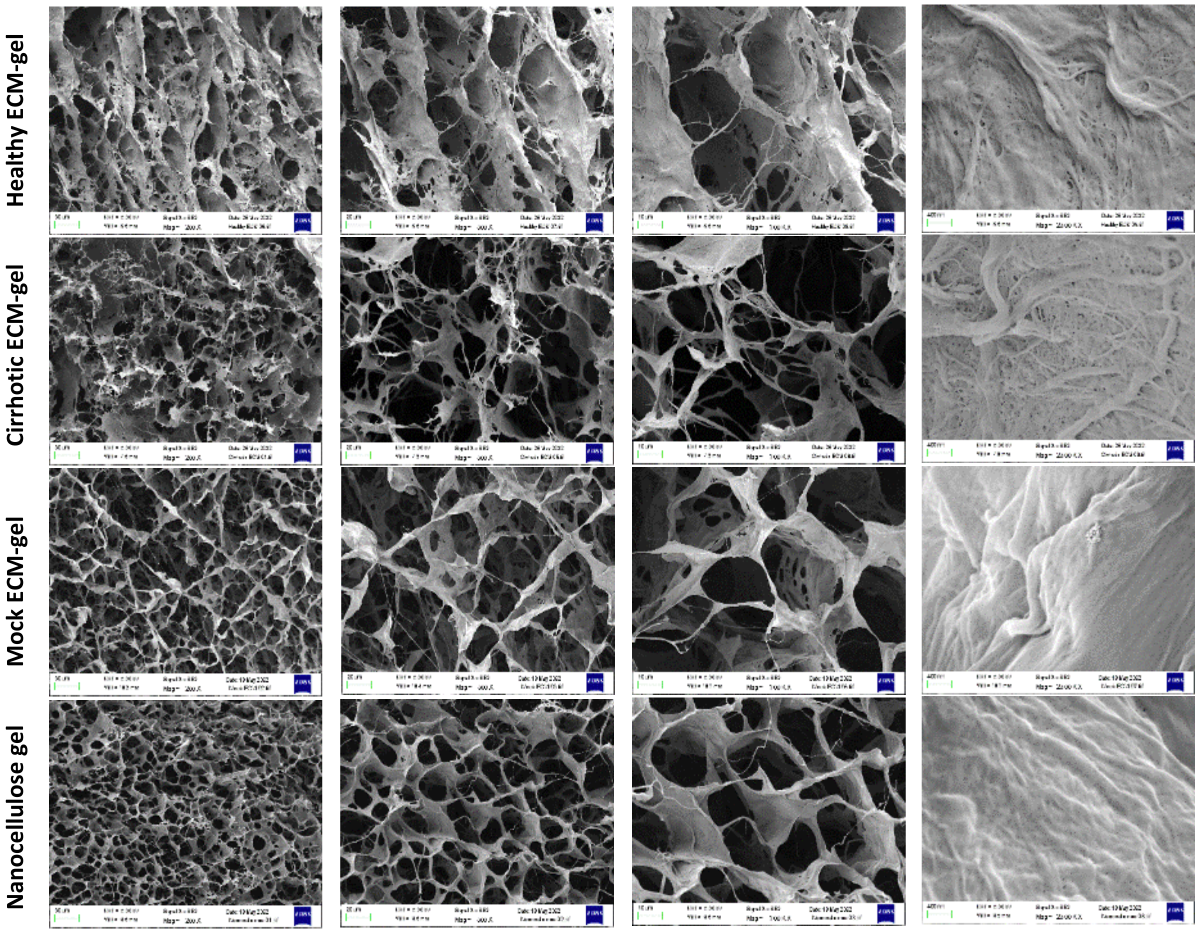

Figure 43: Mechanical properties of ECM Gels. *Scanning Electron Microscopy representative images of healthy ECM Gels, cirrhotic-ECM gels, mock-ECM gels and Nanocellulose only gels(N=1 per condition; from left to right: 50 μM, 20 μM, 10 μM, 400 nM scale bar) .*

4.3.2.2 Assessment of HSCs cell density and viability in ECM Gels.

Based on previous experiments (L. Frenguelli et al., unpublished), two different concentrations of HSCs (3000 cells/µL or 5000 cells/µL) were seeded in healthy ECM Gels and cultured for 14 days. Cell viability was evaluated at day 0, day 3, day 7 and day14.

As shown in Figure 44, HSCs remained viable and metabolically active throughout the culturing period, without showing a significant increase in cell numbers (Figure 44C). Cells developed a spindle-like phenotype from day7 onwards (Figure 44B). As there was no significant difference in metabolic activity or viability between the two cell densities tested, the concentration of 5000 cells/µL was chosen to perform the next set of experiments, and this in order to maximize the quantity of RNA or protein material extracted from each sample but also to maintain a good cell viability level.

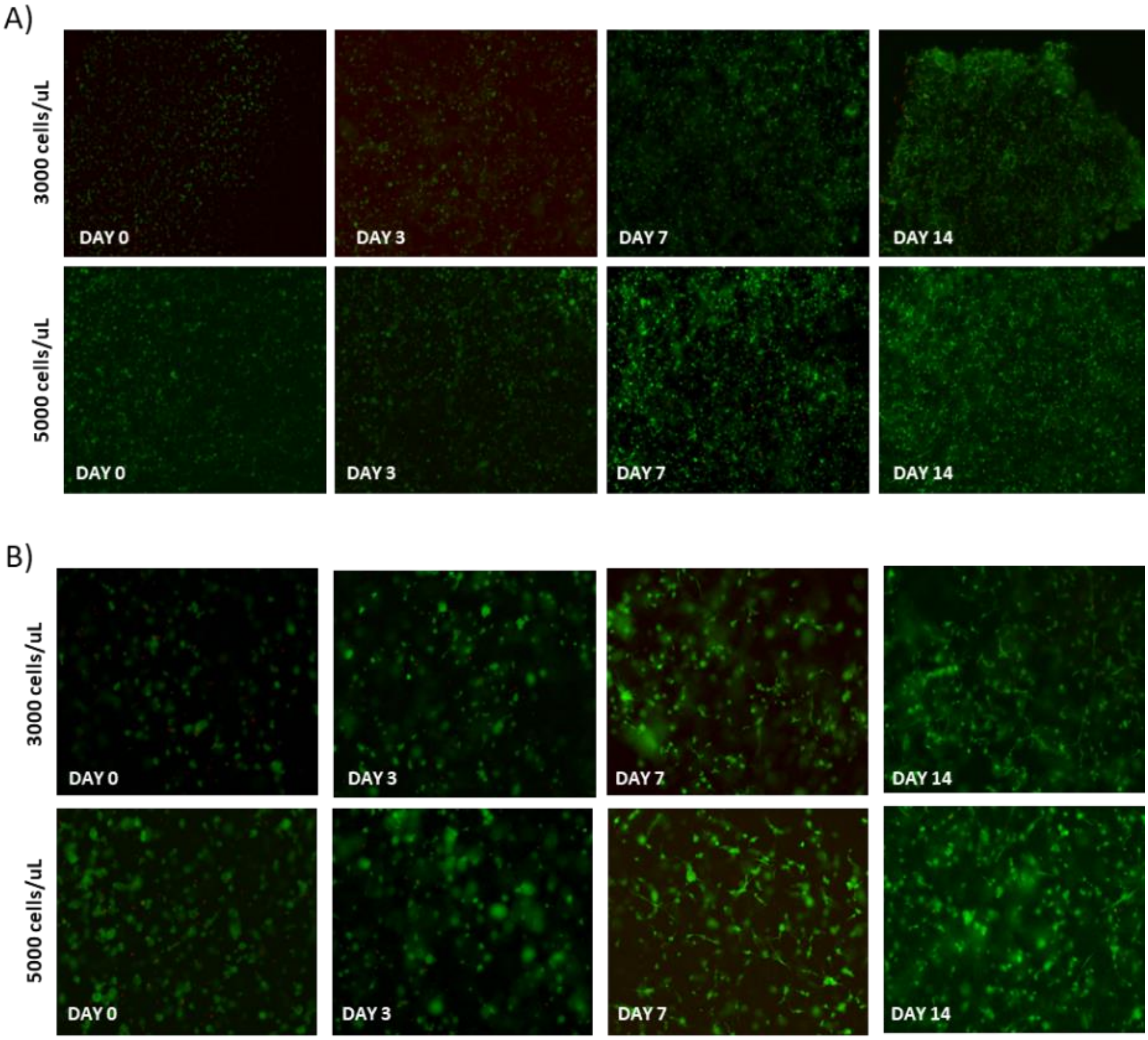

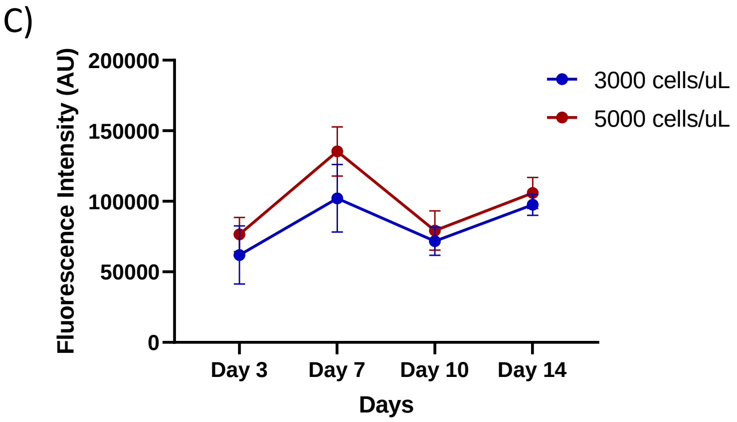

Figure 44: Evaluation of viability and proliferation of HSCs cultured in healthy ECM Gels. *HSCs were seeded in healthy ECM Gels at 3000 cells/uL or 5000 cells/uL and cultured up to 14 days; A-B) Live Dead assay on different densities of HSCs seeded in healthy ECM Gel. Live Dead staining was performed on day0, day3, day7 and day 14, and pictures taken at A) 4x magnification or B) 10x magnification; (n=1 for each cell density/time point); C) PrestoBlue assay on different densities of HSCs seeded in healthy ECM-gel. PrestoBlue assay was performed on day3, day7, day 10 and day14 (n=3 for each cell density).*

Before proceeding with further experiments, the same investigation was performed on HSCs seeded at a concentration of 5000 cells/µL in cirrhotic ECM Gels and cultured for 14 days. HSCs remained viable and metabolically active throughout the culturing period, without a significant increase in cell numbers (Figure 45, data kindly provided by Dr. Philipp Schwabl), and hence behaving in a similar way as in the healthy ECM Gels.

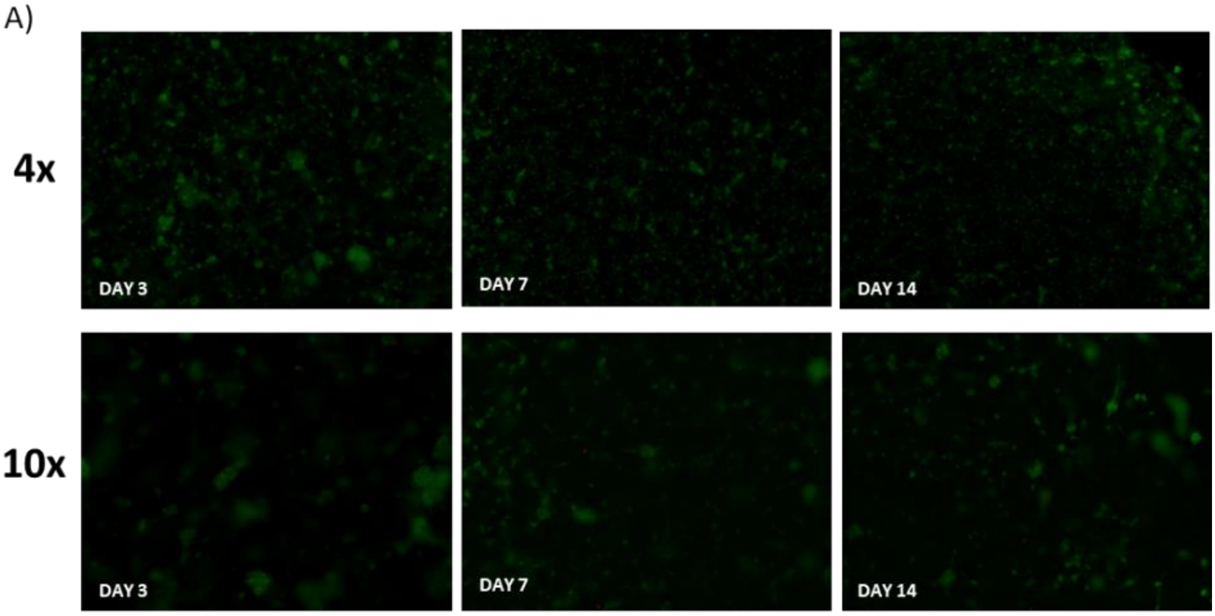

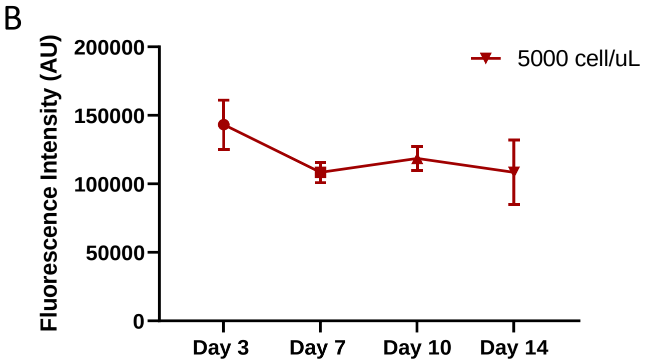

Figure 45: Evaluation of viability and proliferation of HSCs cultured in cirrhotic ECM Gels. *HSCs were seeded in cirrhotic ECM Gels at 5000 cells/uL and cultured up to 14 days; A) Live Dead assay on HSCs seeded in healthy ECM Gels. Live Dead staining was performed on day0, day3, day7 and day 14, pictures taken at 4x or 10x magnification; (n=1 for each cell density/time point); B) PrestoBlue assay on HSCs seeded in healthy ECM Gels. PrestoBlue assay was performed on day3, day7, day 10 and day14 (n=3 for each cell density).*

4.3.2.3 HSCs cultured in ECM Gels respond to pro-fibrogenic stimuli: gene expression analysis.

Responsiveness of HSCs cultured in healthy or cirrhotic ECM Gels to standard pro-fibrogenic stimuli was tested using TGFB1. As shown in figure 46, the treatment induced a significant increase in the gene expression of classical HSC activation markers (TGFB1 and TIMP1) when cells were cultured in both healthy and cirrhotic ECM Gels. COL1A1 expression was significantly upregulated by TGFB1 only when HSCs were cultured on healthy ECM Gels, while the treatment had no effect on ACTA2 gene expression. Importantly, the quiescence marker CYGB was downregulated by TGFB1 treatment in cells cultured in both healthy and cirrhotic ECM Gels, while IL6 followed a similar trend only in healthy-ECM cultured cells (Figure 46). Overall, these data show a good response of HSCs cultured in ECM Gels to exogenous stimuli.

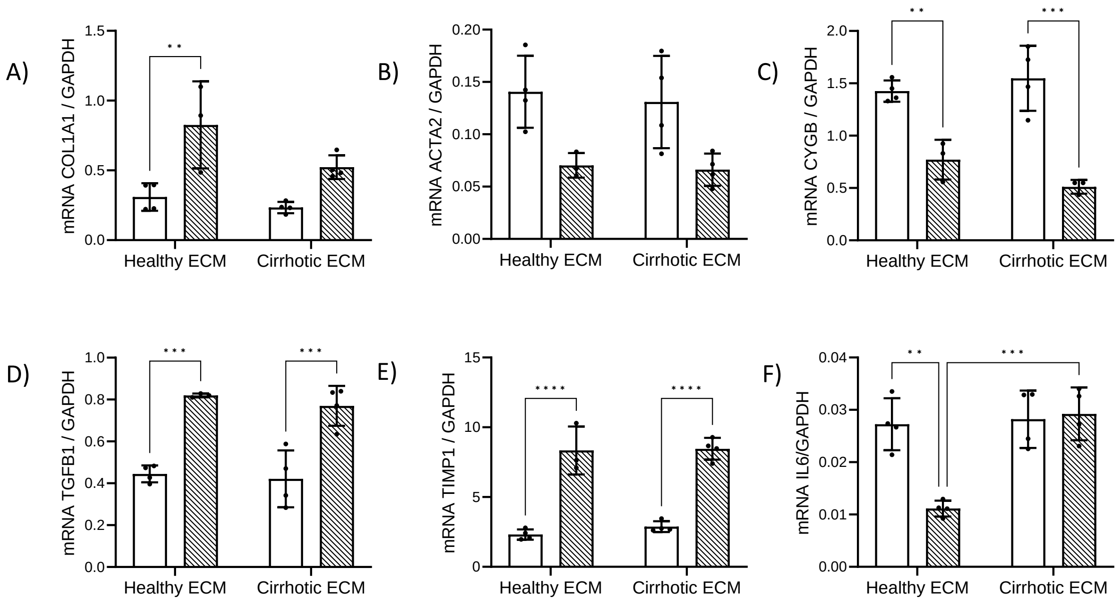

Figure 46: Responsiveness to TGFB1 treatment of HSCs cultured in healthy or cirrhotic ECM Gels. *(A – F) Gene expression analysis of HSCs activation markers COL1A1 (A), ACTA2 (B), TGFB1 (D), TIMP1 (E), quiescence marker CYGB (C) and proinflammatory marker IL6 (F). HSCs were cultured on healthy and cirrhotic ECM Gels for 14 days and treated with TGFB1 for 48h*3 starting at day 7. (****/***/**p<0.001/0.005/0.01; n=4 for each group).*

4.3.2.4 Comparison of HSCs behaviour when cultured in ECM Gels, ECM-scaffolds or 2D.

In order to unravel similarities and differences between the two three-dimensional models presented in this work and classical 2D cultures, HSCs were cultured in parallel in healthy and cirrhotic ECM Gels, healthy and cirrhotic ECM-scaffolds (all derived from the same healthy or cirrhotic human livers) or on plastic. As shown in Figure 47, gene expression analysis shows a very similar trend between ECM Gels and scaffolds for activation markers COL1A1 and ACTA2, significantly downregulated in HSCs cultured in healthy and cirrhotic ECM Gels or scaffolds compared to cells cultured in 2D. Quiescence marker CYGB was more expressed in HSCs cultured in ECM Gels compared to scaffolds, but cells in both ECM Gels and scaffolds showed a significant upregulation when compared with cell cultured in 2D. A similar trend was observed for TGFB1. TIMP1 gene expression was upregulated only in cirrhotic ECM Gels compared to cirrhotic scaffolds and 2D, with IL6 gene expression having a similar direction (Figure 47).

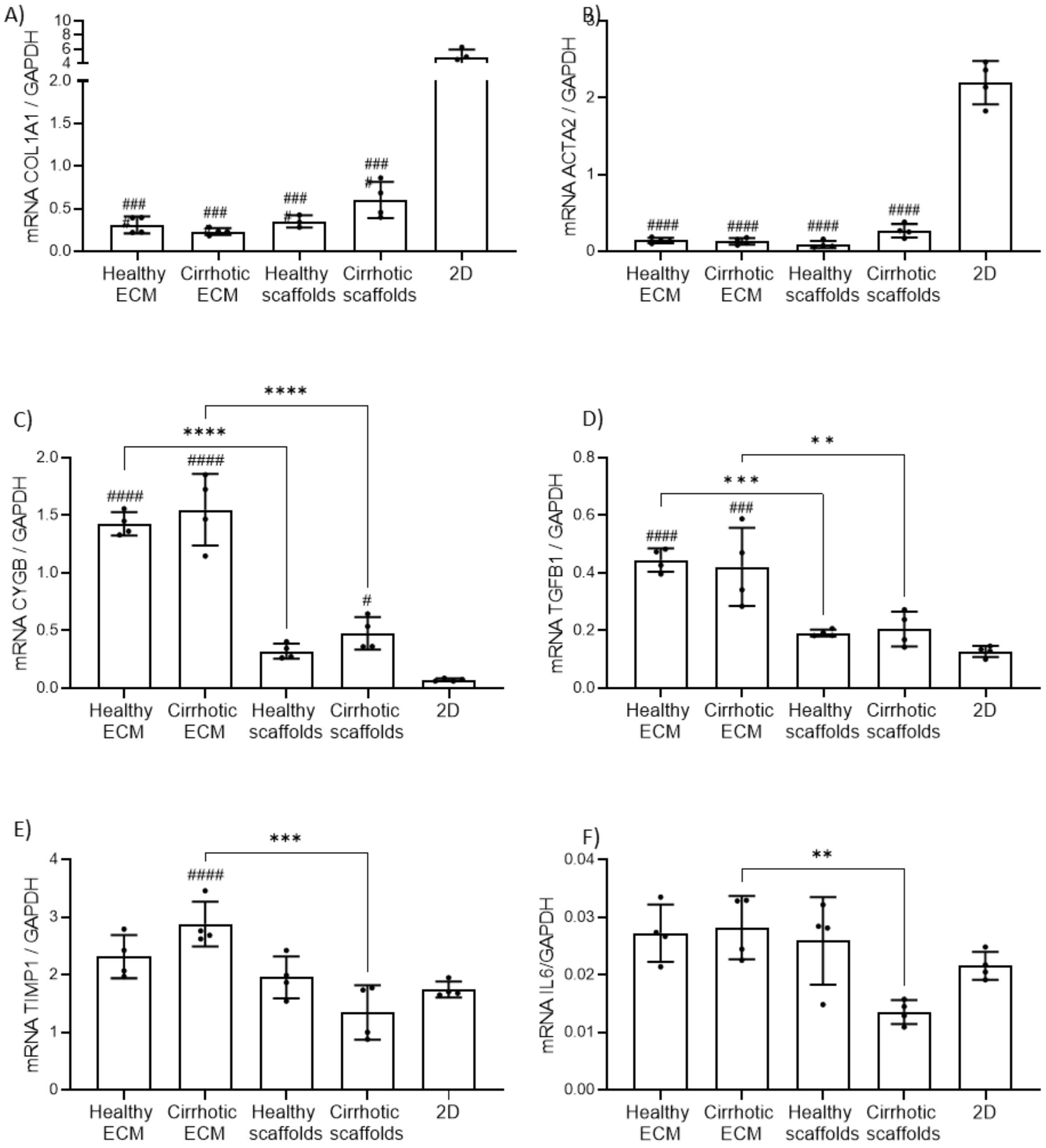

Figure 47: Comparison of HSCs behaviour in healthy or cirrhotic ECM Gels, ECM scaffolds or 2D culture. *(A – F) Gene expression analysis of HSCs activation markers COL1A1 (A), ACTA2 (B), TGFB1 (D), TIMP1 (E), quiescence marker CYGB (C) and proinflammatory marker IL6 (F). HSCs were cultured on healthy and cirrhotic ECM Gels or scaffolds for 14 days or in 2D for 3 days. (****/***/**p<0.001/0.005/0.01 ECM Gels vs scaffolds; ####/###p<0.001/0.005 ECM Gels or scaffolds vs 2D; n=4 for each group).*

Overall, although some slight differences can be observed between HSCs cultured in ECM Gels and ECM-scaffolds, they show a similar behaviour where they are less activated compared to classical 2D cultures. Importantly though, ECM scaffolds and ECM Gels presented with some different features, as shown in Figure 48. In fact, the distribution of HSCs cultured in ECM Gels was much more homogenous than when HSCs were cultured in ECM scaffolds. Furthermore, the quantity of human tissue needed to produce the same number of HSCs samples was much lower and less perishable when utilizing ECM Gels compared to ECM scaffolds (Figure 48).

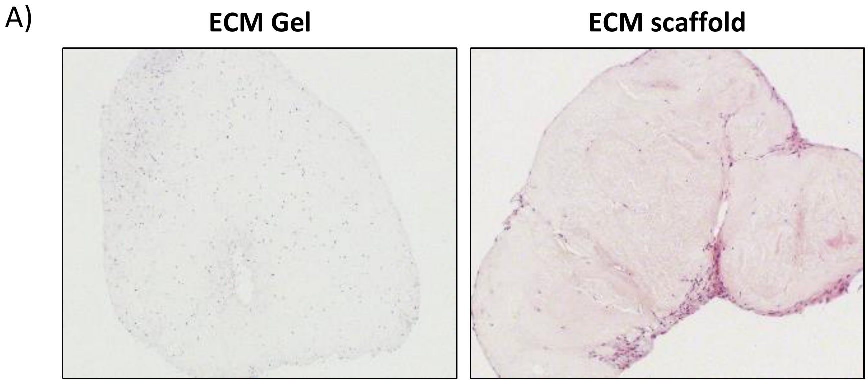

B)

3D in vitro model	#decellularized scaffolds	mL of ECM solution	#HSC culture samples	Shelf life
ECM scaffolds	10	/	10	1 month (4C)
ECM Gels	10	2.3 mL	~100	3 months (4C)

Figure 48: Comparison of the 3D ECM Gels versus ECM scaffolds model. *(A) H&E staining of HSCs cultured for 14 days on ECM Gels or ECM scaffolds (10x magnification); (B) Table comparing quantity of liver ECM scaffolds needed to culture HSCs in ECM Gels or ECM scaffolds and relative shelf-life.*

4.3.2.5 Cultures in ECM Gels can be used to investigated genetic variants in HSCs.

To prove whether ECM Gels, as well as ECM scaffolds, could be used to investigate the impact of genetic variants on HSCs, as shown in Chapter 3 of this thesis, cells being WT (from now on referred as WT) or heterozygous for both the PNPLA3 I148M and the TM6SF2 E156K variant (from now on referred as HET-MUT) were cultured in healthy or cirrhotic ECM Gels and their activation status analysed.

As shown in Figure 49, HET-MUT HSCs had a significantly increased gene expression of ACTA2 compared to WT HSCs only when cultured on cirrhotic ECM Gels and in presence of TGFB1. COL1A1 was upregulated in HET-MUT HSCs cultured in healthy ECM Gels in presence of TGFB1 and in cirrhotic ECM Gels without TGFB1 treatment. TGFB1 followed a different trend, being downregulated in HET-MUT HSCs compared to WT in both healthy and cirrhotic ECM Gels treated with TGFB1. TIMP1 gene expression was upregulated in HET-MUT HSCs compared to WT cultured in cirrhotic ECM Gels but downregulated in presence of the TGFB1 treatment. Importantly, TGFB1 treatment upregulated TGFB1 and TIMP1 gene expression only in WT HSCs cultured on healthy and cirrhotic ECM Gels.

This indicates a stronger activation of HET-MUT HSCs when cultured in the cirrhotic ECM Gels, but a lower responsiveness to TGFB1 treatment.

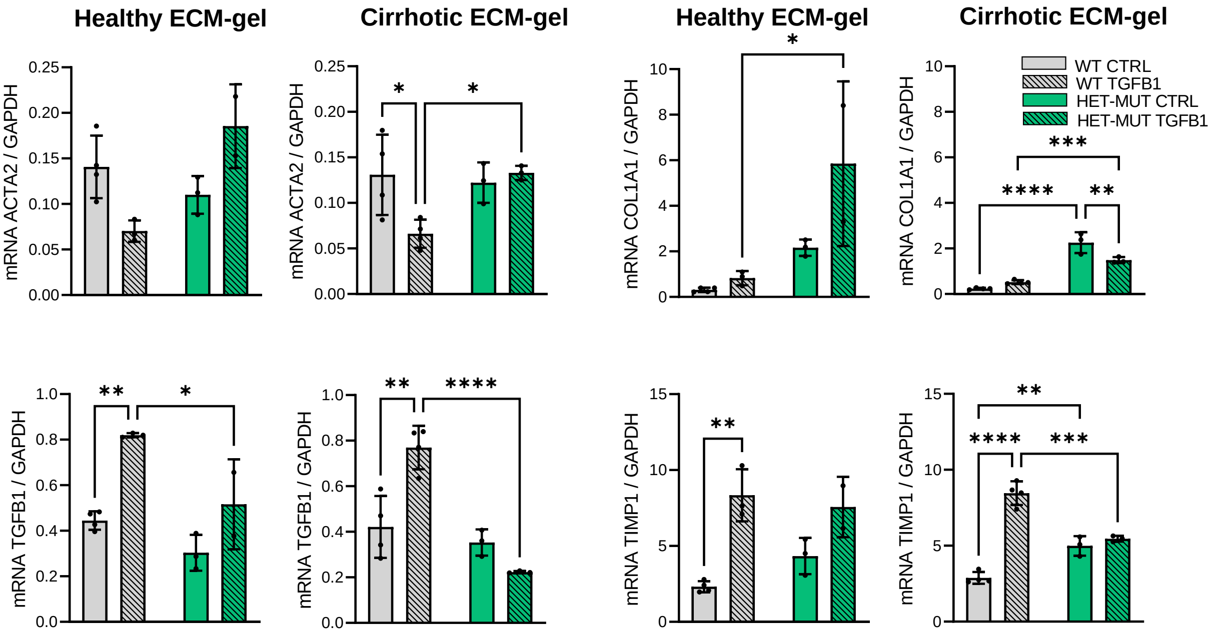

*__Figure 49: Comparison of WT or HET-MUT HSCs behaviour in healthy or cirrhotic ECM Gels.__ Gene expression analysis of HSCs activation markers ACTA2, COL1A1, TGFB1, TIMP1. HSCs were cultured on healthy and cirrhotic ECM-gels for 14 days and treated with TGFB1 (5ng/mL) for 48*3hours. (****/***/**/*p<0.001/0.005/0.01/0.05; n=2/4 for each group).*

4.3.2.6 Cultures in ECM Gels to evaluate HSCs contraction.

Since HSCs in ECM Gels did not form spheroids as they did in HepGels (Figure 40), a novel methodology to evaluate contraction was optimized in the laboratory by Dr

Philipp Schwabl. Contraction of the whole ECM Gel was evaluated by quantifying the total area of the ECM Gel from a 1x picture and then the Area Change at different time points of the investigation expressed as a percentage.

Contraction was induced in WT or HET-MUT HSCs cultured in healthy ECM Gels by utilizing the vasoconstrictor Endothelin-1 (1uM) after pre-treating with TGFB1 (5ng/mL) for 48h*3 to induce HSCs activation.

As shown in Figure 50, for both WT or HET-MUT HSCs, there was no significant contraction of the ECM Gels throughout 30 minutes of Et-1 treatment, with or without TGFB1 pre-treatment. Furthermore, there was no difference in contraction between treated or control samples (Figure 50A – data on WT HSCs kindly provided by Dr Schwabl). Interestingly though, the baseline area (measured at t=0) for HET-MUT HSCs was significantly lower than for WT HSCs, indicating a possible enhanced contractility of the cells induced by the presence of the genetic variant (Figure 50B).

In fact, when looking at the protein expression and phosphorylation of Moesin, a key protein in cell contraction, its level was higher in HET-MUT compared to WT HSCs in standard conditions and increased by Et-1 treatment (Figure 51B). On contrary, the ratio of phospho-moesin/moesin was increased in WT HSCs compared to HET-MUT HSCs in standard condition, with a stronger induction by Et-1 treatment in cells with a wild type genotype (Figure 51C).

In conclusion, although the usage of nanocellulose-based ECM Gels and Et-1 does not provide a useful tool to evaluate HSCs contraction, it revealed a difference in contractility capacity of HSCs carrying the PNPLA3 I148M and TM6SF2 E156K genetic variants.

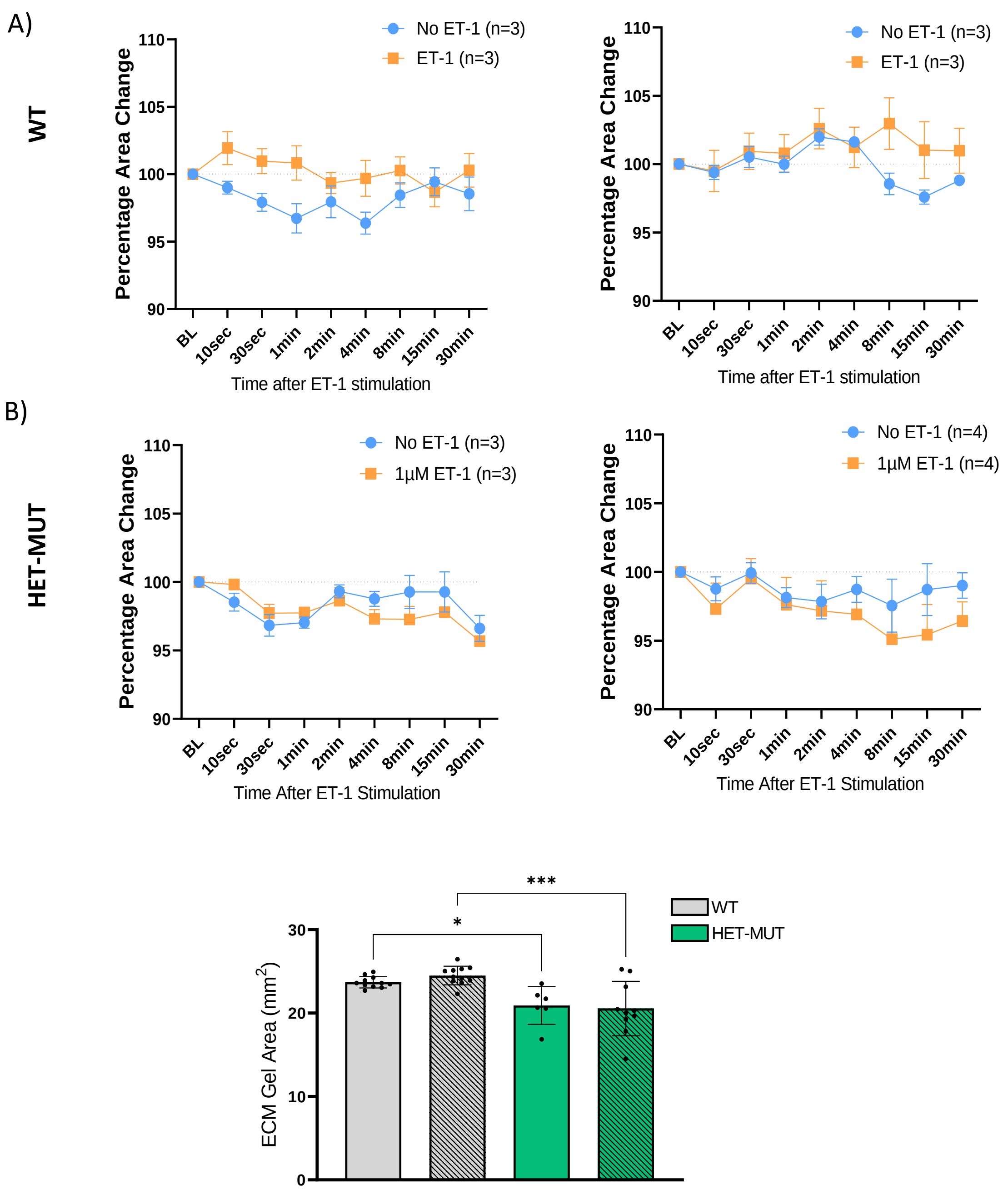

Figure 50: Contraction evaluation of HSCs WT or HET-MUT cultured in healthy ECM Gel. *HSCs WT or mutant for the PNPLA3 I148M and TM6SF2 E156K mutations (HET-MUT) were cultured in healthy ECM Gels for 14 days. At day7, samples were pre-treated with TGFB1 (5 ng/mL) for 48h*3. At day 14, samples were treated with Endothelin-1 (1uM) and contraction was tracked for a maximum of 30 minutes. (A) Percentage of Area change versus baseline control (BL, t=0) of healthy ECM Gels cultured with HSCs; measurements were taken every 10s, 30s, 1min, 2min, 4min, 8min, 15min or 30min (n=3/4 per condition); (B) Baseline control Area (t=0 – without Et-1 treatment) of HSCs TM6SF2-WT or –E156K cultured in healthy ECM-gels. (***/*p<0.005/0.05, n=6 per each condition).*

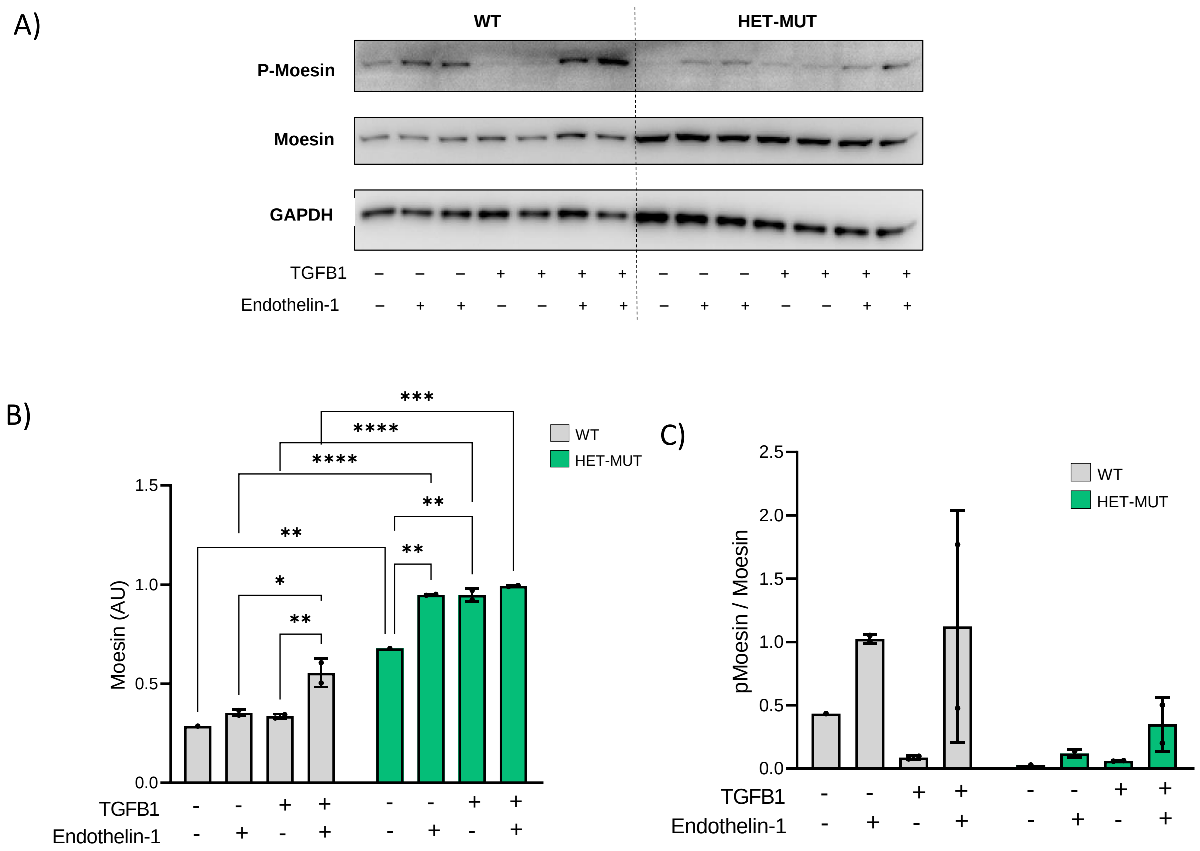

Figure 51: Protein expression of contractile proteins in HSCs WT or HET-MUT cultured in healthy ECM gels. *HSCs WT or mutant for the PNPLA3 I148M and TM6SF2 E156K mutations (HET-MUT) were cultured in healthy ECM gels for 14 days. At day7, samples were pre-treated with TGFB1 (5 ng/mL) for 48h*3. At day 14, samples were treated with Endothelin-1 (1uM) for 30 min and samples collected for protein quantification. (A) Western blot of Moesin and phospho-Moesin in HSCs cultured in healthy ECM-gels cultured with HSCs; (B) Densitometry of Moesin; (C) Ratio of phospho-Moesin/Moesin. (***/*p<0.005/0.05, n=1/2 per each condition).*

4.4 Discussion.

Among three-dimensional models for cell culture, hydrogels have been deeply investigated because of their ability to simulate the nature of most soft tissues. Indeed, they possess high water content, facilitate the transport of oxygen, nutrients, waste and soluble factors. They also give the possibility to incorporate cell adhesion ligands, tune viscoelasticity and biodegradability as well as being easily scalable[166].

Hydrogels containing single ECM components, such as basement membrane or collagen type I have been intensively used for cell culture but lack important features of the total ECM components. Using ECM derived from decellularized tissues is a good alternative but, since purified ECM proteins cannot self-reassemble, the ECM solution needs to be mixed with a synthetic gelling agent[166].

In this project, the ECM obtained from the decellularization of healthy and cirrhotic human livers[37,176] and solubilized to form healthy or cirrhotic liver ECM solutions[171] has been combined with two different gelling agents to generate hydrogels which have been used for the *in vitro* culture of hepatic cells. Specifically, experiment here discussed explored the suitability of these two types of ECM hydrogels for modelling liver fibrosis and for investigating different aspects of HSCs activation.

Due to external circumstances, cultures of HSCs in HepGels (using a thermoresponsive biopolymer as gelling agent) and ECM Gels (using an ionically crosslinked biopolymer as gelling agent) could not be tested at the same time and therefore are here not directly compared.

HSCs cultures in HepGels were first optimized by using the hepatic stellate cells line LX2. Different cell densities of LX2 cells were cultured in HepGels in order to find the best conditions for cell viability, growth and HSC concentration. HepGel was found capable to support LX2 cells viability and proliferation up to 11 days of culture and, most importantly, the cell density used to repopulate the hydrogels (300 cells/µl) was very low. This is an important aspect when scaling up the usage of this system for High Throughput Screening (HTS). Moreover, cells responded to pro-fibrogenic stimuli such as TGFB1, indicating that the HepGel can be used as a new 3D model to investigate HSC behaviour during disease modelling. In addition, we evaluated the suitability of HepGel for contraction assay. LX2 cells cultured in HepGel formed spheroids that eventually merged and repopulated the whole gel. Long-term exposure to TGFB1 induced a significant reduction in size of the whole gel compared to the control samples. TGFB1 is known as a pro-fibrogenic compound and not a contractile stimulus. Therefore, the gel contraction is probably due to ECM deposition and cytoskeletal tension generated in HSCs rather than proper contraction but proves that the material is useful for contraction assays.

The same set of experiments was repeated using primary human HSCs. A limiting step in the usage of 3D models is the number of cells needed, particularly when working when primary cells, since human donor material is scarce and methods for the simultaneous isolation of the individual cell types are tedious and yet yield few cells[177]. Furthermore, the initial cell number needed is usually very high due to the low cell proliferation rate of primary cells compared to immortalized cell lines. For instance, the number of cells used to repopulate scaffolds is around 1 million cells/scaffolds[36], and a recent study employing hydrogels to culture hepatocytes and HSCs used 150000 cells/µL[178]. As we show in this study, the usage of HepGel allowed the employment of much lower numbers of cells, for both LX2 cells (300 cells/µL – 15000 cells/hydrogel) and HSCs (1200 cells/µL – 60000 cells/hydrogel).

HepGel resulted capable to support primary human HSC cells viability and proliferation up to 11 days of culture. Primary human HSCs were then tested for responsiveness to TGFB1, and the results were compared between cells cultured in HepGel and in 2D plastic culture. Primary human HSC cultured on 2D and in HepGel showed significant differences in gene expression of activation and pro-fibrogenic genes, pointing out that HepGel is closer to the real liver microenvironment than 2D plastic dishes.

Tissue contraction in response to TGFB1 was tested in HepGel repopulated with primary HSCs. HSCs formed spheroids, but differently from LX2, did not merge and not completely repopulated the whole gel. Nonetheless, TGFB1 induced a significant reduction in spheroids volume compared to the control samples, proving HepGel to be a useful tool for contraction assays with primary human HSCs. To the best of our knowledge, although HSCs have been cultured on different types of hydrogels for many different application[179,180], the phenomenon of HSCs embedded in hydrogels and spontaneously forming spheroids has never been reported before. Therefore, the evaluation of HSCs contraction when assembled in spheroids has never been described and could be a new interesting tool for the study of HSCs biology.

A similar set of experiments was repeated with cultures of HSCs in ECM Gels. Based on previous experiments (L. Frenguelli et al., unpublished), higher concentrations of HSCs (3000 and 5000 cells/µL) were tested and showed stable metabolic activity and viability over the course of 14 days in both healthy and cirrhotic ECM Gels, with a similar trend to that observed in HepGels cultures. This was facilitated by the good porosity and ultrastructure of the ECM Gels, together with stable loss and storage modulus, which were evaluated with standardized tests and indicated stable crosslinking and a solid-like behaviour of the gel[181]. HSCs cultured in ECM Gels resulted responsive to TGFB1 treatment, which induced the upregulation of classic HSCs activation markers. No significant difference was observed in the gene expression of these markers when cells were cultured on the healthy *versus* cirrhotic ECM Gels, apart from a stronger expression of the proinflammatory marker IL6 in presence of TGFB1 and the cirrhotic ECM. The ECM Gels model was also compared to ECM scaffolds obtained from the same healthy and cirrhotic livers and classic 2D culture. Importantly, ECM Gels showed no difference in the expression of the majority of the activation/quiescence markers when compared to ECM scaffolds cultures, while, as previously published for ECM scaffolds[36], they presented with a marked decrease of activation markers and increase of quiescence markers when compared with classic plastic 2D cultures. These results can be explained by both the presence of human liver ECM, but also by the difference in stiffness with the plastic material, as it has been demonstrated that stiffness *per se* can modulate the phenotype of hepatic cells[182]. In the experiments presented in this thesis, DMA measurements showed that ECM Gels had a stiffness of 2 KPa, very similar to the one of healthy human livers[183], opposed to the stiffness of plastic which is of 2 GPa and therefore induces a HSCs phenotype which is far from that of the real human liver[35]. Importantly, while ECM scaffolds obtained from healthy and cirrhotic human livers kept the difference in stiffness which is observed in patients[37], stiffness between healthy and cirrhotic ECM Gels was similar. This is probably due to the loss of microarchitecture consequent to the ECM milling and resuspension in the gelling agent and the fact that, while the cirrhotic human liver presents with a higher content of ECM compared to healthy livers[184], healthy and cirrhotic ECM solution were used in the ECM Gels at the same concentration. Nonetheless, the increased stiffness of the hydrogels made of only nanocellulose suggests the possibility to modulate the stiffness of the ECM Gels by changing the concentration of gelling agent or of the ionic crosslinker[185]. Importantly, HSCs cultured in cirrhotic ECM Gels showed stronger differences due to the presence of the PNPLA3 I148M and TM6SF2 E156K variants compared to when cultured in healthy ECM Gels. This suggests a difference in composition of the healthy and cirrhotic ECM, which was previously demonstrated in ECM scaffolds[37], and will have to be confirmed by proteomic analysis of the ECM Gels, which is able to induce different responses in HSCs.

These results confirm that the ECM Gels are a suitable *in vitro* model to study HSCs behaviour, and, similarly to the ECM scaffolds, they resemble the characteristics of the healthy and cirrhotic liver microenvironment. In addition, it is important to note how using ECM Gels would be a step forward in the 3D modelling development compared to the ECM scaffolds, in terms of scalability. In fact, utilizing the ECM in solution instead than in scaffolds form, allows the formation of 10-times more samples from the same amount of starting material. Furthermore, homogenous distribution of the cells which can be achieved in ECM Gels but not in ECM scaffolds guarantees higher reproducibility between samples.

Similarly, to HepGels, healthy ECM Gels were also used to evaluate HSCs contraction, but, due to the lack of spheroids formation by HSCs in ECM Gels, a different method was used. Unfortunately, this method did not allow the detection of contraction in HSCs treated with Endothelin-1. This could have happened for several reasons. Among them, the amount and distribution of cells which did not aggregate in spheroids, and might not have been enough to form sufficient cell-cell interactions which could induce and transmit a mechano-response to the whole hydrogel. Furthermore, although ECM Gels showed to have a comparable stiffness to the human liver, different viscoelastic properties might facilitate the measure of contraction. Interestingly though, the test revealed a stronger basal contraction of cells carrying the PNPLA3 I148M and TM6SF2 E156K mutations compared to wild type cells. This was confirmed by analysis of Moesin protein content, which was higher in mutant cells compared to wild type cells, whereas wild type cells were more responsive to Endothelin-1 treatment compared to mutant cells, as shown by the higher increase in Moesin phosphorylation. Moesin is a protein which links actin filaments with membrane proteins, participating in the regulation of different cellular phenomena such as mitosis, cell migration, adhesion, motility and cell polarization[186–189]. Recently, moesin has been found to be involved in the contraction of HSCs and also in their activation and fibrogenesis[190]. This is in accordance with our observations on HSCs carrying the PNPLA3 I148M and TM6SF2 E156K mutations, which presented not only with increased Moesin expression, but also with increased COL1A1 and TIMP1 gene expression when cultured in cirrhotic ECM Gels. Further investigations including other motor proteins such as Myosin Light Chain II (MLCII) and pro-inflammatory and proliferation markers will be needed to further characterize how the presence of both genetic mutations impacts the behaviour and capacity of contraction of HSCs. Furthermore, being both PNPLA3 and TM6SF2 involved in the liver lipid metabolism, the impact of the two mutations on lipid metabolism and fatty acid oxidation in HSCs should explored. The method to investigate contraction, though, needs to be further optimized: the usage of a different gelling agent with different mechanical properties could be explored, as well as methods using advanced confocal microscopy and calcium-tracers, as it is well known calcium is essential in controlling HSCs contraction[191].

In conclusion, these results have shown that composite hydrogels made with healthy or cirrhotic ECM obtained from the decellularization of human livers are a useful tool to investigate behaviour of HSCs. Using this type of hydrogels has major advantages as it mimics better the human ECM microenvironment for hepatic cells, reduces the usage of high amounts of primary human cells and increases the feasibility to be used in a high throughput screening in future experiments.

5 General Conclusions and Future Perspectives.

The work presented in this thesis explored novel three-dimensional *in vitro* models to investigate the impact of genetic variants on the behaviour of hepatic stellate cells. The aim of this work was to unravel the effect of two genetic variants, the PNPLA3 I148M and the TM6SF2 E156K mutation, on the behaviour of hepatic stellate cells in the fibrogenic progression of chronic liver disease. The investigation was carried out by utilizing a novel 3D model based on human liver decellularized scaffolds which can recapitulate healthy and cirrhotic liver microenvironment and revealed specific molecular patterns in HSCs carrying the PNPLA3 I148M mutation. This model, previously tested and published for other hepatic cells[36,37,92], was then further optimized by utilizing the decellularized liver ECM to produce ECM-based hydrogels for the culture of HSCs. Hydrogels were characterized and used to investigate HSCs pro-fibrogenic behaviour and contraction capacity in presence of the PNPLA3 I148M and TM6SF2 E156K variants.

Epidemiological, familial, and twin studies have shown that hepatic steatosis and hepatic fibrosis are characterized by a degree of heritability of about 50% in patients with NAFLD[192]. In recent years, interest in genetic variations involved in the development of chronic liver disease has been growing, and numerous Genome Wide Association Studies (GWAS) have been conducted to identify polymorphisms associated with worsening liver disease[58,59,72]. Among these, the PNPLA3 I148M mutation accounts for the largest fraction of inherited predisposition to develop any progressive chronic liver disease, being related to the development of both steatohepatitis[58] and HCC[71], and being present in 50% of the general population[193]. While the presence of the PNPLA3 I148M mutation in hepatocytes has been shown to cause triglycerides accumulations and consequently development of steatosis[194,195], its role in the biology of HSCs is still unclear. HSCs carrying the PNPLA3 I148M variant have been shown to have increased activation[73], but the mechanism(s) driving this have not been fully investigated yet.

In this project, this issue was addressed by conducting transcriptomic analysis on HSCs isolated from patients WT or I148M for the PNPLA3 variant, which provided with an overview of significantly different regulated pathways, genes and upstream regulators between the two groups. The dataset is in the process of being published and will be therefore available for the scientific community to further explore the behaviour of HSCs carrying the PNPLA3 variant. In order to focus on pathways modulated by the PNPLA3 variant in HSCs and potentially relevant for NAFLD progression, the HSCs transcriptomic dataset was combined with RNA sequencing data obtained from a cohort of NAFLD patients carrying the WT or I148M PNPLA3 variant. Importantly, the comparison highlighted several shared pathways and genes between the two datasets, and many related to mitochondrial activity, oxidative stress, and ECM remodelling. Therefore, this project was focused on investigating those pathways, their upstream regulator TGFB1 and the target gene NR4A1.

The platform chosen to carry out validating experiments was the decellularized 3D ECM scaffolds model previously optimized in our laboratory[36,37]. This *in vitro* 3D model has already been shown to retain important features of the healthy and cirrhotic human liver microenvironment, such as tissue microarchitecture and stiffness, disease-specific ECM signature and growth factors storage[36,37] and, most importantly, the capacity of reverting HSCs to a more quiescent-like activation state[35,36] compared to classic plastic 2D cultures. The scaffolds model was also preferred over animal models for the study of the PNPLA3 I148M mutation for another important reason, this being the different tissue expression and functionality of PNPLA3 in mice compared to humans[79,80]. Using the human liver scaffolds model, this project confirmed RNA sequencing data indicating decreased mitochondrial activity in HSCs carrying the PNPLA3 I148M mutation, linking it to mitochondrial Complex IV deficiency, and additionally impaired anti-oxidant capacity. Furthermore, the TGFB1-regulated gene NR4A1 was shown to have a decreased expression and functionality in HSC PNPLA3-I148M which could be recovered by the natural agonist Csn-B, and therefore was identified as a possible druggable target for the treatment of chronic liver disease.

Importantly, we observed a modulation of HSCs behaviour due to the presence of cirrhotic liver ECM when compared to healthy ECM. In fact, HSCs cultured in cirrhotic liver scaffolds presented with increased oxidative stress and decreased response to Csn-B treatment. This highlights the importance of using a model recapitulating both the healthy and cirrhotic liver microenvironment.

In future studies, other pathways related to mitochondrial function and oxidative stress should be explored to further unravel the impact of the PNPLA3 variant on the fibrogenic activation of HSCs. Specifically, pathways related to lipid remodelling and fatty acid oxidation will be of particular importance due to data presented in this work and the specific role of PNPLA3 as a lipase[196]. In addition, NR4A1 expression and activity should be studied in a more complex multicellular model and drug studies conducted with NR4A1 as a target.

Performing these studies using the 3D ECM liver scaffolds as a platform could present with several limitations: (i) experimental variability due to different cell attachment to the liver scaffolds, (ii) co-culture limitations due to the variability in cell attachment and (iii) limited scalability due to the high quantity of liver tissue required to produce scaffolds.

Some of these limitations were addressed in Chapter 4 of this thesis, by using the decellularized liver ECM to produce ECM-based hydrogels for the *in vitro* culture of HSCs. In fact, due to their tuneable chemical and physical properties, hydrogels are becoming increasingly interesting in terms of High Throughput Screening (HTS) applications[197].

The decellularized liver ECM could form hydrogels when mixed with two different gelling agents, a thermoresponsive polymer (HepGels) and an ionic-cross linkable mix of nanocellulose and alginate distributed by CELLINK (ECM Gels). The usage of the decellularized ECM allowed a 10-fold reduction of required liver tissue and a homogenous distribution of the cells in the hydrogel sample. Both matrixes were able to support viability and metabolism of HSCs, responsiveness to pro-fibrogenic stimuli as TGFB1 and were inducing significantly less activation in HSCs compared to classic plastic 2D cultures.

Furthermore, ECM Gels proved to be mechanically stable and to resemble the stiffness of the healthy human liver. Due to their mechanical properties and adjustable shape, ECM hydrogels were tested as a tool to measure HSCs contraction, as an alternative to old and biased methods as collagen lattice gel contraction assays[198,199]. Although contraction was detectable in preliminary experiments when cells were cultured in HepGels, ECM Gels treated with a contractile agent did not support the detection of any contraction.

Importantly, regardless the loss of the original tissue microarchitecture, HSCs behaviour was similar in ECM Gels compared to ECM scaffolds. Therefore, ECM Gels were used as an alternative *in vitro* model to study profibrogenic behaviour of HSCs carrying genetic variants. In this case, the effect of both the PNPLA3 I148M and TM6SF2 E156K mutations on HSCs activation was investigated. Recent studies showed that the combination of disease associated variants in different loci can add-up and increase the risk of developing NAFLD and NASH both in patients[200] and in *in vitro* models[142]. The TM6SF2 E156K variant has also been associated with the progression of chronic liver disease[153,201] and with lipid accumulation in hepatocytes[157], but its role in combination with other variants in HSCs has never been investigated.

Our preliminary experiments showed that HSCs carrying the PNPLA3 I148M and TM6SF2 E156K mutation had an increased expression of activation markers compared to WT HSCs, induced by the presence of the cirrhotic ECM. Mutated cells were also less responsive to TGFB1 treatment compared to HSCs WT for PNPLA3 and TM6SF2. Although further studies are needed to explore the impact of these two mutations on HSCs, this indicates an effect of increased activation and confirms the 3D ECM Gels as a good model to study pro-fibrogenic behaviour of HSCs.

Future experiments will have to complete the characterization of the ECM Gels by confirming the preservation of key ECM components after hydrogel formation and revealing ECM composition differences between healthy and cirrhotic ECM Gels. In addition, a more extensive analysis of the impact of the cirrhotic ECM on HSCs behaviour will be conducted. The investigation of the effect of combined genetic variants on HSCs behaviour will be further developed by expanding the pool of HSCs donors including donors carrying a single variant and using omics techniques and optimizing co-cultures with other hepatic cells in a NASH-like environment. Once that is established, the effect of drugs aimed at different targets could be evaluated in a HTS setting.

Overall, this project explores the effect of different genetic variants on HSCs profibrogenic behaviour by using transcriptomic analysis and confirming findings in an *in vitro* 3D model using human liver derived ECM scaffolds. It also demonstrates the possibility of improving the scalability of the 3D scaffolds model by producing liver ECM hydrogels which can be used for *in vitro* modelling of liver fibrosis.

Bibliography.

1. Cheemerla, S. & Balakrishnan, M. Global Epidemiology of Chronic Liver Disease. *Clin Liver Dis (Hoboken)* **17**, 365–370 (2021).

2. Younossi, Z. *et al.* Global Perspectives on Nonalcoholic Fatty Liver Disease and Nonalcoholic Steatohepatitis. *Hepatology* **69**, 2672–2682 (2019).

3. Loomba, R. & Adams, L. A. The 20% Rule of NASH Progression: The Natural History of Advanced Fibrosis and Cirrhosis Caused by NASH. *Hepatology* vol. 70 1885–1888 Preprint at https://doi.org/10.1002/hep.30946 (2019).

4. Pierantonelli, I. & Svegliati-Baroni, G. Nonalcoholic Fatty Liver Disease: Basic Pathogenetic Mechanisms in the Progression from NAFLD to NASH. *Transplantation* **103**, E1–E13 (2019).

5. Taylor, R. S. *et al.* Association Between Fibrosis Stage and Outcomes of Patients With Nonalcoholic Fatty Liver Disease: A Systematic Review and Meta-Analysis. *Gastroenterology* **158**, 1611-1625.e12 (2020).

6. Pinzani, M. Pathophysiology of Liver Fibrosis. *Digestive Diseases* **33**, 492–497 (2015).

7. Friedman, S. L. Evolving challenges in hepatic fibrosis. *Nat Rev Gastroenterol Hepatol* **7**, 425–436 (2010).

8. El-Serag, H. B. Epidemiology of viral hepatitis and hepatocellular carcinoma. *Gastroenterology* vol. 142 Preprint at https://doi.org/10.1053/j.gastro.2011.12.061 (2012).

9. Youngmin A Lee, Michael C Wallace, and S. L. F. Pathobiology of liver fibrosis: a translational success story. *Gut* **41**, 919–925 (2015).

10. Dijk, F. Van. Targeted therapies in liver fibrosis : combining the best parts of platelet-derived growth factor BB and interferon gamma. *Front Med (Lausanne)* **2**, (2015).

11. Parola, M. & Pinzani, M. Liver fibrosis: Pathophysiology, pathogenetic targets and clinical issues. *Mol Aspects Med* **65**, 37–55 (2019).

12. Friedman, S. L. Hepatic Stellate Cells: Protean, Multifunctional, and Enigmatic Cells of the Liver. *Physiol Rev* **88**, 125–172 (2008).

13. Tsuchida, T. & Friedman, S. L. Mechanisms of hepatic stellate cell activation. *Nature Reviews Gastroenterology and Hepatology* Preprint at https://doi.org/10.1038/nrgastro.2017.38 (2017).

14. Böttcher, K. & Pinzani, M. Pathophysiology of liver fibrosis and the methodological barriers to the development of anti-fibrogenic agents. *Advanced Drug Delivery Reviews* (2017) doi:10.1016/j.addr.2017.05.016.

15. Luedde, T., Kaplowitz, N. & Schwabe, R. F. Cell death and cell death responses in liver disease: Mechanisms and clinical relevance. *Gastroenterology* **147**, 765-783.e4 (2014).

16. Canbay, A. *et al.* Apoptotic Body Engulfment by a Human Stellate Cell Line Is Profibrogenic. *Laboratory Investigation* **83**, 655–663 (2003).

17. Canbay, A., Friedman, S. & Gores, G. J. Apoptosis: The Nexus of Liver Injury and Fibrosis. *Hepatology* vol. 39 273–278 Preprint at https://doi.org/10.1002/hep.20051 (2004).

18. Rockey, D. C. Hepatic Fibrosis, Stellate Cells, and Portal Hypertension. *Clinics in Liver Disease* Preprint at https://doi.org/10.1016/j.cld.2006.08.017 (2006).

19. Gracia-Sancho, J., Marrone, G. & Fernández-Iglesias, A. Hepatic microcirculation and mechanisms of portal hypertension. *Nature Reviews Gastroenterology and Hepatology* Preprint at https://doi.org/10.1038/s41575-018-0097-3 (2019).

20. Russo, F. P. *et al.* The Bone Marrow Functionally Contributes to Liver Fibrosis. *Gastroenterology* **130**, 1807–1821 (2006).

21. Parola, M., Marra, F. & Pinzani, M. Myofibroblast - like cells and liver fibrogenesis: Emerging concepts in a rapidly moving scenario. *Molecular Aspects of Medicine* vol. 29 58–66 Preprint at https://doi.org/10.1016/j.mam.2007.09.002 (2008).

22. Schuppan, D., Ruehl, M., Somasundaram, R. & Hahn, E. G. Matrix as a modulator of hepatic fibrogenesis. *Seminars in Liver Disease* vol. 21 351–372 Preprint at https://doi.org/10.1055/s-2001-17556 (2001).

23. Friedman, S. L., Roll, F. J., Boyles, J. & Bissell, D. M. Hepatic lipocytes: the principal collagen-producing cells of normal rat liver. *Proc Natl Acad Sci U S A* **82**, 8681–5 (1985).

24. Hernandez-Gea, V. & Friedman, S. L. Pathogenesis of Liver Fibrosis. *Annual Review of Pathology: Mechanisms of Disease* **6**, 425–456 (2011).

25. Knittel, T. *et al.* Expression patterns of matrix metalloproteinases and their inhibitors in parenchymal and non-parenchymal cells of rat liver: Regulation by TNF-?? and TGF-??1. *J Hepatol* **30**, 48–60 (1999).

26. Frantz, C., Stewart, K. M. & Weaver, V. M. The extracellular matrix at a glance. *J Cell Sci* **123**, 4195–4200 (2010).

27. Horning, J. L. *et al.* 3-D tumor model for in vitro evaluation of anticancer drugs. *Mol Pharm* **5**, 849–862 (2008).

28. Shanks, N., Greek, R. & Greek, J. Are animal models predictive for humans? *Philosophy, Ethics, and Humanities in Medicine* **4**, 2 (2009).

29. Birgersdotter, A., Sandberg, R. & Ernberg, I. Gene expression perturbation in vitro—A growing case for three-dimensional (3D) culture systems. *Semin Cancer Biol* **15**, 405–412 (2005).

30. de Minicis, S. *et al.* Gene Expression Profiles During Hepatic Stellate Cell Activation in Culture and In Vivo. *Gastroenterology* **132**, 1937–1946 (2007).

31. Freires, I. A., Sardi, J. de C. O., de Castro, R. D. & Rosalen, P. L. Alternative Animal and Non-Animal Models for Drug Discovery and Development: Bonus or Burden? *Pharm Res* **34**, 681–686 (2017).

32. Andrade, E. L. *et al.* Non-clinical studies in the process of new drug development – Part II : Good laboratory practice , metabolism , pharmacokinetics , safety and dose translation to clinical studies. *Brazilian Journal of Medical and Biological Research* **49**, 1–19 (2016).

33. Arrowsmith, J. Trial watch: Phase III and submission failures: 2007–2010. *Nat Rev Drug Discov* **10**, 87–87 (2011).

34. Al-Akkad, W. *et al.* Tissue-Specific Human Extracellular Matrix Scaffolds Promote Pancreatic Tumour Progression and Chemotherapy Resistance. *Cells* **11**, 1–23 (2022).

35. Mazza, G., Al-Akkad, W. & Rombouts, K. Engineering in vitro models of hepatofibrogenesis. *Advanced Drug Delivery Reviews* vol. 121 147–157 Preprint at https://doi.org/10.1016/j.addr.2017.05.018 (2017).

36. Mazza, G. *et al.* Rapid production of human liver scaffolds for functional tissue engineering by high shear stress oscillation-decellularization. *Sci Rep* **7**, 5534 (2017).

37. Mazza, G. *et al.* Cirrhotic Human Liver Extracellular Matrix 3D Scaffolds Promote Smad-Dependent TGF-β1 Epithelial Mesenchymal Transition. *Cells* **9**, (2019).

38. Tsamandouras, N. *et al.* Quantitative Assessment of Population Variability in Hepatic Drug Metabolism Using a Perfused Three-Dimensional Human Liver

Microphysiological System. *Journal of Pharmacology and Experimental Therapeutics* **360**, 95–105 (2016).

39. Fitzgerald, K. A., Malhotra, M., Curtin, C. M., O'Brien, F. J. & O'Driscoll, C. M. Life in 3D is never flat: 3D models to optimise drug delivery. *Journal of Controlled Release* vol. 215 39–54 Preprint at https://doi.org/10.1016/j.jconrel.2015.07.020 (2015).

40. Vatakuti, S., Olinga, P., Pennings, J. L. A. & Groothuis, G. M. M. Validation of precision-cut liver slices to study drug-induced cholestasis: a transcriptomics approach. *Arch Toxicol* **91**, 1401–1412 (2017).

41. Sasagawa, T., Shimizu, T., Yamato, M. & Okano, T. Endothelial colony-forming cells for preparing prevascular three-dimensional cell-dense tissues using cell-sheet engineering. *J Tissue Eng Regen Med* **10**, 739–747 (2016).

42. Kim, K., Utoh, R., Ohashi, K., Kikuchi, T. & Okano, T. Fabrication of functional 3D hepatic tissues with polarized hepatocytes by stacking endothelial cell sheets in vitro. *J Tissue Eng Regen Med* **11**, 2071–2080 (2017).

43. Kostrzewski, T. *et al.* A Microphysiological System for Studying Nonalcoholic Steatohepatitis. *Hepatol Commun* **4**, 77–91 (2020).

44. Ronaldson-Bouchard, K. *et al. A multi-organ chip with matured tissue niches linked by vascular flow*. *Nature Biomedical Engineering* vol. 6 (Springer US, 2022).

45. Leite, S. B. *et al.* Novel human hepatic organoid model enables testing of drug-induced liver fibrosis in vitro. *Biomaterials* **78**, 1–10 (2016).

46. Fennema, E., Rivron, N., Rouwkema, J., van Blitterswijk, C. & de Boer, J. Spheroid culture as a tool for creating 3D complex tissues. *Trends in Biotechnology* vol. 31 108–115 Preprint at https://doi.org/10.1016/j.tibtech.2012.12.003 (2013).

47. Hakkinen, K. M., Harunaga, J. S., Doyle, A. D. & Yamada, K. M. Direct Comparisons of the Morphology, Migration, Cell Adhesions, and Actin Cytoskeleton of Fibroblasts in Four Different Three-Dimensional Extracellular Matrices. *Tissue Eng Part A* **17**, 713–724 (2011).

48. Szalowska, E., Stoopen, G., Groot, M. J., Hendriksen, P. J. M. & Peijnenburg, A. a C. M. Treatment of mouse liver slices with cholestatic hepatotoxicants results in down-regulation of Fxr and its target genes. *BMC Med Genomics* **6**, 39 (2013).

49. van Swelm, R. P. L. *et al.* Proteomic profiling in incubation medium of mouse, rat and human precision-cut liver slices for biomarker detection regarding

acute drug-induced liver injury. *Journal of Applied Toxicology* **34**, 993–1001 (2014).

50. Rimann, M. & Graf-Hausner, U. Synthetic 3D multicellular systems for drug development. *Current Opinion in Biotechnology* vol. 23 803–809 Preprint at https://doi.org/10.1016/j.copbio.2012.01.011 (2012).

51. Miranda, J. P. *et al.* Extending hepatocyte functionality for drug-testing applications using high-viscosity alginate-encapsulated three-dimensional cultures in bioreactors. *Tissue Eng Part C Methods* **16**, 1223–1232 (2010).

52. Karlsen, T. H., Lammert, F. & Thompson, R. J. Genetics of liver disease: From pathophysiology to clinical practice. *J Hepatol* **62**, S6–S14 (2015).

53. Petrukhin, K. *et al.* Mapping, cloning and genetic characterization of the region containing the Wilson disease gene. (1993).

54. Feder, J. N. *et al.* A novel MHC class I-like gene is mutated in patients with hereditary haemochromatosis. (1996).

55. Janciauskiene, S. M. *et al.* The discovery of α1-antitrypsin and its role in health and disease. *Respir Med* **105**, 1129–1139 (2011).

56. Buch, S. *et al.* A genome-wide association scan identifies the hepatic cholesterol transporter ABCG8 as a susceptibility factor for human gallstone disease. *Nat Genet* **39**, 995–999 (2007).

57. Gideon M. Hirschfield, M.R.C.P., Ph.D., Xiangdong Liu, Ph. D. *et al.* Primary Biliary Cirrhosis Associated with HLA, IL12A, and IL12RB2 Variants. *The new england journal o f medicine* **43**, 2138–2142 (2009).

58. Romeo, S. *et al.* Genetic variation in PNPLA3 confers susceptibility to nonalcoholic fatty liver disease. *Nat Genet* (2008) doi:10.1038/ng.257.

59. Kozlitina, J. *et al.* Exome-wide association study identifies a TM6SF2 variant that confers susceptibility to nonalcoholic fatty liver disease. *Nature Publishing Group* (2014) doi:10.1038/ng.2901.

60. Yang, J. *et al.* PNPLA3 and TM6SF2 variants as risk factors of hepatocellular carcinoma across various etiologies and severity of underlying liver diseases. *Int J Cancer* (2019) doi:10.1002/ijc.31910.

61. Mancina, R. M. *et al.* The MBOAT7-TMC4 Variant rs641738 Increases Risk of Nonalcoholic Fatty Liver Disease in Individuals of European Descent. *Gastroenterology* **150**, 1219-1230.e6 (2016).

62. Lin, Y.-C., Chang, P.-F., Chang, M.-H. & Ni, Y.-H. Genetic variants in GCKR and PNPLA3 confer susceptibility to nonalcoholic fatty liver disease in obese individuals 1-3. *Am J Clin Nutr* **99**, 869–74 (2014).

63. Abul-Husn, N. S. *et al.* A Protein-Truncating HSD17B13 Variant and Protection from Chronic Liver Disease . *New England Journal of Medicine* **378**, 1096–1106 (2018).

64. Zheng, M., Allington, G. & Vilarinho, S. Genomic medicine for liver disease. (2022) doi:10.1002/hep.32364.

65. Ge, D. *et al.* Genetic variation in IL28B predicts hepatitis C treatment-induced viral clearance. (2009) doi:10.1038/nature08309.

66. Trépo, E. & Valenti, L. Update on NAFLD genetics: From new variants to the clinic. *J Hepatol* **72**, 1196–1209 (2020).

67. He, S. *et al.* A sequence variation (I148M) in PNPLA3 associated with nonalcoholic fatty liver disease disrupts triglyceride hydrolysis. *Journal of Biological Chemistry* **285**, 6706–6715 (2010).

68. Pingitore, P. *et al.* Recombinant PNPLA3 protein shows triglyceride hydrolase activity and its I148M mutation results in loss of function. *Biochim Biophys Acta Mol Cell Biol Lipids* (2014) doi:10.1016/j.bbalip.2013.12.006.

69. Pirazzi, C. *et al.* PNPLA3 has retinyl-palmitate lipase activity in human hepatic stellate cells. *Hum Mol Genet* (2014) doi:10.1093/hmg/ddu121.

70. Valenti, L. *et al.* Homozygosity for the patatin-like phospholipase-3/adiponutrin i148m polymorphism influences liver fibrosis in patients with nonalcoholic fatty liver disease. *Hepatology* (2010) doi:10.1002/hep.23622.

71. Valenti, L., Dongiovanni, P., Ginanni Corradini, S., Burza, M. A. & Romeo, S. PNPLA3 I148M variant and hepatocellular carcinoma: A common genetic variant for a rare disease. *Digestive and Liver Disease* Preprint at https://doi.org/10.1016/j.dld.2012.12.006 (2013).

72. Buch, S. *et al.* A genome-wide association study confirms PNPLA3 and identifies TM6SF2 and MBOAT7 as risk loci for alcohol-related cirrhosis. *Nat Genet* **47**, 1443–1448 (2015).

73. Bruschi, F. V. *et al.* The PNPLA3 I148M variant modulates the fibrogenic phenotype of human hepatic stellate cells. *Hepatology* (2017) doi:10.1002/hep.29041.

74. Bruschi, F. V., Tardelli, M., Einwallner, E., Claudel, T. & Trauner, M. Pnpla3 I148M up-regulates hedgehog and yap signaling in human hepatic stellate cells. *Int J Mol Sci* **21**, 1–16 (2020).

75. Bruschi, F. V. *et al.* PNPLA3 I148M Variant Impairs Liver X Receptor Signaling and Cholesterol Homeostasis in Human Hepatic Stellate Cells. *Hepatol Commun* **3**, 1191 (2019).

76. Smagris, E. *et al.* Pnpla3I148M knockin mice accumulate PNPLA3 on lipid droplets and develop hepatic steatosis. *Hepatology* **61**, 108–118 (2015).

77. Li, J. Z. *et al.* Chronic overexpression of PNPLA3 I148M in mouse liver causes hepatic steatosis. *J Clin Invest* **122**, (2012).

78. Lindén, D. *et al.* Pnpla3 silencing with antisense oligonucleotides ameliorates nonalcoholic steatohepatitis and fibrosis in Pnpla3 I148M knock-in mice. *Mol Metab* **22**, 49–61 (2019).

79. Lake, A. C. *et al.* Expression, regulation, and triglyceride hydrolase activity of Adiponutrin family members. *J Lipid Res* **46**, 2477–2487 (2005).

80. Huang, Y. *et al.* A feed-forward loop amplifies nutritional regulation of PNPLA3. *Proc Natl Acad Sci U S A* **107**, 7892–7897 (2010).

81. Ramos, M. J., Bandiera, L., Menolascina, F. & Fallowfield, J. A. In vitro models for non-alcoholic fatty liver disease: Emerging platforms and their applications. *iScience* vol. 25 Preprint at https://doi.org/10.1016/j.isci.2021.103549 (2022).

82. Zhang, X. *et al.* Decellularized extracellular matrix scaffolds: Recent trends and emerging strategies in tissue engineering. *Bioact Mater* **10**, 15–31 (2022).

83. Crapo, P. M., Gilbert, T. W. & Badylak, S. F. An overview of tissue and whole organ decellularization processes. *Biomaterials* vol. 32 3233–3243 Preprint at https://doi.org/10.1016/j.biomaterials.2011.01.057 (2011).

84. Baselli, G. A. *et al.* Liver transcriptomics highlights interleukin-32 as novel NAFLD-related cytokine and candidate biomarker. *Gut* **69**, 1855–1866 (2020).

85. Kleiner, D. E. *et al.* Design and validation of a histological scoring system for nonalcoholic fatty liver disease. *Hepatology* **41**, 1313–1321 (2005).

86. Rombouts, K. & Carloni, V. Determination and characterization of tetraspanin-Associated phosphoinositide-4 kinases in primary and neoplastic liver cells. *Methods in Molecular Biology* **1376**, 203–212 (2016).

87. Cunningham, F. *et al.* Ensembl 2015. *Nucleic Acids Res* **43**, (2015).

88. Dobin, A. *et al.* Sequence analysis STAR: ultrafast universal RNA-seq aligner. **29**, 15–21 (2013).

89. Li, B. & Dewey, C. N. RSEM: Accurate transcript quantification from RNA-Seq data with or without a reference genome. *BMC Bioinformatics* **12**, 1–16 (2011).

90. Love, M. I., Huber, W. & Anders, S. Moderated estimation of fold change and dispersion for RNA-seq data with DESeq2. *Genome Biol* **15**, 1–21 (2014).

91. Laskaratos, F.-M. *et al.* Transcriptomic Profiling of In Vitro Tumor-Stromal Cell Paracrine Crosstalk Identifies Involvement of the Integrin Signaling Pathway in the Pathogenesis of Mesenteric Fibrosis in Human Small Intestinal Neuroendocrine Neoplasms. *Article 629665 1 Front. Oncol* **11**, 629665 (2021).

92. Thanapirom, K. *et al.* Optimization and validation of a novel three-dimensional co-culture system in decellularized human liver scaffold for the study of liver fibrosis and cancer. *Cancers (Basel)* **13**, (2021).

93. Schmittgen, T. D. & Livak, K. J. Analyzing real-time PCR data by the comparative CT method. *Nat Protoc* **3**, 1101–1108 (2008).

94. Marrone, G. *et al.* The adenosine monophosphate–activated protein kinase—vacuolar adenosine triphosphatase–pH axis: A key regulator of the profibrogenic phenotype of human hepatic stellate cells. *Hepatology* **68**, 1140–1153 (2018).

95. Diller, T., Thompson, J. & Steer, B. Biological validation of a novel process and product for quantitating western blots. *J Biotechnol* **326**, 52–60 (2021).

96. Protasoni, M., Kroon, A. M. & Taanman, J.-W. Mitochondria as oncotarget: a comparison between the tetracycline analogs doxycycline and COL-3. *Oncotarget* **9**, 33818–33831 (2018).

97. Wittig, I., Braun, H.-P. & Schägger, H. Blue native PAGE. (2006) doi:10.1038/nprot.2006.62.

98. Samarakoon, R. & Higgins, P. J. Integration of non-SMAD and SMAD signaling in TGF-β1-induced plasminogen activator inhibitor type-1 gene expression in vascular smooth muscle cells. *Thrombosis and Haemostasis* vol. 100 976–983 Preprint at https://doi.org/10.1160/TH08-05-0273 (2008).

99. Begliuomini, C. *et al.* VARS2-linked mitochondrial encephalopathy: Two case reports enlarging the clinical phenotype. *BMC Med Genet* **20**, 1–6 (2019).

100. Kim, J. A., Wei, Y. & Sowers, J. R. Role of mitochondrial dysfunction in insulin resistance. *Circulation Research* vol. 102 401–414 Preprint at https://doi.org/10.1161/CIRCRESAHA.107.165472 (2008).

101. Liu, R. M. & Desai, L. P. Reciprocal regulation of TGF-β and reactive oxygen species: A perverse cycle for fibrosis. *Redox Biology* vol. 6 565–577 Preprint at https://doi.org/10.1016/j.redox.2015.09.009 (2015).

102. Pols, T. W. H. *et al.* Nur77 modulates hepatic lipid metabolism through suppression of SREBP1c activity. *Biochem Biophys Res Commun* **366**, 910–916 (2008).

103. Xu, Y. *et al.* Knockout of Nur77 Leads to Amino Acid, Lipid, and Glucose Metabolism Disorders in Zebrafish. *Front Endocrinol (Lausanne)* **13**, (2022).

104. Lee, S. O. *et al.* The orphan nuclear receptor NR4A1 (Nur77) regulates oxidative and endoplasmic reticulum stress in pancreatic cancer cells. *Molecular Cancer Research* **12**, 527–538 (2014).

105. Palumbo-Zerr, K. *et al.* Orphan nuclear receptor NR4A1 regulates transforming growth factor-β 2 signaling and fibrosis. *Nat Med* **21**, 150–158 (2015).

106. Zhan, Y. *et al.* Cytosporone B is an agonist for nuclear orphan receptor Nur77. (2008) doi:10.1038/nchembio.106.

107. Zeng, X. *et al.* NR4A1 is Involved in Fibrogenesis in Ovarian Endometriosis. *Cellular Physiology and Biochemistry* **46**, 1078–1090 (2018).

108. Wang, A., Rud, J., Olson, C. M., Anguita, J. & Osborne, B. A. Phosphorylation of Nur77 by the MEK-ERK-RSK Cascade Induces Mitochondrial Translocation and Apoptosis in T Cells. *The Journal of Immunology* **183**, 3268–3277 (2009).

109. Xiong, Y. *et al.* Reactivation of NR4A1 Restrains Chondrocyte Inflammation and Ameliorates Osteoarthritis in Rats. *Front Cell Dev Biol* **8**, 158 (2020).

110. Zhang, C. *et al.* Mitochondrial Dysfunction and Chronic Liver Disease. *Curr Issues Mol Biol* **44**, 3156–3165 (2022).

111. Begriche, K., Igoudjil, A., Pessayre, D. & Fromenty, B. Mitochondrial dysfunction in NASH: Causes, consequences and possible means to prevent it. *Mitochondrion* **6**, 1–28 (2006).

112. Teodoro, J. S., Rolo, A. P., Duarte, F. v., Simões, A. M. & Palmeira, C. M. Differential alterations in mitochondrial function induced by a choline-deficient diet: Understanding fatty liver disease progression. *Mitochondrion* **8**, 367–376 (2008).

113. Koliaki, C. *et al.* Adaptation of Hepatic Mitochondrial Function in Humans with Non-Alcoholic Fatty Liver Is Lost in Steatohepatitis. *Cell Metab* **21**, 739–746 (2015).

114. Min, H. K. *et al.* Metabolic profiling reveals that PNPLA3 induces widespread effects on metabolism beyond triacylglycerol remodeling in Huh-7 hepatoma cells. *Am J Physiol Gastrointest Liver Physiol* **307**, 66–76 (2014).

115. Pérez-Carreras, M. *et al.* Defective hepatic mitochondrial respiratory chain in patients with nonalcoholic steatohepatitis. *Hepatology* **38**, 999–1007 (2003).

116. Chimienti, G. *et al.* The mitochondrial trigger in an animal model of nonalcoholic fatty liver disease. *Genes (Basel)* **12**, (2021).

117. Lee, Y. I. *et al.* Human Hepatitis B Virus-X Protein Alters Mitochondrial Function and Physiology in Human Liver Cells. *Journal of Biological Chemistry* **279**, 15460–15471 (2004).

118. Lev, D. *et al.* Reversible fulminant lactic acidosis and liver failure in an infant with hepatic cytochrome-c oxidase deficiency. *J Inherit Metab Dis* **25**, 371–377 (2002).

119. Aharoni-Simon, M., Hann-Obercyger, M., Pen, S., Madar, Z. & Tirosh, O. Fatty liver is associated with impaired activity of PPARγ-coactivator 1α (PGC1α) and mitochondrial biogenesis in mice. *Laboratory Investigation* **91**, 1018–1028 (2011).

120. Chen, Z., Tian, R., She, Z., Cai, J. & Li, H. Role of oxidative stress in the pathogenesis of nonalcoholic fatty liver disease. *Free Radic Biol Med* **152**, 116–141 (2020).

121. Masarone, M. *et al.* Role of oxidative stress in pathophysiology of nonalcoholic fatty liver disease. *Oxid Med Cell Longev* **2018**, (2018).

122. Kushnareva, Y., Murphy, A. N. & Andreyev, A. Complex I-mediated reactive oxygen species generation: Modulation by cytochrome c and NAD(P)+ oxidation-reduction state. *Biochemical Journal* **368**, 545–553 (2002).

123. Ayala, A., Muñoz, M. F. & Argüelles, S. Lipid peroxidation: Production, metabolism, and signaling mechanisms of malondialdehyde and 4-hydroxy-2-nonenal. *Oxid Med Cell Longev* **2014**, (2014).

124. Hruszkewycz, A. M. & Bergtold, D. S. The 8-hydroxyguanine content of isolated mitochondria increases with lipid peroxidation. *Mutation Research Letters* **244**, 123–128 (1990).

125. Chen, J., Schenker, S., Frosto, T. A. & Henderson, G. I. Inhibition of cytochrome c oxidase activity by 4-hydroxynonenal (HNE). Role of HNE adduct formation with the enzyme subunits. *Biochim Biophys Acta Gen Subj* **1380**, 336–344 (1998).

126. Chambel, S. S., Santos-Gonçalves, A. & Duarte, T. L. The dual role of Nrf2 in nonalcoholic fatty liver disease: Regulation of antioxidant defenses and hepatic lipid metabolism. *Biomed Res Int* **2015**, (2015).

127. Besse-Patin, A., Léveillé, M., Oropeza, D., Nguyen, B. N. & Prat, A. Estrogen Signals Through Peroxisome Proliferator-Activated Receptor−γ Coactivator 1α to Reduce Oxidative Damage Associated With Diet-Induced Fatty Liver Disease. *Gastroenterology* **152**, 243–256 (2017).

128. Okina, Y. *et al.* TGF-β1-driven reduction of cytoglobin leads to oxidative DNA damage in stellate cells during non-alcoholic steatohepatitis. *J Hepatol* **73**, 882–895 (2020).

129. Pingitore, P. *et al.* PNPLA3 overexpression results in reduction of proteins predisposing to fibrosis. *Hum Mol Genet* **25**, 5212 (2016).

130. Dewidar, B., Meyer, C., Dooley, S. & Meindl-Beinker, N. TGF-β in Hepatic Stellate Cell Activation and Liver Fibrogenesis-Updated 2019. (2019) doi:10.3390/cells8111419.

131. Human Protein Atlas. https://www.proteinatlas.org/ENSG00000123358-NR4A1/single+cell+type/liver.

132. Claveria-Cabello, A. *et al.* Dual pharmacological targeting of hdacs and pde5 inhibits liver disease progression in a mouse model of biliary inflammation and fibrosis. *Cancers (Basel)* **12**, 1–27 (2020).

133. Biswas, S. *et al.* Conformationally Restricted Dipeptide-Based Nanoparticles for Delivery of siRNA in Experimental Liver Cirrhosis. *ACS Omega* (2022) doi:10.1021/acsomega.2c05292.

134. Huang, Q. *et al.* NR4A1 inhibits the epithelial-mesenchymal transition of hepatic stellate cells: Involvement of TGF-β-Smad2/3/4-ZEB signaling. *Open Life Sci* **17**, 447–454 (2022).

135. Valenti, L., Dongiovanni, P., Ginanni Corradini, S., Burza, M. A. & Romeo, S. PNPLA3 I148M variant and hepatocellular carcinoma: A common genetic variant for a rare disease. *Digestive and Liver Disease* **45**, 619–624 (2013).

136. Geng, N. *et al.* Nuclear receptor Nur77 protects against oxidative stress by maintaining mitochondrial homeostasis via regulating mitochondrial fission and mitophagy in smooth muscle cell. *J Mol Cell Cardiol* **170**, 22–33 (2022).

137. Venu, V. K. P. *et al.* Metformin Prevents Hyperglycemia-Associated, Oxidative Stress-Induced Vascular Endothelial Dysfunction: Essential Role for the Orphan Nuclear Receptor Human Nuclear Receptor 4A1 (Nur77). *Mol Pharmacol* **100**, 428–455 (2021).

138. Wang, D. *et al.* FGF1ΔHBS prevents diabetic cardiomyopathy by maintaining mitochondrial homeostasis and reducing oxidative stress via AMPK/Nur77 suppression. *Signal Transduct Target Ther* **6**, (2021).

139. Zheng, Y., Tao, Y., Zhan, X. & Wu, Q. Nuclear receptor 4A1 (NR4A1) silencing protects hepatocyte against hypoxia-reperfusion injury in vitro by activating liver kinase B1 (LKB1)/AMP-activated protein kinase (AMPK) signaling. *Bioengineered* **13**, 8349–8359 (2022).

140. Zhou, F. *et al.* Berberine-induced activation of AMPK increases hepatic FGF21 expression via NUR77. *Biochem Biophys Res Commun* **495**, 1936–1941 (2018).

141. Zhao, N. *et al.* The Nuclear Orphan Receptor Nur77 Alleviates Palmitate-induced Fat Accumulation by Down-regulating G0S2 in HepG2 Cells. *Sci Rep* **8**, 1–10 (2018).

142. Longo, M. *et al.* TM6SF2/PNPLA3/MBOAT7 Loss-of-Function Genetic Variants Impact on NAFLD Development and Progression Both in Patients and in In Vitro Models. *CMGH* **13**, 759–788 (2022).

143. Luukkonen, P. K. *et al.* Distinct contributions of metabolic dysfunction and genetic risk factors in the pathogenesis of non-alcoholic fatty liver disease. *J Hepatol* **76**, 526–535 (2022).

144. Hellerbrand, C. Hepatic stellate cells - The pericytes in the liver. *Pflugers Arch* **465**, 775–778 (2013).

145. Soon, R. K. & Yee, H. F. Stellate Cell Contraction: Role, Regulation, and Potential Therapeutic Target. *Clin Liver Dis* **12**, 791–803 (2008).

146. Reynaert, H., Thompson, M. G., Thomas, T. & Geerts, A. Hepatic stellate cells: Role in microcirculation and pathophysiology of portal hypertension. *Gut* Preprint at https://doi.org/10.1136/gut.50.4.571 (2002).

147. Bianco, C. *et al.* Non-invasive stratification of hepatocellular carcinoma risk in non-alcoholic fatty liver using polygenic risk scores. *J Hepatol* **74**, 775–782 (2021).

148. Donati, B. *et al.* MBOAT7 rs641738 variant and hepatocellular carcinoma in non-cirrhotic individuals. doi:10.1038/s41598-017-04991-0.

149. Krawczyk, M. *et al.* Combined effects of the PNPLA3 rs738409, TM6SF2 rs58542926, and MBOAT7 rs641738 variants on NAFLD severity: A multicenter biopsy-based study1. *J Lipid Res* **58**, 247–255 (2017).

150. Xu, M. *et al.* Interaction of TM6SF2 E167K and PNPLA3 I148M variants in NAFLD in northeast China. *Ann Hepatol* **18**, 456–460 (2019).

151. Anstee, Q. M. & Day, C. P. The Genetics of Nonalcoholic Fatty Liver Disease: Spotlight on PNPLA3 and TM6SF2. *Semin Liver Dis* **35**, 270–290 (2015).

152. Loomba, R. & Sanyal, A. J. The global NAFLD epidemic. *Nat Rev Gastroenterol Hepatol* **10**, 686–690 (2013).

153. Roh, Y. S., Loomba, R. & Seki, E. The TM6SF2 Variants, Novel Genetic Predictors for Nonalcoholic Steatohepatitis. *Gastroenterology* **148**, 252–254 (2015).

154. Coppola, N. *et al.* TM6SF2 E167K variant is associated with severe steatosis in chronic hepatitis C, regardless of PNPLA3 polymorphism. *Liver International* **35**, 1959–1963 (2015).

155. Eslam, M. *et al.* Diverse impacts of the rs58542926 E167K variant in TM6SF2 on viral and metabolic liver disease phenotypes. *Hepatology* **64**, 34–46 (2016).

156. Liu, Z. *et al.* Distinct roles for non-muscle myosin II isoforms in mouse hepatic stellate cells. *J Hepatol* **54**, 132–141 (2011).

157. Mahdessian, H. *et al.* TM6SF2 is a regulator of liver fat metabolism influencing triglyceride secretion and hepatic lipid droplet content. *Proc Natl Acad Sci U S A* **111**, 8913–8918 (2014).

158. LIU, S. *et al.* In vitro analysis of hepatic stellate cell activation influenced by transmembrane 6 superfamily 2 polymorphism. *Mol Med Rep* **23**, 1–7 (2020).

159. Ullah, F., Othman, M. B. H., Javed, F., Ahmad, Z. & Akil, H. M. Classification, processing and application of hydrogels: A review. *Materials Science and Engineering C* **57**, 414–433 (2015).

160. Subramanian, K. G. & Vijayakumar, V. Hydrogels: Classification, Synthesis, Characterization, and Applications. *Encyclopedia of Biomedical Polymers and Polymeric Biomaterials* 3879–3892 (2015) doi:10.1081/e-ebpp-120049894.

161. Sheffield, C., Meyers, K., Johnson, E. & Rajachar, R. M. Application of Composite Hydrogels to Control Physical Properties in Tissue Engineering and Regenerative Medicine. (2018) doi:10.3390/gels4020051.

162. Blanazs, A. *et al.* Sterilizable gels from thermoresponsive block copolymer worms. *J Am Chem Soc* (2012) doi:10.1021/ja3024059.

163. Burdick, J. A. & Anseth, K. S. Photoencapsulation of osteoblasts in injectable RGD-modified PEG hydrogels for bone tissue engineering. *Biomaterials* (2002) doi:10.1016/S0142-9612(02)00176-X.

164. Rouillard, A. D. *et al.* Methods for photocrosslinking alginate hydrogel scaffolds with high cell viability. *Tissue Eng Part C Methods* (2011) doi:10.1089/ten.tec.2009.0582.

165. Geckil, H., Xu, F., Zhang, X., Moon, S. & Demirci, U. Engineering hydrogels as extracellular matrix mimics. *Nanomedicine* **5**, 469–484 (2010).

166. Tibbitt, M. W. & Anseth, K. S. Hydrogels as extracellular matrix mimics for 3D cell culture. *Biotechnol Bioeng* **103**, 655–663 (2009).

167. Hughes, C. S., Postovit, L. M. & Lajoie, G. A. Matrigel: A complex protein mixture required for optimal growth of cell culture. doi:10.1002/pmic.200900758.

168. Arteel, G. E. & Naba, A. The liver matrisome – looking beyond collagens. *JHEP Reports* **2**, (2020).

169. Battista, S. *et al.* The effect of matrix composition of 3D constructs on embryonic stem cell differentiation. *Biomaterials* (2005) doi:10.1016/j.biomaterials.2005.04.003.

170. Duan, Y. *et al.* Hybrid gel composed of native heart matrix and collagen induces cardiac differentiation of human embryonic stem cells without supplemental growth factors. *J Cardiovasc Transl Res* (2011) doi:10.1007/s12265-011-9304-0.

171. Frenguelli, L. Development of Human Liver Extracellular Matrix Hydrogels for Three Dimensional Cell Culture and Cell Transplantation. *University College of London* (2020).

172. Canton, I. *et al.* Mucin-inspired thermoresponsive synthetic hydrogels induce stasis in human pluripotent stem cells and human embryos. *ACS Cent Sci* (2016) doi:10.1021/acscentsci.5b00370.

173. Markstedt, K., Mantas, A., Tournier, I., Ha, D. & Gatenholm, P. 3D Bioprinting Human Chondrocytes with Nanocellulose − Alginate Bioink for Cartilage Tissue Engineering Applications. (2015) doi:10.1021/acs.biomac.5b00188.

174. Keskin-Erdogan, Z. *et al.* Utilization of GelMA with phosphate glass fibers for glial cell alignment. *J Biomed Mater Res A* **109**, 2212–2224 (2021).

175. Jastram, A., Claus, J., Janmey, P. A. & Kragl, U. Rheological properties of hydrogels based on ionic liquids. *Polym Test* **93**, 106943 (2021).

176. Mazza, G. *et al.* Decellularized human liver as a natural 3D-scaffold for liver bioengineering and transplantation. *Sci Rep* **5**, 13079 (2015).

177. Werner, M. *et al.* All-in-one: Advanced preparation of human parenchymal and non-parenchymal liver cells. *PLoS One* (2015) doi:10.1371/journal.pone.0138655.

178. Nguyen, D. G. *et al.* Bioprinted 3D primary liver tissues allow assessment of organ-level response to clinical drug induced toxicity in vitro. *PLoS One* (2016) doi:10.1371/journal.pone.0158674.

179. Caliari, S. R. *et al.* Stiffening hydrogels for investigating the dynamics of hepatic stellate cell mechanotransduction during myofibroblast activation. *Sci Rep* **6**, 21387 (2016).

180. Rockey, D. C., Housset, C. N. & Friedman, S. L. Activation-dependent Contractility of Rat Hepatic Lipocytes in Culture and In Vivo. *J Clin Invest* **92**, 1795–1804 (1993).

181. Stojkov, G., Niyazov, Z., Picchioni, F. & Bose, R. K. Relationship between structure and rheology of hydrogels for various applications. *Gels* **7**, (2021).

182. Guixé-Muntet, S. *et al.* Nuclear deformation mediates liver cell mechanosensing in cirrhosis. *JHEP Reports* **2**, (2020).

183. Colombo, S. *et al.* Normal liver stiffness and its determinants in healthy blood donors. *Digestive and Liver Disease* **43**, 231–236 (2011).

184. Klaas, M. *et al.* The alterations in the extracellular matrix composition guide the repair of damaged liver tissue. *Sci Rep* **6**, 1–12 (2016).

185. Place, E. S., Rojo, L., Gentleman, E., Sardinha, J. P. & Stevens, M. M. Strontium-and zinc-alginate hydrogels for bone tissue engineering. *Tissue Eng Part A* **17**, 2713–2722 (2011).

186. Furthmayr, H., Lankes, W. & Amieva, M. Moesin, a new cytoskeletal protein and constituent of filopodia: Its role in cellular functions. *Kidney Int* **41**, 665–670 (1992).

187. Hirata, T. *et al.* Moesin-deficient mice reveal a non-redundant role for moesin in lymphocyte homeostasis. doi:10.1093/intimm/dxs077.

188. Ansa-Addo, E. A. *et al.* Membrane-organizing protein moesin controls Treg differentiation and antitumor immunity via TGF-? signaling. *Journal of Clinical Investigation* **127**, 1321–1337 (2017).

189. Parisiadou, L. *et al.* Neurobiology of Disease Phosphorylation of Ezrin/Radixin/Moesin Proteins by LRRK2 Promotes the Rearrangement of Actin Cytoskeleton in Neuronal Morphogenesis. (2009) doi:10.1523/JNEUROSCI.3799-09.2009.

190. Karvar, S. *et al.* Moesin, an Ezrin/Radixin/Moesin Family Member, Regulates Hepatic Fibrosis. *Hepatology* **72**, 1073–1084 (2020).

191. Pinzani, M. *et al.* Endothelin 1 is overexpressed in human cirrhotic liver and exerts multiple effects on activated hepatic stellate cells. *Gastroenterology* **110**, 534–548 (1996).

192. Loomba, R. *et al.* Heritability of Hepatic Fibrosis and Steatosis Based on a Prospective Twin Study. *Gastroenterology* **149**, 1784–1793 (2015).

193. Karlsen, T. H., Lammert, F. & Thompson, R. J. Genetics of liver disease: From pathophysiology to clinical practice. *J Hepatol* **62**, S6–S14 (2015).

194. Ruhanen, H. *et al.* PNPLA3 mediates hepatocyte triacylglycerol remodeling. *J Lipid Res* **55**, 739–746 (2014).

195. Kabbani, M. *et al.* Human hepatocyte PNPLA3-148M exacerbates rapid non-alcoholic fatty liver disease development in chimeric mice In brief Human hepatocyte PNPLA3-148M exacerbates rapid non-alcoholic fatty liver disease development in chimeric mice. *CellReports* **40**, 111321 (2022).

196. He, S. *et al.* A sequence variation (I148M) in PNPLA3 associated with nonalcoholic fatty liver disease disrupts triglyceride hydrolysis. *Journal of Biological Chemistry* (2010) doi:10.1074/jbc.M109.064501.

197. Ryan, S. L. *et al.* Drug Discovery Approaches Utilizing Three-Dimensional Cell Culture. *Assay Drug Dev Technol* **14**, 19–28 (2016).

198. Bell, E., Ivarsson, B. & Merrill, C. Production of a tissue-like structure by contraction of collagen lattices by human fibroblasts of different proliferative potential in vitro (tissue structure/hydrated collagen lattice/fibroblast function/cell aging/contractility). *Cell Biology* **76**, 1274–1278 (1979).

199. Soon, R. K. & Yee, H. F. Stellate Cell Contraction: Role, Regulation, and Potential Therapeutic Target. *Clin Liver Dis* **12**, 791 (2008).

200. Vespasiani-Gentilucci, U. *et al.* Combining Genetic Variants to Improve Risk Prediction for NAFLD and Its Progression to Cirrhosis: A Proof of Concept Study. (2018) doi:10.1155/2018/7564835.

201. Liu, Y. L. *et al.* TM6SF2 rs58542926 influences hepatic fibrosis progression in patients with non-alcoholic fatty liver disease. *Nat Commun* **5**, (2014).